# Aspects of Ion Coulomb Crystal based Quantum Memory for Light


Anders Mortensen

PhD thesis

Danish National Research Foundation
Center for Quantum Optics – Quantop
Department of Physics and Astronomy
The University of Aarhus
February 2005

This Thesis is submitted to the Faculty of Science at the University of Aarhus, Denmark, in order to fulfill the requirements for obtaining the PhD degree in Physics.
The studies have been carried out under the supervision of Ass. Prof. Michael Drewsen in the Ion Trap Group at the Department of Physics and Astronomy, University of Aarhus from January 2001 to February 2005.

# PREFACE

The present Thesis is based on my work done during the last four years in the Ion Trap Group at the Department of Physics and Astronomy, University of Aarhus, under the supervision of Michael Drewsen. During this time I have gained insight in the field of quantum optics and the field of ion trapping from an experimentalist point of view. The everyday tasks and challenges have been numerous ranging from working with sometimes intractable lasers, craftsmanship in the workshop, constructing new experimental devises from scratch and working with vacuum technology.

The work presented in this Thesis could not have been accomplished without the collaborative work of former and present group members of the Ion Trap group. I would like to thank the master students that I have been working which includes Kristian Støchkel, Frank K. Jensen, Inger Stensgaard, Randi Martinussen, Anders Bertelsen, Jens Lindballe, and Esben S. Nielsen. I am especially grateful to Jens Lindballe and Esben S. Nielsen for their contributions to the work presented in this Thesis. When I first joined the Ion Trap Group there were two senior fellow PhD students Liv Hornekær and Niels Kjærgaard, who were always willing to give me advise on how to handle the lab equipment. I would especially like to thank fellow PhD student Peter Staanum, who started his PhD study about a year before me. For about three years I benefitted from his pleasant company and useful physics related discussions. Lately fellow PhD students Peter Herskind and Ditte Møller have joined our group. Peter Herskind has taken over my project with a skilful and enthusiastic approach. Dirk Voigt spent two years with us as a Postdoc and has contributed with ideas and discussions to the presented project as well as doing important build up of laser systems. Jens Lykke Sørensen joined us for a little more than a year ago and his help with the final stages of the build up of the trap setup has been invaluable. The last group member I would like to acknowledge my supervisor Michael Drewsen for introducing me to and completely guiding me through this interesting project. His never failing enthusiasm for the subject of physics and our many fruitful discussions has helped me through times when the next step to proceed along was not obvious. I would also like to thank Claudia Mewes and Michael Fleischhauer for patiently explaining and discussing the theoretical aspects of my project.

An important contribution to the work presented in this thesis has been done by the technical staff at the University of Aarhus. I appreciate all the people at the mechanical workshop, the electronics department and the construction group for their competent and kind help. Here I would like to give a special

thanks to the people that were directly involved in the project. These include: Henrik Bechtold for his innovative approach to designing the ion trap. Finn Rander for making the parts to the ion trap and teaching me how to machine ceramics. Torben Hyltoft Thomsen for helping me when I was on my own in the students mechanical workshop. The vacuum lab guys Karsten Rasmussen and Jens Vestergaard for teaching me stuff about vacuum technology that does not appear in textbooks. I would also like to mention Uffe Simonsen, Kåre Iversen, and Robert Stensgaard, who were in charge of the technical staff. Also thanks to the administrative staff and especially Grete Flarup, who was always helpful.

I am indebted to my family and friends for giving support on a personal level during my more than eight years of physics study. I am also grateful for the friendships I have made during my years in Aarhus, which have been invaluable to me.

Finally I would like to acknowledge Peter Staanum, Peter Herskind and my father for proofreading this Thesis.

Feb. 2005, Anders Mortensen

# LIST OF PUBLICATIONS


[I] M. Drewsen, I. S. Jensen, J. J. T. Lindballe, N. Nissen, R. Martinussen, A. Mortensen, P. Staanum, and D. Voigt. Ion Coulomb crystals: a tool for studying ion processes, *Int. J. Mass Spec.*, 229:83–91, 2003.

[II] M. Drewsen, I. S. Jensen, N. Kjærgaard, J. J. T. Lindballe, A. Mortensen, K. Mølhave, and D. Voigt. Non-stationary Coulomb crystals in linear Paul traps, *J. Phys. B*, 36:525–532, 2003.

[III] A. Mortensen, J. J. T. Lindballe, I. S. Jensen, P. Staanum, D. Voigt, and M. Drewsen. Isotope shifts of the $4s^2\ ^1S_0 \leftrightarrow 4s5p\ ^1P_1$ transition and hyperfine splitting of the $4s5p^1P_1$ state in calcium. *Phys. Rev. A*, 69(4):042502, 2004.

[IV] M. Drewsen, A. Mortensen, R. Martinussen, P. Staanum, and J. L. Sørensen. Nondestructive identification of cold and extremely localized molecular ions. *Phys. Rev. Lett.*, 93:243201, 2004.

[V] M. Drewsen, A. Mortensen, J. J. T. Lindballe, K. Mølhave and N. Kjærgaard. Dynamically excited single-component ion Coulomb crystals in linear Paul traps. *Nucl. Instrum. & Methods A*, 532:237–240, 2004.

[VI] M. Drewsen, T. Matthey, A. Mortensen, and J. P. Hansen. Thermally excited three-dimensional long-range order in smaller Coulomb clusters. *Manuscript in preparation.*

CONTENTS

# 1. INTRODUCTION

Interactions between light and matter carry a special position in the study of fundamental quantum phenomena. In the years since the invention of the laser techniques have been refined to such a level that today it is possible to deterministically create specific superposition states of matter by interaction with laser light. The field of quantum information has in the last decade been subject to a huge interest conceived from the fact that a computer, operating on quantum mechanical principles, is capable of solving certain computational problems exponentially faster than a classical computer. A practical realization of such a quantum computer could consist of a network of quantum processors which communicate information about their quantum states by exchanging photons that have the information encoded in their polarization states or spatial wave functions. One of the building blocks of such a scheme is a light memory interface, which can temporarily store a photon while preserving its quantum state.

Atoms have the desired properties for temporal storage of photons. Controlled mapping of a photon field onto atoms can be done using Raman adiabatic-passage techniques [1]. This is done with single atoms and photons in the context of cavity-QED [2]. Another approach, which is technically less demanding, is to have a large number of atoms and make use of electromagnetically induced transparency [3] to map photon states onto a collective excitation of an atomic ensemble. The basic techniques for the latter approach have recently been demonstrated in a cold cloud of sodium [4] as well as in atomic rubidium vapor [5], where the classical properties of a pulse of light was temporarily stored.

For the realization of a memory for light, that preserves the quantum state of the light pulse during the whole storage procedure, we consider using cold trapped ions as a storage medium. In general trapped ions are excellent targets for quantum optics experiments, because they exhibit good spatial localization and have internal states with very long decoherence times. Examples where these properties are exploited include the experimental entanglement of four ions [6] and the probing of the standing wave field of an optical resonator using a single trapped ion [7].

The main theme in the present Thesis is quantum memory for light using cold trapped ions. The trapped ions used for the light memory are cooled by means of sympathetic cooling with another Doppler laser cooled ion species. When Doppler laser cooling is applied to trapped ions temperatures in the milliKelvin range are reached. Here the thermal kinetic energy of the ions is so low compared to the mutual Coulomb repulsion of the ions that a crystalline

ordering of the ions is observed and a so-called ion Coulomb crystal is formed. In the proposed quantum memory scheme the ion Coulomb crystal will consist of $^{40}Ca^{+}$ ions which are sympathetically cooled by Doppler laser cooled $^{44}Ca^{+}$ ions. In contrast to the typical quantum optical experiments on trapped ions, where the number of ions are limited to only a few ions, this ion crystal will consist of several thousand calcium ions. The production of these big two-isotope ion Coulomb crystals is done using a photo-ionization technique.

Due to technical limitations of the trapping potentials and the Coulomb repulsion between the ions the obtainable ion densities in an ion Coulomb crystal is quite limited typically in the range $10^7$–$10^8$ cm$^{-3}$. The ion density limitation in turn restrains the optical density of the ion Coulomb crystals and as a consequence we need to follow the original proposal of Fleischhauer *et al.* [8] and increase the coupling between the photon to be stored and the ions by placing the ion Coulomb crystal in the mode of an optical resonator. The situation is accordingly that we have a collective coupling between a few thousand calcium ions and the mode of an optical resonator. The advantage is that the technically challenging strong coupling requirement can be relaxed when the coupling is collectively enhanced. The trapping potentials furthermore allow for an excellent positioning control of the ions into the mode of the optical resonator.

In this Thesis the first steps towards realizing this quantum memory in ion Coulomb crystals are presented. The current status of the project is that an ion trap with an integrated optical resonator has been built and installed in an ultra high vacuum chamber. The Thesis will focus on the ideas and reflections that have concluded in the construction of the vacuum chamber and the ion trap as well as the future plans for the evolvement of the quantum memory project. We will also in the context of quantum memory in ion Coulomb crystals address some experiments on the structure and the production of two isotope calcium ion Coulomb crystals. The Thesis hence covers many facets from different areas of physics including quantum optics, spectroscopy, ion trap physics, laser cooling, and plasma physics, all of which it is my hope that the reader will appreciate getting acquainted with.

## *Outline of the Thesis*

The Thesis is divided in two major parts. In the first part (Chapters 3–6) experiments with $Ca^{+}$ ions trapped in a linear Paul trap are described. A common aspect of these experiments is that they are all of relevance for the project of light storage in ion Coulomb crystals, whether that is the production of large bi-crystals or the structural properties of these bi-crystals. In the second part (Chapters 7–9) we approach the subject of light storage in ion Coulomb crystals more directly with an introduction to the subject and a description of the experimental status of the project.

Chap. 2 A short description of the basic theory of the linear Paul trap and Doppler laser cooling of ions followed by a discussion of the physics of single- and multi-species Coulomb crystals.

Chap. 3 Description of the experimental equipment used for the experiments described in chapters 4–6, but also of relevance for the discussion of the light storage in Coulomb crystals.

Chap. 4 After a general introduction to the photo-ionization ion trap loading technique we use in Aarhus, spectroscopic measurements of the transition used for the photo-ionization are presented. The quantitative results of this part have been published in Ref. [III]. At the end the isotope selectivity of the loading scheme is presented.

Chap. 5 Charge transfer rate measurements between neutral $^{40}$Ca atoms and singly charged calcium ions of another isotope are presented. From the results an estimate of the charge transfer cross section is given.

Chap. 6 Crystal structures of one- and two-species ion Coulomb crystals are studied experimentally. A special emphasis is put on the lattice structure. The experimental results are supported by molecular dynamics simulations.

Chap. 7 General introduction to the theory behind the quantum memory scheme on which the light storage in ion Coulomb crystals is based. The chapter is rounded off with an overview of the current experimental status of quantum memory for light.

Chap. 8 This chapter deals with light storage in trapped ions. After presenting basics of the proposed scheme for light storage in ion crystals the fidelity of single photon storage is estimated from numerical simulations. Considerations concerning the more technical side of the Paul trap with an integrated resonator are presented next.

Chap. 9 Presentation of the real trap setup as well as the vacuum chamber in which it is installed. At the end of the chapter some measurements that characterize the optical resonator are presented.

Chap. 10 Summary and outlook.

# 2. BASIC THEORY

This chapter begins with an introduction to the theory of ion trapping in the linear Paul trap followed by a discussion of Doppler laser cooling with special attention to cooling of $Ca^+$ ions. Next the theory of cold confined ion plasmas is given and the end of the chapter the concept of sympathetic cooling in multi-component plasmas is presented.

## *2.1 Linear Paul trap theory*

The linear Paul trap is an experimental construction that can trap and confine charged particles. All the experiments on trapped ions presented in this Thesis are performed in a linear Paul trap, and the light memory ion trap construction presented in Chap. 9 is also based on the linear Paul trap design. The predecessor of the linear Paul trap was the quadrupole mass filter invented by Wolfgang Paul [9] back in the 1950's, while the linear Paul trap was developed about 30 years later [10]. Other types of ion traps include the hyperbolic Paul trap [11], the Penning trap [12], and the race-track trap [13]. In present section we will develop the basic theory of the linear Paul trap (see also Ref. [14]) and introduce the quantities relevant for the Thesis.

The Paul trap design we shall consider in this Thesis consists of four electrode rods situated in a quadrupole configuration as depicted in Fig. 2.1. Each of the 4 electrode rods are sectioned in 3 pieces, two end-cap electrodes and a center-electrode, such that the trap consists of a total of 12 electrodes on which individual voltages can be applied. According to Earnshaws theorem it is not possible to confine a charged particle spatially using static electric potentials only. To remedy this time varying electric fields are used in the linear Paul trap. More specifically we obtain a time varying quadrupole electric field between the electrodes by applying the voltage $\frac{1}{2}U_{\rm rf}\cos\Omega_{\rm rf}t$ to the two of the diagonally opposite electrode rods, while the voltage $-\frac{1}{2}U_{\rm rf}\cos\Omega_{\rm rf}t$ is applied to the two remaining electrode rods (see Fig. 2.1). If the proper geometry is chosen the resulting electric potential becomes $U(x,y,z) = -\frac{1}{2}U_{\rm rf}\cos\Omega_{\rm rf}t[(x^2-y^2)/r_0^2]$, where $r_0$ is the inter electrode inscribed radius. Note that the electric potential depends on $x$ and $y$ and thus only affects the charged particle motion in the $xy$-plane. To confine the particle axially we apply an additional static bias voltage, the end-cap voltage $U_{\rm ec}$, to the 8 end-cap electrodes. Again, if the right trap geometry is chosen, the axial electric potential near the trap center derived from the end-cap potential becomes approximately $\phi_z(z) = \eta U_{\rm ec}\frac{z^2}{z_0^2}$,

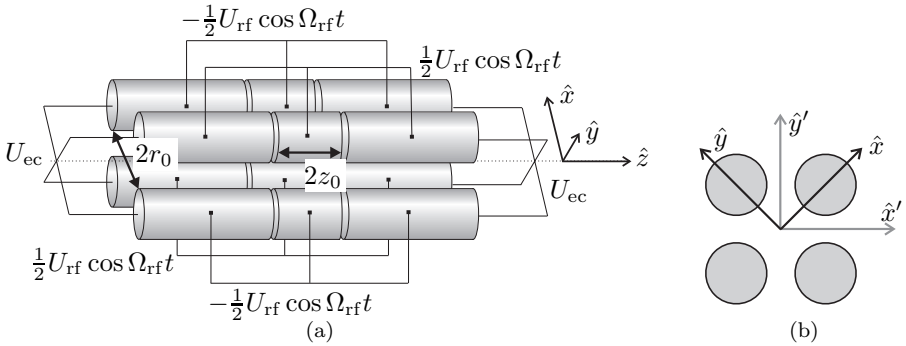


*Fig. 2.1:* (a) Linear Paul trap electrode configuration with applied voltages. We will refer to the $\hat{z}$-axis as the trap axis (dotted line). (b) End-view of the Paul trap with the definitions of the $\hat{x}$ and $\hat{y}$ axis (black). The $\hat{x}'$ and $\hat{y}'$ axis (grey) are used elsewhere.

where the axial geometric factor $\eta$ is related to the trap geometry and $2z_0$ is the center-electrode length. Adding the radial part of the end-cap potential to the sinusoidally varying electric potential we get

$$\phi(x,y,t) = -\frac{1}{2}U_{\mathrm{rf}}\cos\Omega_{\mathrm{rf}}t\frac{x^2-y^2}{r_0^2} - \frac{1}{2}\eta U_{\mathrm{ec}}\frac{x^2+y^2}{z_0^2} \tag{2.1}$$

for the radial trapping potential. The equations of motion of a particle influenced by the electric potential in Eq. (2.1) can be rewritten as

$$\frac{d^2\nu}{d\tau^2} + (a - 2q_\nu\cos 2\tau)\nu = 0, \quad \nu = x, y, \tag{2.2}$$

where we have made the substitutions

$$\tau = \frac{\Omega_{\mathrm{rf}}t}{2}, \quad a = -4\frac{\eta Q U_{\mathrm{ec}}}{z_0^2 M\Omega_{\mathrm{rf}}^2}, \quad q_x = -q_y = 2\frac{QU_{\mathrm{rf}}}{Mr_0^2\Omega_{\mathrm{rf}}^2}. \tag{2.3}$$

The differential equations (2.2) are well-known in literature as the Mathieu equation [15]. The Mathieu equation has stable solutions for certain values of the $a$ and $q$ parameters. In Fig. 2.2(a) the stability regions of the Mathieu equation are mapped out in $(q,a)$-space. Because stable motion in the axial direction require that $a < 0$ the region of stable particle motion is restricted to the region mapped out in Fig. 2.2(b). In some situations it is desirable to have more than one ion species trapped simultaneously. This requires that there exists trapping parameters for which ion species in question all have $a$ and $q$ parameters that give stable ion motion. As evident from Eq. (2.3) the $a$ and $q$ parameters depend on the charge-to-mass ratio $Q/M$ and stable motion of the simultaneously trapped ion species is thus obtainable if their $Q/M$ values are sufficiently close to each other.

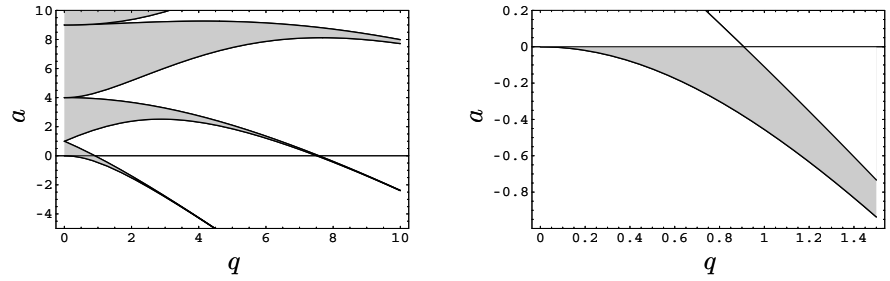


(a) (b)

*Fig. 2.2:* (a) Stability diagram of the Mathieu function in the $(q, a)$-plane. Regions with stable solutions are marked with grey. (b) Region of stable motion of a particle in the linear Paul trap. Both diagrams also apply to negative $q$-values, i.e., the stability regions are mirrored in the $a$-axis.

For $|a|, |q| \ll 1$ the solution to the Mathieu equation takes the simple form

$$\nu(t) = \nu_0(1 - q_\nu \cos \Omega_{\rm rf} t) \cos \omega_r t, \tag{2.4}$$

where the secular frequency

$$\omega_r = \frac{\sqrt{q^2/2 + a}}{2} \Omega_{\rm rf}, \tag{2.5}$$

has been introduced. This equation describes a slowly oscillating radial motion, the *secular motion* with a small amplitude, fast oscillating motion, the *micromotion*, superposed on the secular motion. Notice that the micromotion is perpendicular to the trap axis defined as the $z$-axis in Fig. 2.1.

Averaging out the fast motion of Eq. (2.4), the three dimensional motion of the trapped ion can be described by the harmonic pseudopotential

$$\Phi_{\rm ps}(r, z) = \frac{1}{2} M(\omega_r^2 r^2 + \omega_z^2 z^2), \quad r^2 = x^2 + y^2, \tag{2.6}$$

where the axial trapping frequency is given by $\omega_z = \sqrt{-a/2}\Omega_{\rm rf}$. It is important to note here that while the pseudopotential is clearly independent on the mass of the ions axially this is not the case radially. It is easily apparent from Eq. (2.6) that for ions of equal charge, but different mass, the lighter ions are stronger bound towards the trap axis. This means that when different species of ions are simultaneously trapped they will separate spatially with the lightest ions closest to the trap axis.

## *2.2 Doppler laser cooling theory*

In the following we will discuss Doppler laser cooling of a trapped ion. The Doppler cooling is based on the absorption and emission of photons from a laser

field and the Doppler shift of the resonance frequency of an ion moving in the laser field. The experiments considered in this Thesis are all performed with the ions moving in a weakly binding potential for which the trap oscillation frequency $\omega_z$ is much smaller than the natural linewidth $\Gamma$ of the transition used for the Doppler cooling. When this is the case the ion can be regarded as a free atom as the timescale of the absorption-emission process responsible for the laser cooling is much shorter than the timescale for which the ion changes its motional state due to the trap potential. In the case of calcium the natural linewidth of the transition used for Doppler cooling is $\Gamma \sim 2\pi \times 22$ MHz and a typical trap frequency in the experiments considered here is $\omega_z \sim 1$ MHz. In the regime where the natural linewidth of the cooling transition in the ion is much smaller than the trap frequencies *sideband cooling* to near the motional ground state of one or a few trapped ions becomes feasible [16, 17]. Currently the Aarhus ion trap group is working towards performing sideband cooling on a few ions [18].

The basic mechanism responsible for Doppler cooling can be understood by considering two counter-propagating laser beams of frequency $\omega_{\rm L}$ interacting with a two-level atom moving in one dimension towards one of the laser beams with velocity $v$. The resonance frequency of the atom is denoted $\omega_a$. Assuming that the lasers are red detuned with respect to the atomic resonance, i.e., that $\omega_{\rm L} < \omega_a$, we know that for a certain velocity $v$ the atom is resonant with the laser light that propagates towards the atom, because of the Doppler shift. On the other hand the laser light that propagates in the same direction as the atom is shifted away from the atomic resonance. The atom will thus preferentially scatter photons that propagate in the opposite direction of the atom, and the atom is accordingly slowed down, because of the momentum transfer from the light field. After many scattering events an equilibrium state is reached, where the temperature is ultimately set by the random nature of the scattering process.

Consider a two level ion with ground state $|g\rangle$, excited state $|e\rangle$, and transition frequency $\omega_{eg}$ interacting plane wave laser field given by

$$E(\mathbf{r}, t) = \hat{\epsilon} E_0 \cos(\omega_{\rm L} t - \mathbf{kr}), \tag{2.7}$$

where $\omega_{\rm L}$ is the laser frequency, $\mathbf{k} = k\hat{z}$ is the wave vector of the light, and $\hat{\epsilon}$ is the polarization of the light. The Hamiltonian in the rotating wave approximation interaction picture is

$$H_{\rm rwa} = \frac{\hbar\Omega}{2} e^{i(\mathbf{kr} - \omega_{\rm L} t)} |e\rangle\langle g| + \text{h.c.}, \tag{2.8}$$

where the Rabi frequency is given by $\Omega = -(eE_0/\hbar)\langle e|r|g\rangle$. In this picture the rate at which photons from the field are scattered by an ion is given by

$$\gamma = \Gamma \frac{|\Omega|^2/4}{\delta^2 + |\Omega|^2/2 + \Gamma^2/4} = \Gamma/2 \frac{s}{\left(\frac{\delta}{\Gamma/2}\right)^2 + 1 + s}, \tag{2.9}$$

where we have introduced the saturation parameter $s \equiv 2|\Omega|^2/\Gamma^2$ and the laser detuning $\delta \equiv \omega_{\rm L} - \omega_{eg}$. When the ion is moving with velocity $\mathbf{v}$ the frequency of

the incoming light is Doppler shifted to first order by $-\mathbf{kv}$. This can be taken into account by making the substitution $\delta \to \delta - kv_z$ in Eq. (2.9):

$$\gamma(\delta, v_z) = \Gamma/2 \frac{s}{\left(\frac{\delta - kv_z}{\Gamma/2}\right)^2 + 1 + s}. \tag{2.10}$$

We neglect recoil kicks due to spontaneous emission for the time being, because the net force on the ion averaged over many scattering events is zero due to the symmetry of the angular distribution of the spontaneously emitted photons. The radiation pressure force on the ion from the laser field is consequently given by the momentum transfer from the absorption of one photon from the laser field multiplied with the scattering rate in Eq. (2.9) giving the force $F_+(k, v_z) = \hbar k \gamma(v_z, k)$ along the $\hat{z}$ direction. Expanding the force around $v = 0$ gives $F_+ \cong F_0 - \beta v_z$, where the coefficients are given by

$$F_0 = \frac{\Gamma}{2} \frac{s}{\left(\frac{\delta}{\Gamma/2}\right)^2 + 1 + s} \quad \text{and} \tag{2.11}$$

$$\beta = -4\hbar k^2 \frac{s}{\left[\left(\frac{\delta}{\Gamma/2}\right)^2 + 1 + s\right]^2} \frac{\delta}{\Gamma}. \tag{2.12}$$

It is seen that the force from one laser beam propagating along the $\hat{z}$-axis is a sum of two contributions, i.e., a constant light pressure and a force that depends on the ion velocity.

In order to counteract the constant light pressure $F_0$ a counter-propagating laser beam with the same frequency and intensity as the laser field described by Eq. (2.7) is sent in providing the force $F_-(k, v_z) = -\hbar k \gamma(-k, v_z)$ along the $\hat{z}$-axis direction. Provided that the ion is not saturated in the scattering process, i.e., $s \ll 1$, the scattering force from the two counter-propagating laser beams can be added giving a total laser cooling force $F^{\rightleftarrows} = \hbar k \gamma(k, v_z) - \hbar k \gamma(-k, v_z)$. For small velocities the force becomes $F^{\rightleftarrows} = -2\beta v_z$ which is illustrated in Fig. 2.3. For negative laser detuning ($\delta < 0$) the coefficient $\beta$ is positive, i.e., the velocity dependent force opposes the ion velocity and therefore viscously damps the ion motion. This mechanism thus effectively leads to a cooling of the ion and the rate at which kinetic energy of the ion is removed is given by $R_{\text{cool}} = -\langle F^{\rightleftarrows} v_z \rangle = 2\beta \langle v_z^2 \rangle$.

If we take the spontaneous emission process into consideration it is true as mentioned that the average momentum transfer after many spontaneous emission cycles is zero, but the rms momentum transfer is finite. This momentum diffusion (see Ref. [19]) introduces a heating mechanism of the ion and the rate of heating is approximately given by $R_{\text{heat}} = 2\gamma \times \frac{(\hbar k)^2}{2m}$. The factor $2\gamma$ is just the rate of emission rate when we have two laser beams in the low saturation limit, while the energy $\frac{(\hbar k)^2}{2m}$ is the recoil energy of the ion when emitting a photon. The absorption process introduce a similar heating process when the ion moves at low velocity, because in this case there is no preferred direction of absorption

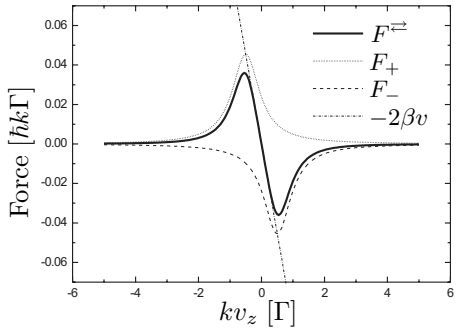


*Fig. 2.3:* Velocity dependence of the laser force on an ion for two counter-propagating cooling lasers (full line), when the detuning is $\delta = -\Gamma/2$ and the saturation parameter is $s = 0.1$. See text for further details about the different graphs.

and the ion will get a random kick in the $\hat{z}$ direction. The heating rate of the absorption process is on the order $R_{\text{heat}}$, and we therefore get that the total heating rate from absorption and spontaneous emission becomes $2R_{\text{heat}}$. Using $\delta = -\Gamma/2$ as the optimal choice of detuning and equating $R_{\text{cool}} = 2R_{\text{heat}}$ we get the steady state kinetic energy of the ion is $\hbar\Gamma/4$. Defining the ion temperature through the kinetic energy of the ion $k_{\text{B}}T/2 = m\langle v_z^2\rangle/2$ we find the Doppler temperature

$$T_{\text{D}} = \frac{\hbar\Gamma}{2k_{\text{B}}}, \tag{2.13}$$

which is the limiting temperature when Doppler cooling is employed.

The Doppler cooling discussed here only affects the motion in the $\hat{z}$ direction. Doppler cooling of a free particle in all 3 dimensions would require 6 in pairs counter-propagating laser beams. In the case of trapped ions Coulomb interactions between the ions introduce momentum transfer between the transverse ($\hat{x}$–$\hat{y}$) directions and the axial $\hat{z}$ direction. This coupling leads to sympathetic cooling of the transverse degrees of freedom and in most cases it is only necessary to cool the ions in the $\hat{z}$ direction using counter-propagating beams. In the special case where we have a few ions on a linear string aligned along the trap axis (see Fig. 2.1) we usually employ laser cooling both along the trap axis and in one of the transverse directions.

### *2.2.1 Doppler laser cooling of $^{40}Ca^{+}$*

The ion trap experiments described in this Thesis are all performed on the $Ca^{+}$ ion. In the present section we will accordingly discuss the Doppler laser cooling of $^{40}Ca^{+}$. The $^{40}Ca^{+}$ ion has its electronic ground state configuration with a single optically active electron outside a closed shell. The level-scheme of the $^{40}Ca^{+}$ ion is presented in Fig. 2.4. The $4S_{1/2}$ ground state is coupled via dipole allowed transitions to the excited $4P_{1/2}$ and $4P_{3/2}$ states at 397 nm and 393 nm, respectively. The $P$-states are in turn coupled via dipole-allowed transitions to

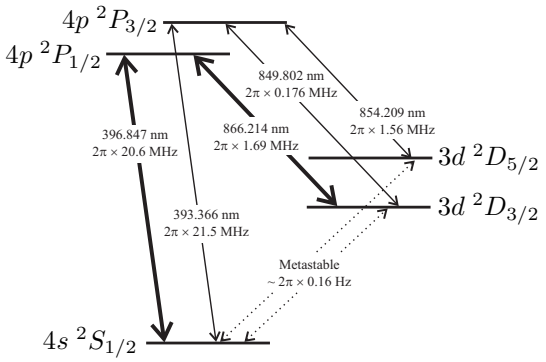


*Fig. 2.4:* Level scheme for Doppler cooling of $Ca^+$ with wavelengths and partial decay rates for the dipole allowed transitions [20]. The thick lines indicate the transitions most frequently used for Doppler cooling of $Ca^+$. In the following we the shorter notation $4S_{1/2}$, $4P_{1/2}$, etc., for the states of the $Ca^+$ ion.

the $3D_{3/2}$ and $3D_{5/2}$ states at wavelengths 866 nm, 854 nm, and 850 nm (see Fig. 2.4). The $D$-states are metastable with natural lifetimes of $\sim$ 1 s. The decay of the $D$-states is to the ground state.

The partial decay rates of the excited states are included in Fig. 2.4. The two most encountered transitions in this Thesis are the $4S_{1/2} \leftrightarrow 4P_{1/2}$ and the $3D_{3/2} \leftrightarrow 4P_{1/2}$ transitions, which have the decay rates $\Gamma_{397} = 2\pi \times 20.6$ MHz and $\Gamma_{866} = 2\pi \times 1.69$ MHz, respectively. Here the indices refer to the transition wavelength in nm.

From the level scheme shown in Fig. 2.4 we see that there is no closed two-level transition that can be used for laser cooling of the $^{40}Ca^+$ ion, so the Doppler cooling theory discussed for a two-level ion in Sec. 2.2 is at first sight not applicable. Doppler cooling of $^{40}Ca^+$ ions is nevertheless possible if more than one laser frequency is used, and furthermore does the Doppler cooling theory presented in Sec. 2.2 also approximately apply to the laser cooling of $^{40}Ca^+$ ion. The most frequently used transition for Doppler cooling in the experiments described in this Thesis is the 397 nm $4S_{1/2} \leftrightarrow 4P_{1/2}$ transition. From the excited $4P_{1/2}$-state the ion can decay via two channels, namely back to the ground state and to the metastable $3D_{3/2}$ state. The branching ratio between these two channels is $\Gamma_{397}/\Gamma_{866} \approx 12$, so in order to avoid that the ion ends up in the metastable state after only a few cooling cycles of the 397 nm transition we deplete the $3D_{3/2}$ level by adding an 866 nm laser. The large branching ratio between the two decay channels implies that most of the cooling cycles are on the $4S_{1/2} \leftrightarrow 4P_{1/2}$ transition, and as the 397 nm photon momentum is about twice the momentum carried by an 866 nm photon it is a good approximation to expect the cooling limit to be given by the Doppler cooling limit for the 397 nm transition, which is

$$T_{\mathrm{D}} = 0.5 \text{ mK}. \tag{2.14}$$

To achieve optimal cooling of the $^{40}Ca^+$ ions we also need to consider the

magnetic substates of the three states involved in the cooling scheme. First of all it is advantageous to avoid optical pumping into one of the magnetic substates of the $^2S_{1/2}$ state. This is avoided by the use of laser light that is $\pi$-polarized with respect to the quantization axis defined by the bias magnetic field, or using any combination of $\sigma_+$, $\sigma_-$, and $\pi$-polarized light. For the $^2D_{3/2}$-state optical pumping into the substates with magnetic quantum numbers $m_{3/2} = -3/2, 3/2$ and so-called dark resonances [21] can be avoided by applying an additional weak magnetic field perpendicular to the direction of propagation of the cooling lasers and the polarization of the 866 nm re-pump laser beam. We have used this method in the experiments described in this Thesis, but for the quantum memory trap project it is desirable to have a very small magnetic field in the trap region directed parallel to the cooling laser propagation direction. For such a magnetic field we can prevent optical pumping by fast rotation of the 866 nm re-pump cooling laser light polarization by using an electro-optic modulator.

The $4S_{1/2} \leftrightarrow 4P_{3/2}$ transition at 393 nm can be used for Doppler cooling of $^{40}Ca^+$ as well. The only difference is that we here need two re-pump lasers at 854 nm and 850 nm (see Fig. 2.4). Apart from this the discussion above also applies to this transition and we find the same Doppler cooling limit for the 393 nm transition, namely $T_D = 0.5$ mK.

### 2.2.2 Doppler laser cooling of $Ca^+$ isotopes

We have restricted the discussion in Sec. 2.2.1 to cooling of $^{40}Ca^+$ ions, but the discussion has a more general scope as Doppler laser cooling of the other naturally occurring calcium isotopes is done using same techniques, with $^{43}Ca^+$ as the only exception as this has a hyperfine structure because of its non-zero nuclear spin. In Table 2.1 the measured isotope shifts relative to $^{40}Ca^+$ of the 397 nm and the 866 nm transitions in $Ca^+$ have been listed for future reference. The isotope shifts are given by the expression $\nu_A - \nu_{40}$, where $\nu_{40}$ and $\nu_A$ are the resonance frequencies of the transition in question in the $^{40}Ca^+$ ion and the $^A Ca^+$ ion, respectively. Note that the isotope shifts in Table 2.1 are much larger than the spectral width of the dipole allowed transitions in the $Ca^+$ ion, when Doppler cooling is applied. When more than one calcium isotope is trapped this implies that laser cooling can be applied selectively to one ion species while the electronic states of the other ion species are unaffected.

## 2.3 Ion Coulomb crystals

The study of crystallized charged plasmas was initiated in the 1930s by Wigner who introduced the theory of the Wigner crystal [24]. Several model systems of these crystallized charged plasmas have been studied since then. The overall confinement the plasmas, such as an ion plasma, is done by a neutralizing background, e.g., electromagnetic fields. The crystallized state of an electron plasma in a metal is one example of such a model system [25]. Here the immobile metallic ions constitute the neutralizing background that confines the mobile valence electrons. On a macroscopic scale the crystallized plasmas can

| | $4S_{1/2} \leftrightarrow 4P_{1/2}$ | $3D_{3/2} \leftrightarrow 4P_{1/2}$ |
|---|---|---|
| $^{42}Ca^{+}$ | 425(4) | -2366(59) |
| $^{43}Ca^{+}$ | 672(9) | -3163(94) |
| $^{44}Ca^{+}$ | 842(3) | -4509(24) |
| $^{46}Ca^{+}$ | 1287(3) | |
| $^{48}Ca^{+}$ | 1696(4) | |

*Tab. 2.1:* Experimentally determined isotope shifts in $Ca^{+}$ relative to the $^{40}Ca^{+}$ resonance ($\nu_A - \nu_{40}$) for the transitions used in the basic Doppler laser cooling scheme. The data was taken from [22] for the $4S_{1/2} \leftrightarrow 4P_{1/2}$ transition and from [23] for the $3D_{3/2} \leftrightarrow 4P_{1/2}$ transition. All shifts are given in units of MHz.

be realized in dusty plasmas consisting of charged dust particles of $\sim \mu$m size confined by electromagnetic potentials [26].

Ion plasmas confined in an ion trap by electromagnetic fields can also undergo crystallization to constitute a state of matter called *ion Coulomb crystals*. In Nature ion Coulomb crystals are believed to exist in the interior of white dwarf stars, where fully ionized nuclei moving in a neutralizing background of electrons constitutes the ion plasma [27].

The thermodynamics of plasmas is described by the plasma coupling parameter $\Gamma$ which is the ratio of the inter particle Coulomb energy to the thermal energy. For an one component plasma at the temperature $T$ we have

$$\Gamma = \frac{Q^2}{4\pi\epsilon_0 a_{\mathrm{ws}} k_{\mathrm{B}} T}, \tag{2.15}$$

where $Q$ is the charge of the confined particles, and $a_{\mathrm{ws}}$ is the Wigner-Seitz radius defined by $\frac{4}{3}\pi a_{\mathrm{ws}}^3 = n_0^{-1}$ for the zero temperature ion density $n_0$.

The value of the coupling parameter determines what the thermodynamical state of the plasma is. The transition from the gas phase to the liquid phase, where short range order governs the plasma, occurs at $\Gamma \simeq 2$ [28] and for $\Gamma > 170$ the plasma is in the solid phase [29, 30], which is characterized by long range order. For an one component plasma of infinite extend the body-centered cubic (bcc) lattice is the predicted ground state structure of the crystallized state. Then the particle density is $n_0 \sim 10^8$ cm$^{-3}$, which is characteristic for our experiments with singly charged trapped ions, the onset of the of the plasma crystallization occurs at temperature $T \sim 10$ mK. This temperature is reachable by Doppler laser cooling, where for instance the Doppler cooling limit of $^{40}Ca^{+}$ ions is $T_{\mathrm{D}} \sim 0.5$ mK (see Sec. 2.2.2).

The Debye length of the ion plasma is given by

$$\lambda_{\mathrm{D}} = \sqrt{\frac{k_{\mathrm{B}} T \epsilon_0}{n Q^2}} \tag{2.16}$$

and it is the characteristic length for which the electric field of a test charge $Q$ inserted in the plasma is screened out by rearranging the plasma particles. Here

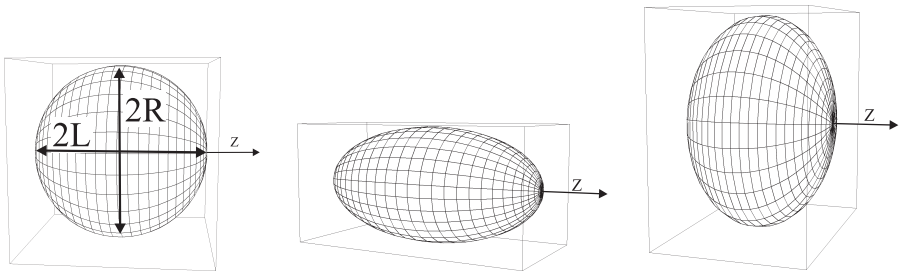


(a) Spherical ($R = L$) (b) Prolate ($R < L$) (c) Oblate ($R > L$)

*Fig. 2.5:* Possible spheroidal shapes of the ion Coulomb crystal. The $z$-axis corresponds to the trap axis in the linear Paul trap.

$n$ is the plasma particle density. A sample of charged particles is considered a plasma and the theory of charged plasmas is applicable if the spatial extend of the sample is larger than the Debye length. Insertion of the temperature $T \lesssim 10$ mK and the ion density $n = 10^8$ cm$^{-3}$, characteristic for ion Coulomb crystals, the Debye length becomes $\lambda_{\mathrm{D}} \lesssim 0.6$ $\mu$m, which is much smaller than the inter ion spacing in the Coulomb crystal and certainly smaller than the spatial extend of the ion crystals encountered in this Thesis.

The predicted ground state structure in a crystallized one component plasma of infinite extend is a bcc lattice structure. The ion Coulomb crystals treated in this Thesis are of finite extend though with a shape determined by the trapping potentials and the structural properties are thus effected by the crystal surface. For most of the ion Coulomb crystals treated here the bulk crystal structure is not even necessarily a 3D long range ordered lattice structure, because the ion crystal surface boundary arrange the ions in so-called shell structures instead. A spherically round ion Coulomb crystal is an example such a shell structure, where the ions will arrange in concentric spheres of different radii throughout the crystal. Each sphere constitutes a shell in the crystal. The inter shell distance is equivalent for all the shells and determined by the ion density of in the crystal.

The general shape of the ion plasma is not spherical. In the linear Paul trap where the ions are confined by the potential $\Phi_{\mathrm{ps}}(r, z) = \frac{1}{2}M(\omega_r^2 r^2 + \omega_z^2 z^2)$ a measure of the trap anisotropy can be given by the parameter $\alpha \equiv \omega_r^2/\omega_z^2$. For a given number of trapped ions the zero temperature crystal structure only depends on $\alpha$. For large values of $\alpha$ the ions will form an inhomogeneous linear string along the $z$-axis. As the value of $\alpha$ is decreased a zig-zag pattern appears near the trap center. When $\alpha$ is decreased even further a helical structure develops [31]. For sufficiently small values of $\alpha$ the ions arrange in concentric spheroidal shell structures with the $z$-axis as the axis of revolution. The spheroid structures are prolate for $\alpha > 1$ and oblate for $\alpha < 1$. The spherical, prolate and oblate spheroidal shapes are depicted in Fig. 2.5.

The ion density $n_0$ in the ion Coulomb crystal at zero temperature can be found by noting that the force $\mathbf{F}_{\mathrm{ion}}$ on each ion in the plasma in equilibrium

is zero, i.e., $\mathbf{F}_{\text{ion}} = -Q\nabla\phi_{\text{total}} = \mathbf{0}$, where $\phi_{\text{total}}$ is the total electric potential in the crystal. From the requirement that the derivative of $\phi_{\text{total}}$ should be zero we see that $\phi_{\text{total}}$ is constant inside the plasma. The total potential is furthermore given by the sum of the harmonic pseudopotential $\frac{\Phi_{\text{ps}}}{Q}$ (Eq. (2.6)) and the electric potential from the ion plasma $\phi_{\text{ion}}$, i.e.,

$$\phi_{\text{total}} = \frac{\Phi_{\text{ps}}}{Q} + \phi_{\text{ion}}. \tag{2.17}$$

Applying Laplaces' equation $\nabla^2\phi_{\text{total}} = 0$ to Eq. (2.17) and using Gauss law in the ion plasma $\nabla^2\phi_{\text{ion}} = -Qn_0/\epsilon_0$ we get the identity

$$\frac{2M\omega_r^2}{Q} + \frac{M\omega_z^2}{Q} = \frac{Qn_0}{\epsilon_0}, \tag{2.18}$$

which can be rewritten using the identities in Sec. 2.1 to yield the expression

$$n_0 = \frac{q^2}{4}\frac{\epsilon_0 M\Omega_{\text{rf}}^2}{Q^2} = \frac{\epsilon_0 U_{\text{rf}}^2}{Mr_0^4\Omega_{\text{rf}}^2} \tag{2.19}$$

for the zero temperature ion density of an ion Coulomb crystal. Notice that the density does not depend on the applied end-cap potential $U_{\text{ec}}$, the total number of ions trapped in the ion Coulomb crystal or the charge $Q$ of the trapped ions and that the density is uniform.

## 2.4 Sympathetic cooling and bi-crystals

In some situations it is desirable to be able to cool a trapped ion species without applying laser cooling directly. The most obvious reason is that only a very limited span of ion species is actually easy to laser cool. Another reason, which is important for the work in this Thesis, is that continuous laser cooling of a particular ion prohibits that the ion at the same time can be used for quantum optics experiments where the electronic quantum state of the ion is involved. Trapped ions which are not laser cooled directly can be cooled by collisional coupling via the Coulomb interaction to other trapped ions that are directly laser cooled. Applications of this *sympathetic cooling* of ions in linear Paul traps are numerous because the only requirement is that the ions can be trapped simultaneously with a laser coolable ion species. In practice this means that sympathetic cooling in linear Paul traps is applicable to ion species with mass-to-charge ratio in the range 2 to $\sim$ 500 as the laser coolable ions range in mass-to-charge ratio from 9 ($^9Be^+$) to 138 ($^{138}Ba^+$)[1]. This makes sympathetic cooling highly relevant for studies of molecular ions [32, 33],[IV].

Laser cooling of multi-component plasmas containing at least one laser coolable ion species leads in most cases to crystallization of the ion plasma. Crystallized two-component plasmas are also referred to as *bi-crystals*. Earlier experiments have demonstrated that is possible to crystallize an ion plasma with only

[1] See Sec. 2.1 for comments on the stability on ion motion.

$\sim 5\%$ of the ions being directly laser cooled if the mass difference between the two ion species is not too big [34], but generally a larger fraction of laser cooled ions in the plasma is needed for crystallization to occur [35].

In this Thesis we are concerned with multi-component ion Coulomb crystals consisting of different isotopes of singly charged calcium ions. A typical situation is that we have a bi-crystal consisting of $^{44}Ca^+$ ions sympathetically cooled by $^{40}Ca^+$ ions. The pseudopotential in Eq. (2.6) implies that the radial confinement of an ion in the linear Paul trap depends on the ion mass. Specifically the heavier ions ($^{44}Ca^+$) are radially less tightly bound leading to a total radial separation of the two ion isotopes, with the lightest isotope ($^{40}Ca^+$) situated closest to the trap axis surrounded by the heavier isotope ($^{44}Ca^+$). The inner $^{40}Ca^+$ ion core forms a cylindrical structure similar to that of an infinitely long single component crystal, while the outermost shell of the surrounding $^{44}Ca^+$ ions have a spheroidal shape similar to the case of an one component ion Coulomb crystal. The zero-temperature ion density in the crystal is given by Eq. (2.19) for each of the spatially separated ion components in the crystal. This can be derived following the derivation of Eq. (2.19) and taking the total spatial separation of the two components into account.

# 3. EXPERIMENTAL SETUP

In this chapter we introduce the experimental equipment used for the experiments described in chapters 4–6. This equipment also of relevance for the discussion of the light storage in ion Coulomb crystals later in chapters 8–9.

## *3.1 Trap configuration*

The experiments treated in this Thesis were all performed with the linear Paul trap depicted in Fig. 3.1. The trap electrodes are made of gold coated stainless steel and sectioned in three pieces separated by Macor spacers[1]. The electrodes have radii of 4.00 mm, the inter-electrode spacing is $r_0 = 3.50$ mm (see Fig. 2.1), and the center-electrode length is $2z_0 = 5$ mm. This geometry gives rise to an approximately harmonic potential near the center of the linear Paul trap with the axial geometric constant $\eta = 0.248$. The trap is operated at the rf frequency $\Omega_{\mathrm{rf}} = 3.88$ MHz. Further details about the trap are found in N. Kjærgaard's Thesis [36].

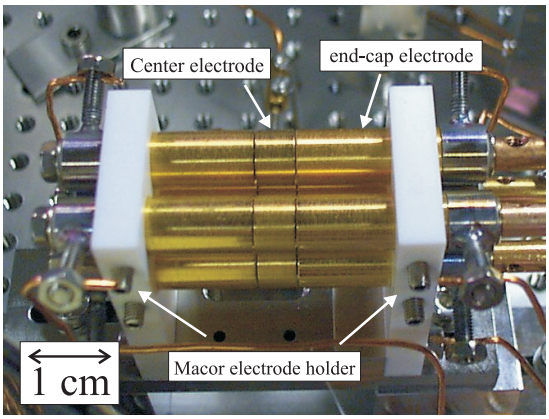


*Fig. 3.1:* Photo of the linear Paul trap installed in the vacuum chamber.

[1] Macor is a non-conducting UHV compatible glass-ceramic material

## 3.2 Vacuum chamber

This section describes the ultrahigh vacuum (UHV) chamber setup in which the linear Paul trap is situated. Figure 3.2 shows a technical drawing and a photograph of the inside of the vacuum chamber. As seen in Fig. 3.2 the UHV chamber consists of a stainless steel cylinder with a diameter of $\sim 30$ cm with 15 CF40-flange ports which are used for different purposes: optical access, electrical feedthrough, pressure measurements, and motion feedthroughs. In the photograph the top flange is not mounted. The top flange is usually the last part of the chamber that is mounted before evacuating. UHV is obtained by baking the chamber at 150°C for a few days while pumping the vacuum chamber with a turbo pump that is connected to the vacuum chamber via a roughing valve. After bakeout the UHV is maintained by an ion getter pump[2] and a sublimation pump. An ion gauge is used for monitoring the pressure. Normal operating pressure is in the range $5 \times 10^{-11}$–$5 \times 10^{-10}$ Torr. Here the different parts of the vacuum chamber labeled in Fig. 3.2 are described:

- *The linear Paul trap* is situated in the center of the chamber. The trap electrode voltages are supplied via copper wires that are connected to the *trap feedthrough*. The details about the linear Paul trap can be found in Sec. 3.1.

- The atomic beam of calcium that crosses the center of the linear Paul trap is produced in the *Ca oven*. The oven consists of a hollow graphite container filled with metallic calcium. The oven is heated by a surrounding coil of tungsten wire. A thermosensor coupled to the graphite is used for monitoring the oven temperature. Normally the operating temperature for the Ca oven is in the range 650–900 K. When the oven is heated a beam of calcium atoms effuse out of a 4–5 mm long canal with a ∅1.0 mm diameter at the front of the graphite container. Skimmers placed between the oven and the linear Paul trap collimate the atomic beam. This is done vertically for the protection of the Paul trap electrodes against contamination from the calcium atoms and horizontally in order to reduce the transverse temperature of the atomic beam. The setup for the *Mg oven* is similar to the Ca oven, but is not relevant for the remainder of the Thesis, because all the experiments described are based on calcium.

- The *oven shutter* is used for blocking the atomic beams. It consists of a stainless steel plate mounted on a rotary motion feedthrough, such that it can be rotated in and out of the blocking position.

- The three laser beam paths drawn in Fig. 3.2(a) indicate the positions of the six anti reflection coated *viewports* that are mounted on the ports for optical access. The 397 nm *cooling laser* and the 866 nm *re-pump beam* for Ca are directed along the Paul trap main symmetry axis. For *transverse cooling* of linear strings of $Ca^+$ ions it is possible to send the 397 nm laser

[2] Leybold IZ270 triode pump

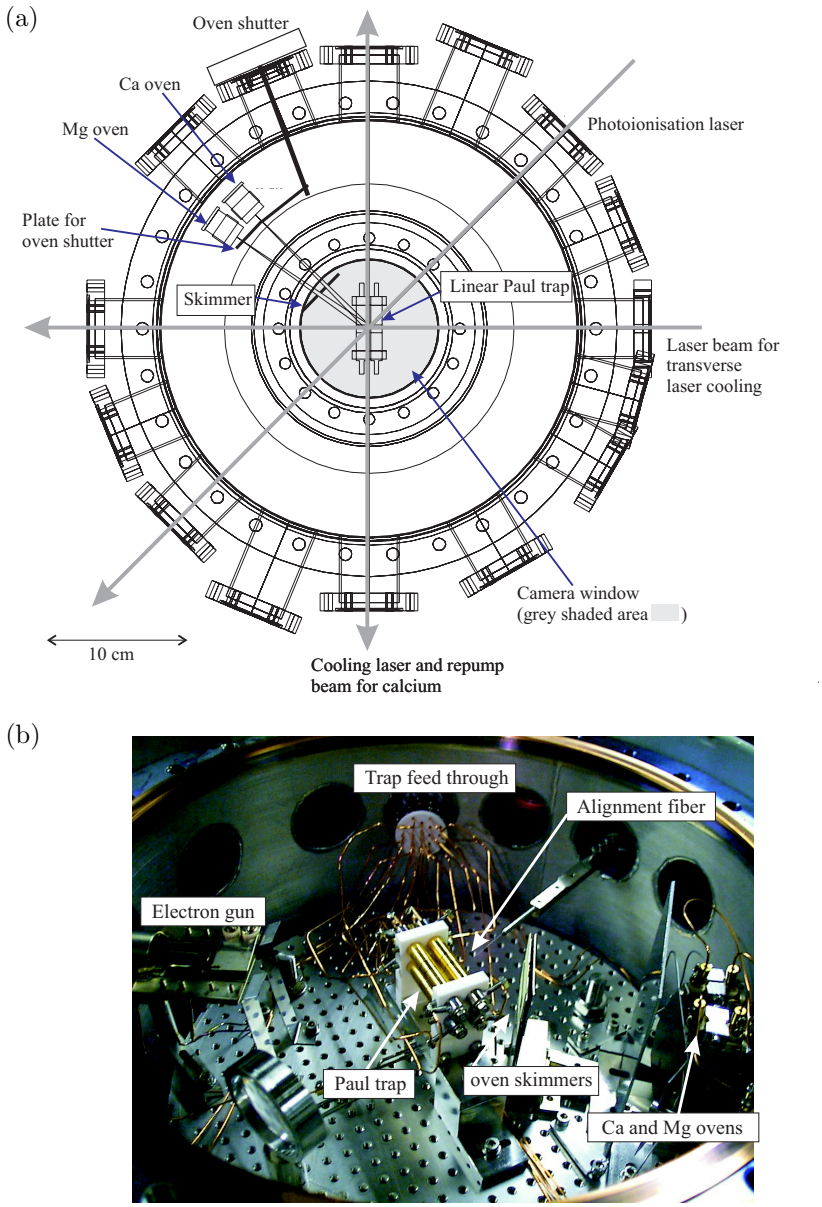


*Fig. 3.2:* (a) Technical drawing of vacuum chamber viewed from above. The 15 ports that points out from the chamber are used for different purposes: windows for accessing the ions with laser beams, electrical feedthroughs, pressure measurements, and motional feedthroughs. (b) Photograph of the UHV chamber with the linear Paul trap installed and the top flange dismounted. The different parts that are labeled in drawing and the picture are described in detail in the text.

in perpendicular to the trap main axis (see Sec. 2.2). The photo-ionization laser is sent in perpendicular to the calcium atomic beam (the reason for this is the main theme in Chap. 4) which is a 45° angle with respect to the Paul trap axis.

- The *alignment fiber* is a small piece of optical fiber with a diameter of 125 $\mu$m mounted on a linear motion feedthrough, which is used to translate the fiber end in and out of the center of the linear Paul trap. The alignment fiber can viewed by the trap camera (see Sec. 3.3) when the cooling laser light is scattered from the tip of the fiber. The alignment fiber is usually used for initial alignment of cooling lasers and when calibrating the length scale of recorded images. There is also installed a window in the top flange through which the ions are viewed with the camera system(see Sec. 3.3).

- A beam of electrons from the *electron gun* (not used in this work) can be send through the Paul trap center for ionization of the atoms in the atomic beam. A set of deflection plates near the electron gun is used for steering the beam of electrons.

## 3.3 Camera system

The ions trapped in the linear Paul trap are imaged by detecting the 397 nm fluorescence that appears when light from the cooling laser is absorbed and spontaneously emitted by the trapped ions. A schematic of the imaging system is seen in Fig. 3.3(a). The fluorescence is first collected by the optics above the trap. The optics consists of an iris that suppresses noise coming from background light in the chamber and a zoom telescope that focuses the light from the ions onto an image intensifier[3]. The basic principle of the image intensifier is that the incoming light causes the emission of electrons from a photocathode. The electrons are then accelerated by an applied DC voltage towards a luminescent phosphor screen on which they are converted back into light. The gain in energy during the acceleration is what causes an amplification of the light signal. To further increase the amplification our image intensifier is equipped with two microchannel plates (MCP) between the photocathode and the phosphor screen. The MCP consist of a thin plate of glass that contains a lot of small ($\sim 10\mu$m) holes. In these holes the number of electrons is increased by successive emission of secondary electrons. In this way multiplication factors of $10^3$–$10^4$ can be obtained with a single MCP. After amplification of the light in the image intensifier the fluorescent image on the phosphor screen is focused onto a charge coupled device (CCD) camera[4] using a Nikon zoom lens[5]. The output from the camera is a 12 bit VGA signal, i.e., 640 pixel × 480 pixel with a range of 4096 grey levels, which can be viewed on a computer, and recorded onto a hard disk.

[3] Proxitronic BV 2581 BY-V 1N
[4] Sensicam CCD camera system from PCO imaging
[5] Nikon AF micro nikkor 60mm/2.8D

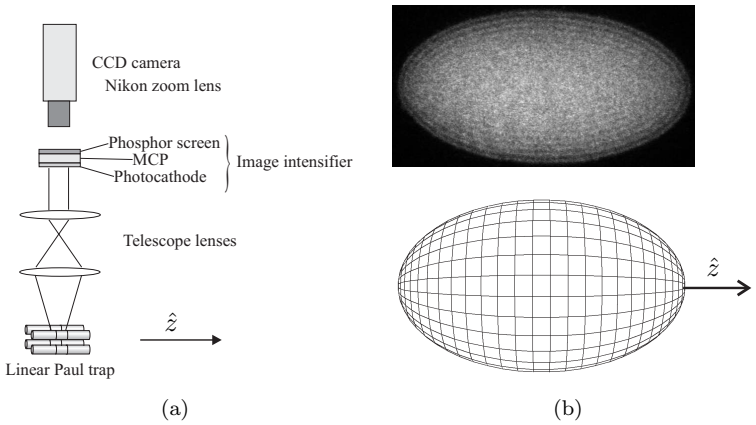


*Fig. 3.3:* (a) Schematics of the camera system. The details are discussed in the text. (b) Typical image of a Doppler cooled one component prolate Coulomb crystal. The orientation of the crystal is indicated with the 3D spheroidal surface plotted below. See also Fig. 2.5. Unless otherwise stated the crystal image in the remainder of this Thesis has this orientation.

A typical image of an one component ion Coulomb crystal is shown in Fig. 3.3(b) together with a surface plot of a spheroid that has approximately the same major axis and minor axis aspect ratio as the Coulomb crystal as well as the same orientation. The $z$-axis, which coincides with the Paul trap axis, is the axis of revolution for the crystal. The projection of the ion crystal is thus shaped as an ellipse. For a review on how the number of ions is determined from such crystal images see App. D.

## *3.4 Laser systems*

The laser systems in our laboratory are used for Doppler cooling of calcium and magnesium ions as well as the production of the ions by photo-ionization of atoms. In this section only the lasers used for calcium will be described, but it should be mentioned that the laser system we use for cooling of magnesium at 280 nm is similar to the laser system we use for photo-ionization of calcium. To give an overview the laser systems used for the Doppler cooling and the production of $Ca^+$ ions a schematic is shown in Fig. 3.4.

There are two stationary home-build wave-meters available in our lab that can measure the wavelengths of all the lasers we have in the lab with a precision up to 7 digits. The wavemeter is based on an interferometer design and a description of the basics of the interferometer can be found in Ref. [37]. Alternatively we can also use optogalvanic spectroscopy (see Ref. [38, 39]) to tune the lasers to the transitions used for Doppler cooling in $Ca^+$.

### 3.4.1 397 nm laser sources

For Doppler cooling of $Ca^+$ laser light at 397 nm is needed (see Fig. 2.4). This is obtained by frequency doubling the output from an 899 Coherent Ti:Sapph laser which is pumped by a Verdi V8 laser. The Verdi V8 laser is a diode pumped, frequency doubled Nd:$YVO_4$ laser providing green light at 532 nm at a maximum output power of 8 W. The output power from the Verdi V8 laser is usually set to 6 W giving $\sim$ 400 mW output power at 794 nm from the Ti:Sapph laser. The Ti:Sapph laser was during these experiments locked to a commercial stabilization cavity with an offset lock giving a laser linewidth of $\lesssim$ 1 MHz. Frequency doubling of the 796 nm light is done in a 12 mm long non-linear Lithium Triborate (LBO) crystal placed in an external bow-tie cavity. An optical Faraday isolator between the Ti:Sapph laser and the bow-tie cavity prevents optical feedback to the Ti:Sapph laser. The bow-tie cavity length is locked using a Hänsch-Couillaud polarization lock, see Ref. [40]. For an input power of 400 mW we usually obtained 20-30 mW of 397 nm blue light.

The generated 397 nm blue light is sent through a series of cylindrical and spherical lenses to obtain a nice round, collimated gaussian beam, when it reaches the trap table. At the trap table the laser light is split using a $\lambda/2$-plate and a polarization beam splitter in order to make two power balanced, counter-propagating cooling laser beams at the ion crystal. A third laser beam for transverse cooling of linear strings of calcium ions is made by further splitting one of the beams again using a $\lambda/2$-plate and a polarization beam splitter.

We also have a blue diode laser operating at 397 nm. This is an extended cavity diode laser with an anti-reflection coated laser diode, where the cavity is constituted by the diode and a grating in a Littrow configuration. The light out-coupled from the laser from the laser is sent through a Faraday isolator and an anamorphic prism for beam shaping. Part of the laser beam is split off by a polarization beam splitter to an external temperature stabilized cavity for frequency stabilization, while the remaining light is sent to the trap table via an optical fiber. We have only obtained a throughput of $\sim$ 30% of the 397 nm laser light in the fibers, but we still chose to use the fiber because it has good characteristics of cleaning the spatial mode of the laser beam. At the trap table the 397 nm diode laser beam is spatially overlapped with the laser beam from the Ti:Sapph laser using orthogonal polarizations of the lasers and a polarization beam splitter.

### 3.4.2 272 nm laser source

For photo-ionization of neutral calcium laser light at 272 nm is needed, see Sec. 4.1. This is obtained by frequency doubling the output from a 699 Coherent dye laser, which is pumped by a Spectra Physics 'BeamLok' Argon ion laser. The output power of the Argon ion laser is usually set to 4–6 W and depending on range of factors this gives an output power of 150–500 mW of 544 nm green laser light from the dye laser. The dye laser was during the experiments locked to a commercial stabilization cavity with an offset lock giving a laser linewidth

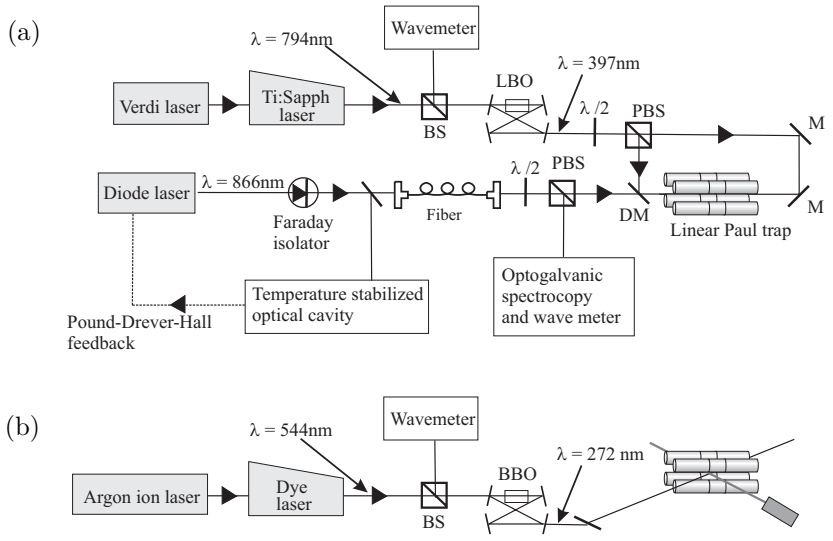


*Fig. 3.4:* (a) Schematics of the laser setup for cooling of $Ca^+$ using the Ti:Sapph laser and the 866 nm laser (basic setup). As we will see later in Chap. 6 it is also possible to simultaneously cool other a different isotope of $Ca^+$ using the 850 nm, the 854 nm laser, and the 397 nm diode lasers, but the schematic presentation of this setup is postponed until Chap. 6. (b) Schematics of the laser setup for photo-ionization of calcium. M: Mirror, DM: Dichroic Mirror, (P)BS: (Polarization) Beam Splitter, $\lambda/2$: half wave plate. See text for details.

of $\sim$ 100 kHz, while the long term fluctuations of the laser frequency are on the order of MHz. Frequency doubling of the 544 nm light is done in a 7 mm long $\beta$-barium borate (BBO) crystal placed in an external bow-tie cavity with a free spectral range of $FSR = 547.3 \pm 6.0$ MHz. The free spectral range of the bow-tie cavity was determined by measuring the optical round trip path length with a Vernier gauge and taking care that the BBO crystal has a refractive index of $n = 1.673$ (see Ref. [41]). The bow-tie cavity length is locked using a Hänsch-Couillaud polarization lock, see Ref. [40]. The output power of 272 nm laser light from the doubling cavity has been measured to be 19 mW at 500 mW pump power, but usually we had only 1–10 mW output power available during the experiments. The 272 nm photo-ionization laser is then shaped by a series of cylindrical and spherical lenses to give a round gaussian beam with a waist of $\sim$ 200 $\mu$m in the interaction region where the calcium ions are produced (see Sec. 4.2). Which gives an average laser intensity of 1–10 W/cm$^2$.

### 3.4.3 Infrared diode laser systems

The three infrared transitions in $Ca^+$ at 850 nm, 854 nm, and 866 nm are all covered by diode lasers. The laser at 854 nm is a commercial diode laser[6], while lasers at 850 nm and 866 nm are home-build diode lasers. The lasers are all extended cavity diode laser systems. The cavity consists of the anti-reflection coated infrared diode placed in a Littrow configuration (see Ref. [42]) with an external grating for feedback. For the home-build laser the grating has 1800 lines/mm. The feedback angle of the grating with respect to the laser diode that determines the lasing frequency is tuned using a piezo-electric transducer giving a scan range on the order of a GHz. Coarse frequency tuning is done by changing the diode current and diode temperature until the desired lasing frequency is within tuning range of the grating-piezo system. The laser light is out-coupled via the direct reflection on the grating and then sent through a Faraday optical isolator and an anamorphic prism pair for beam shaping. The laser light is then sent to the trap table or a wavemeter via an optical fiber.

Frequency stabilization of the 850 nm and 854 nm diode lasers is obtained by locking them to the same external temperature stabilized cavity using the Pound-Drever-Hall locking scheme [43, 44]. The 866 nm is also frequency stabilized to an external temperature stabilized cavity. These temperature stabilized cavities are identical and the cavity drifts are $\lesssim 1$ MHz/hour.

### 3.4.4 Stabilization cavities

Three home-built temperature stabilized optical cavities are used for the frequency stabilization of the laser systems present in our lab. Details about which laser are stabilized to these cavities are mentioned in the description of the laser systems (Sec. 3.4). The stabilization cavities were designed and built by F. K. Jensen [45].

The optical cavity consists of a $\sim$ 25 cm long quartz tube with mirrors attached to each end giving a free spectral range of $\sim$ 600 MHz. Quartz is chosen because it has a low but non-zero thermal expansion coefficient ($\alpha = 0.55 \times 10^6 \mathrm{K}^{-1}$), so the cavity length is tunable by changing the temperature of the quartz tube. Resistance wire has been wound around the quartz tube to provide the temperature stabilization of the quartz tube. The whole cavity is placed inside a vacuum tube for thermal and acoustic noise isolation. The locking scheme used is usually the Pound-Drever-Hall FM locking scheme, but for the 397 nm blue laser an offset lock is used. The short term stability of the cavity system gives a spectral width of $\sim$ 20 kHz, while the long term drift of the cavity is $\sim$ 1 MHz/h.

[6] SDL-TC10 diode laser.

# 4. PHOTO-IONIZATION EXPERIMENTS

In our efforts towards realizing the light memory in Coulomb crystals it is essential for us to develop an efficient loading mechanism for calcium ions in the linear Paul trap. Not only are $\gtrsim 10,000$ ions in these Coulomb crystals needed, but it is also a requirement that specific calcium isotopes can be loaded to produce large bi-crystals consisting of two different isotopes of calcium (see Sec. 2.4). An ion loading technique that offers a solution to these requirements as well as having other nice properties is resonant two-photon photo-ionization trap loading of calcium which was introduced by Kjærgaard *et al.* [36]. Another variant of the two-step loading scheme for calcium was demonstrated in Ref. [46] in which the ions are produced via an auto-ionizing state in calcium.

In order to quantify the efficiency of the loading scheme of Ref. [36] a study of the isotope selectivity of the loading scheme was initialized. In this chapter the results of this study will be presented. The results include measurements of the hitherto unknown isotope shifts of the $4s^2\ ^1S_0 \leftrightarrow 4s5p\ ^1P_1$ transition as well as the hyperfine splitting of the $4s5p\ ^1P_1$ state for $^{43}$Ca. The results in Sec. 4.4 have also been reported in Ref. [III].

## *4.1 Photo-ionization of calcium*

Our approach to photo-ionization of neutral calcium takes its origin in the dipole-allowed 272 nm $4s^2\ ^1S_0 \leftrightarrow 4s5p\ ^1P_1$ transition depicted in Fig. 4.1. The photo-ionization is a two-step process. In the first step a narrow bandwidth CW-laser at 272 nm excites the calcium atom from the ground state $4s^2\ ^1S_0$ to the excited $4s5p\ ^1P_1$ state. From this state the atom is either ionized by absorption of another 272 nm UV-photon or the atom decays. The lifetime of the excited $4s5p\ ^1P_1$ state is 17–60 ns [47] and it decays via two channels: first decay channel is back to the ground state and the second decay channel is to the meta-stable $4s3d\ ^1D_2$ state that has a lifetime of $18.3 \pm 1.4$ ms [48]. According to Smith *et al.* [49] the branching ratio between the first and the second decay channel is $\frac{4s5p\ ^1P_1 \rightarrow 4s^2\ ^1S_0}{4s5p\ ^1P_1 \rightarrow 4s3d\ ^1D_2} \sim \frac{1}{50}$. When the atom is in this metastable $4s3d\ ^1D_2$ state it is still sufficiently close to the ionization threshold that absorption of another 272 nm photon leads to ionization.

The advantage of this scheme is that it relies on a closed system. Provided that the 272 nm laser is sufficiently intense and resonant with the first transition there is a reasonable probability that the atom is in one of the excited states from which absorption of another UV-photon leads directly to ionization.

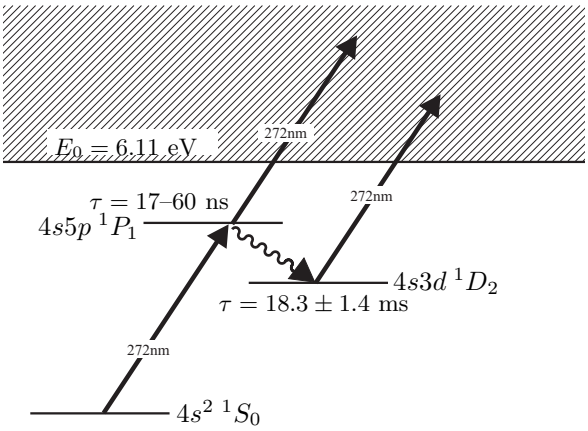


*Fig. 4.1:* Level scheme showing levels in calcium relevant for the photo-ionization of neutral calcium. The ionization threshold is 6.11 eV above the ground state in calcium [50]. The lifetimes of the excited levels are also indicated.

As mentioned in the introduction of this chapter there exist another trap loading scheme demonstrated by Gulde *et al.* [46, 51]. In this scheme the calcium atom is excited via the 423 nm $4s^2\ ^1S_0 \leftrightarrow 4s4p\ ^1P_1$ transition and then subsequently photo-ionized by resonantly exciting to an auto-ionizing state with a 389 nm laser. Using this scheme has the advantage that a higher ion production rate is attainable, due to the much stronger oscillator strength of the $4s^2\ ^1S_0 \leftrightarrow 4s4p\ ^1P_1$ transition compared to the $4s^2\ ^1S_0 \leftrightarrow 4s5p\ ^1P_1$ transition [52]. But the high ion production rate is at the expense of the reduced isotope selectivity of the 423 nm transition [53], which is a critical quantity in the light memory application. The isotope selectivity of the two schemes is discussed in more detail in Sec. 4.6.

## *4.2 Experimental setup*

The experiments on photo-ionization of calcium were performed in the trap setup described in Chap. 3. A schematic overview of the experimental setup for the photo-ionization is shown in Fig. 4.2. The 397 nm and 866 nm lasers, which are directed parallel to the Paul trap axis are used for Doppler cooling of $Ca^+$ ions, and the 272 nm laser is used for photo-ionization of neutral calcium. The output power of the 272 nm laser is typically in the range 1–10 mW. A mechanical shutter controlled by a TTL-signal is placed in the beam path of the 272 nm laser and used for blocking the laser beam. Using the mechanical shutter it is possible to make laser pulses with a square temporal profile and a duration down to $\sim$ 10 ms for which effects of the jitter and the rise time of the shutter still are negligible. In front of the chamber a lens is placed that focuses the beam down to a waist of $\sim 200$ $\mu$m in the region where the photo-

ionization laser beam crosses the calcium atomic beam, giving beam intensities in the range 1–10 W/cm$^2$. After passing the vacuum chamber the power of the photo-ionization laser beam is measured with a photodetector connected to an oscilloscope. This provides information about the average beam power as well as the beam power output stability during one laser pulse.

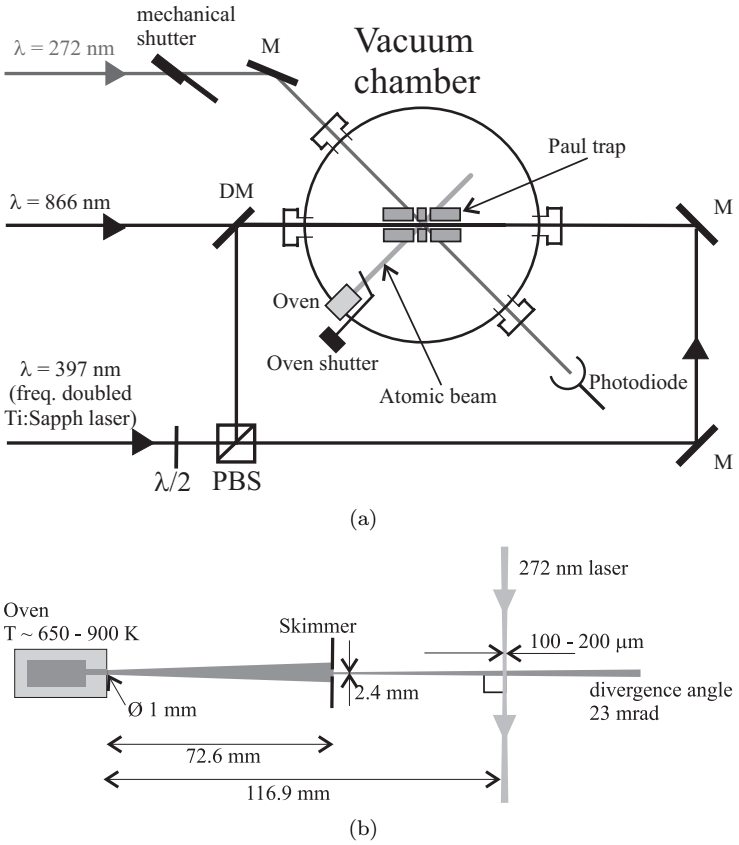


*Fig. 4.2:* (a) Schematic overview of the laser setup and the vacuum chamber geometry for the photo-ionization experiments. M: Mirror, DM: Dichroic Mirror, PBS: Polarization Beam Splitter, $\lambda/2$: half wave plate. (b) Schematic overview of the oven setup, the photo-ionization beam, and the atomic beam as viewed from above. The skimmer height is only a few 100 $\mu$m (not shown in the picture). Further details about the experimental equipment are described in Chap. 3.

The atomic beam effuses from a small orifice in the oven and is afterwards collimated with skimmers to give a beam divergence angle of $\sim$ 23 mrad (see Fig. 4.2(b)). The oven shutter is used for manually blocking the atomic calcium beam. The oven temperatures in these experiments are typically in the range $T$ = 650–900 K giving atomic speeds in the beam direction approximately in

the range of 400–1000 m/s. Transversal to the beam direction the atomic speeds are smaller with a factor set by the beam divergence angle, i.e., the transverse speeds of the atoms are only of the order of 10 m/s. The Doppler broadening of the 272 nm transition in the photo-ionization scheme (see Fig. 4.1) thus depends on the angle between the photo-ionization laser and the atomic beam. In order to reduce the Doppler broadening as much as possible the photo-ionization laser beam direction is perpendicular to the atomic beam direction as shown in Fig. 4.2 making the Doppler width of the $4s^2\ ^1S_0 \leftrightarrow 4s5p\ ^1P_1$ transition in calcium only a few 10 MHz. In comparison there would be both a shift and a broadening of the transition of the order of $\sim$ GHz if the angle between the atomic beam and the laser beam was 45°.

Ions produced in the proximity of the center of the linear Paul trap are trapped with a probability that depends on the speed and the position of the ion at the time it is produced as well as the trap depth which is set by the trapping parameters. The region of the trap where the produced ions are trapped with high probability we refer to as the trapping region. For typical trapping parameters of $U_{\mathrm{rf}} \sim 200$ V, $\Omega = 2\pi \times 3.9$ MHz, and $U_{\mathrm{ec}} \sim 5$ V, the effective trap depth becomes $\sim 1$ eV. This ensures that the ions produced are efficiently trapped despite the initial thermal velocities of the neutral atoms, which corresponds to energies of $\sim 0.1$ eV.

## *4.3 Loading the linear Paul trap using photo-ionization.*

In this section we discuss the applications of the two-photon photo-ionization method presented in Sec. 4.1 and Sec. 4.2. The controlled ion trap loading of large clean $^{40}Ca^+$ Coulomb crystals, small linear ion strings and crystals containing low abundant isotopes of calcium. The production of large bi-crystals consisting of two calcium isotopes is also presented. Here near resonant electron transfer between trapped calcium ions and calcium atoms in the atomic beam is introduced as a technique to control the proportion between the two trapped isotopes in the ion Coulomb crystal.

### *4.3.1 Controlled loading of the linear Paul trap*

The photo-ionization of calcium offers a method to produce large clean crystals of $^{40}Ca^+$ with excellent control of the total number of ions loaded into the linear Paul trap. The sequence shown in Fig. 4.3 demonstrates how we can actually make a $^{40}Ca^+$ crystal of a desired size. The sequence consists of 672 pictures and the camera was gated with a repetition rate of $\sim$ 300 ms. The crystal is loaded with trap parameters $U_{\mathrm{ec}} = 0.7$ V and $U_{\mathrm{rf}} = 2.3$ V giving an ion density of about $0.8 \times 10^8$ ions/cm$^3$. The power of the 272 nm photo-ionization laser is $\sim 2.6$ mW and the laser is detuned a few 100 MHz from the $4s^2\ ^1S_0 \leftrightarrow 4s5p\ ^1P_1$ resonance of $^{40}$Ca.

The graph in Fig. 4.3 shows the number of $^{40}Ca^+$ ions in the crystal as function of time. The nearly constant slope of this graph indicates that the ion loading rate is almost constant and there is no loss of ions. The slope is a bit

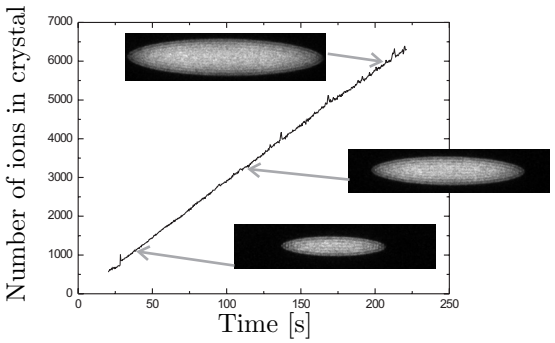


*Fig. 4.3:* Slow loading of a pure $^{40}Ca^{+}$ crystal. Number of ions in the crystal is determined by measuring the volume of the $^{40}Ca^{+}$ crystal. The three crystal images show the crystal at times 33 s, 103 s, and 221 s during the loading sequence.

declining towards the end of the loading sequence which we attribute to the fact that the oven temperature is not constant during the sequence, but actually is $T_{\text{oven}} \sim 472°\text{C}$ at the beginning of the sequence and $T_{\text{oven}} \sim 468°\text{C}$ at the end of the sequence. At $t = 30$ s there is a small kink in the measured crystal size, which can be attributed to the formation dynamics of the trapped crystal.

Impurities in the $^{40}Ca^{+}$ ion crystal such as doubly charged calcium ions, or ions of different species would show up as dark regions in the crystal or a deviation from the expected spheroidal crystal shape of an one component crystal. In the series of crystals shown in Fig. 4.3 there are no signs of impurities in the crystal, which proves that we can indeed load remarkably clean $^{40}Ca^{+}$ crystals using the photo-ionization method.

Another example of the high degree of control of the ion production rate offered by the photo-ionization method is illustrated with the sequence of $^{40}Ca^{+}$ ion strings shown in Fig. 4.4. The oven temperature is $\sim 464°\text{C}$ and the 272 nm laser power is $\sim 12$ mW giving an ion production rate on the order of 10 ions/s. By exposing the calcium atomic beam to the photo-ionization laser with pulses duration $\sim 100$ ms we are able to load on average one $^{40}Ca^{+}$ ion into the same ion string per pulse. In Fig. 4.4 this was done for 1 ion to 5 ions in a string. The fact that we are able to load clean $^{40}Ca^{+}$ strings with this high degree of control is an useful tool for certain quantum computational schemes based upon a few ions in a string [18].

The photo-ionization trap loading method should be compared to electron bombardment which was the method used in the past. Here $Ca^{+}$ ions are produced by collisions between a beam of electrons and the neutral calcium atoms in the atomic beam. Unfortunately the electron beam can also further ionize the $Ca^{+}$ ions to produce $Ca^{++}$ ions, as well as ionize the background atoms, for example, $O_2$ and $CO_2$, which also become trapped, because the charge to mass ratio is not far from the $Ca^{+}$ ion. In order to make large pure single-species crystals the impure crystal can be cleaned by changing the trap

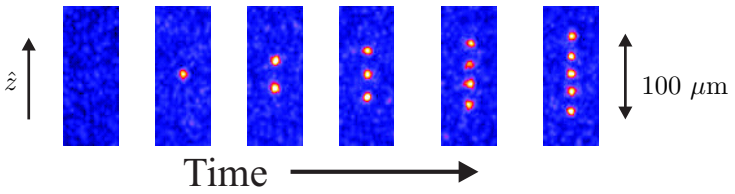


*Fig. 4.4:* Sequence of loading $^{40}Ca^{+}$ into a string one at a time with laser pulses of a duration of 100 ms.

parameters until the $a$ and $q$ parameters of the unwanted ions in the crystal lie outside the Mathieu stability region (see Sec. 2.1) and they are expelled from the trap. This is a very elaborate method of obtaining single-species ion crystals and hence the photo-ionization method is preferred to the electron bombardment method.

In the quantum memory trap which will be presented in Chap. 9, high finesse mirrors are introduced near the trapping region of the linear Paul trap. In this situation the photo-ionization method is superior to the electron bombardment method. One advantage is that it is easy to shape and direct the laser beam such that it does not hit any surfaces near the trap region. In comparison the electron bombardment method usually charges up surfaces near the trap region, which can diminish the ion trapping conditions by introducing stray fields. Another advantage is that the photo-ionization method is many orders of magnitude more efficient than the electron bombardment method. The smaller efficiency of the electron bombardment method implies that in order to have reasonable ion production rates with this method a high atomic flux is needed. This is not an attractive situation when high reflective mirrors are placed near the trapping region, because the atomic beam can contaminate the mirror surfaces and reduce the mirror reflectivity.

### *4.3.2 Trapping low abundant isotopes of calcium*

The fact that the two-step photo-ionization of calcium is a resonant process is a big advantage when other isotopes of calcium than $^{40}Ca^{+}$ need to be trapped. The naturally occurring calcium consists of a mixture of 6 different isotopes: $^{40}$Ca (96.941%), $^{44}$Ca (2.086%), $^{42}$Ca (0.647%), and smaller proportions of, $^{48}$Ca (0.187%), $^{43}$Ca (0.135%), and $^{46}$Ca (0.004%). From these abundances it is clear that either an isotope enriched sample of calcium or a trap loading method that can distinguish between the different calcium isotopes is necessary in order to load other isotopes than $^{40}Ca^{+}$. Using the two step photo-ionization we can pursue the latter method in a scheme which we refer to as *isotope selective photo-ionization*.

The photo-ionization scheme is isotope selective because the resonance frequency of the first transition in the photo-ionization depends on the isotope, i.e., there is an isotope shift of the transition frequency. As we will study in more detail later in the present chapter the typical isotope shift of the photo-

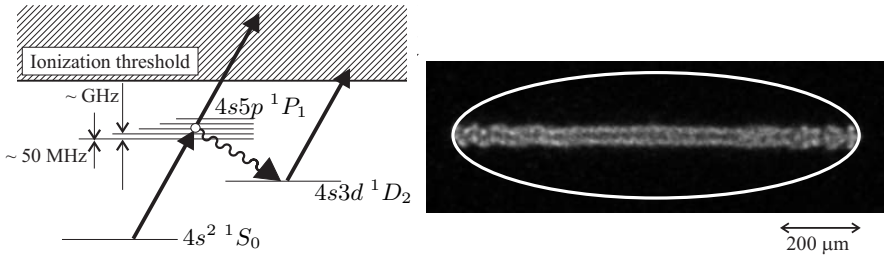


(a) Calcium level scheme (b) $^{40}Ca^{+}$–$^{44}Ca^{+}$ bi-crystal

*Fig. 4.5:* (a) Level scheme illustrating the basics in the isotope-selective scheme. The lines at the $4s5p\ ^1P_1$ state illustrate the shifted resonances of the different isotopes. (b) Bi-crystal consisting of $^{40}Ca^{+}$ (fluorescing) and $^{44}Ca^{+}$ ions(non-fluorescing). Total number of ions in the crystal is $\sim 1500$ ions. The white line indicates the actual boundary of the full crystal.

ionization transition $4s^2 \leftrightarrow 4s5p$ in calcium is on the order of GHz. In the special case of $^{43}$Ca which is the only naturally occurring calcium isotope with non-zero nuclear spin ($I = 7/2$) and therefore has a hyperfine splitting of the excited $4s5p$-state the neighboring isotope resonances, $^{42}$Ca and $^{44}$Ca, are still a couple of 100 MHz away. The linewidth of the 272 nm photo-ionization laser is on the order of 1 MHz while the natural width of the $4s^2 \leftrightarrow 4s5p$ transition is a few MHz. The width of the first transition in the photo-ionization of calcium is thus clearly dominated by the Doppler width of $\sim 50$ MHz, which originates from the transverse velocity spread of the atomic beam effusing from the oven (see Sec. 4.2). Comparing the typical isotope shift ($\sim$ GHz) with the total spectral width ($\sim 50$ MHz) of the first transition we see that the photo-ionization laser can selectively excite the different isotopes of calcium. The basics of the isotope selective loading described is illustrated in Fig. 4.5(a).

Figure 4.5(b) shows a typical image of a bi-crystal (see Sec. 2.4) loaded when the photo-ionization laser is tuned near the $4s^2 \leftrightarrow 4s5p$ resonance of the $^{44}$Ca atom. In this experiment only the $^{40}Ca^{+}$ ions are directly laser cooled, while the $^{44}Ca^{+}$ ions are sympathetically cooled by the $^{40}Ca^{+}$ ions exchanging their kinetic energy via the Coulomb interaction (see Sec. 2.4). Therefore only fluorescence from the $^{40}Ca^{+}$ ions is observed, while the presence of the $^{44}Ca^{+}$ ions in this image have to be inferred from the tube shape of the $^{40}Ca^{+}$ ions. In many of the experiments described in this Thesis we need to count the total number of ions in the crystal. This is done by using near resonant electron transfer between trapped $^{44}Ca^{+}$ ions and $^{40}$Ca atoms in the atomic beam to convert the bi-crystal into a nearly pure $^{40}Ca^{+}$ ion crystal, which is the theme of Sec. 4.3.3.

### 4.3.3 Near resonant electron transfer

In this section we will describe how the phenomenon of near resonant electron transfer is used as an useful ion detection tool in the experiments described in this Thesis. Near resonant charge transfer in our linear Paul trap occurs when a neutral calcium atom from the atomic beam collides with one of the trapped calcium ions and in this collision process exchanges an electron. The incoming atom is thus ionized and subsequently trapped, while the initially trapped ion becomes a neutral atom and is no longer confined by the trapping potentials.

The possible charge transfer processes between the calcium isotopes are summarized by the following reaction formulas

$$^{A}\mathrm{Ca} + {}^{A}\mathrm{Ca}^{+} \rightarrow {}^{A}\mathrm{Ca}^{+} + {}^{A}\mathrm{Ca} \qquad \text{(symmetric)}, \tag{4.1}$$

$$^{A}\mathrm{Ca} + {}^{A'}\mathrm{Ca}^{+} \rightarrow {}^{A}\mathrm{Ca}^{+} + {}^{A'}\mathrm{Ca} + \Delta E \qquad \text{(asymmetric)}, \tag{4.2}$$

where $A$ and $A'$ are the atomic mass numbers of the calcium isotopes and $A \neq A'$. In the asymmetric case the energy deficiency denoted by $\Delta E$ comes from the isotope shift of the ground state level relative to the atom's ionization limit for the atoms $^{A}$Ca and $^{A'}$Ca. According to Lorenzen *et al.* [54] this deficiency is $\Delta E \sim 13 \times 10^{-6}$ eV for $A = 40$ and $A' = 48$[1], so the reaction described in Eq. (4.2) is truly near resonant when compared to the typical kinetic energy of a calcium atom in the atomic beam.

The fact that $^{40}$Ca is by far the most abundant of the 6 naturally occurring calcium isotopes (96.941%) directly influences which electron transfer reactions are observed in the ion crystal. Assuming that a crystal consisting dominantly of the isotope $^{A}\mathrm{Ca}^{+}$ has been loaded, where $A \neq 40$, the most frequent occurring asymmetric reaction is

$$^{40}\mathrm{Ca} + {}^{A}\mathrm{Ca}^{+} \rightarrow {}^{40}\mathrm{Ca}^{+} + {}^{A}\mathrm{Ca} + \Delta E, \tag{4.3}$$

and this process will reach an equilibrium when the relative occurrence of $^{40}\mathrm{Ca}^{+}$ in the crystal reflects the natural abundance of $^{40}$Ca. Usually the cooling lasers are tuned to the $^{40}\mathrm{Ca}^{+}$ ions, and therefore only this particular isotope is visible on the images of the crystals. Detection of the $^{40}\mathrm{Ca}^{+}$ part of the crystal is readily available, because this particular isotope, being the lightest, is situated closest to the trap axis and the volume of this part of the crystal can be found with the technique described in Appendix D.

In Fig. 4.6 charge transfer in a small bi-crystal of $^{40}\mathrm{Ca}^{+}$–$^{44}\mathrm{Ca}^{+}$ ions is demonstrated. The density of ions in the crystal is about $0.5 \times 10^{-8}$ cm$^{-3}$ and the total number of ions in the crystal is $\sim 250$. The small bi-crystal is first produced by resonant photo-ionization of $^{44}$Ca atoms. In the ion production stage some of the produced $^{44}\mathrm{Ca}^{+}$ ions are already exchanged with $^{40}\mathrm{Ca}^{+}$ ions by electron transfer with $^{40}$Ca atoms in the atomic beam. Then the oven and the photo-ionization laser are blocked. The cooling lasers are tuned to the

[1] The main contribution to the isotope level shift of the ground state comes from the Bohr mass shift which is given by $-\frac{m}{M}E$ for an isotope of mass $M$, binding energy $E$. The electron mass is $m$.

$^{40}Ca^+$ cooling transition and the ions crystallize, i.e., the $^{44}Ca^+$ ions are cooled sympathetically by the $\sim$ 25 laser cooled $^{40}Ca^+$ ions. At $t \sim 0$ the oven is un-blocked again so the ion crystal is bombarded with thermal atoms from the atomic beam and the charge transfer starts. The oven temperature during the charge transfer is $T \sim 533°C$. In Fig. 4.6 it is seen how the number of $^{40}Ca^+$ ions increases until the crystal nearly a pure $^{40}Ca^+$ crystal at $t \sim 80$ s. The number of $^{40}Ca^+$ ions are determined from the volume of the fluorescing $^{40}Ca^+$ part of crystal assuming that the different isotopes are completely spatially separated.

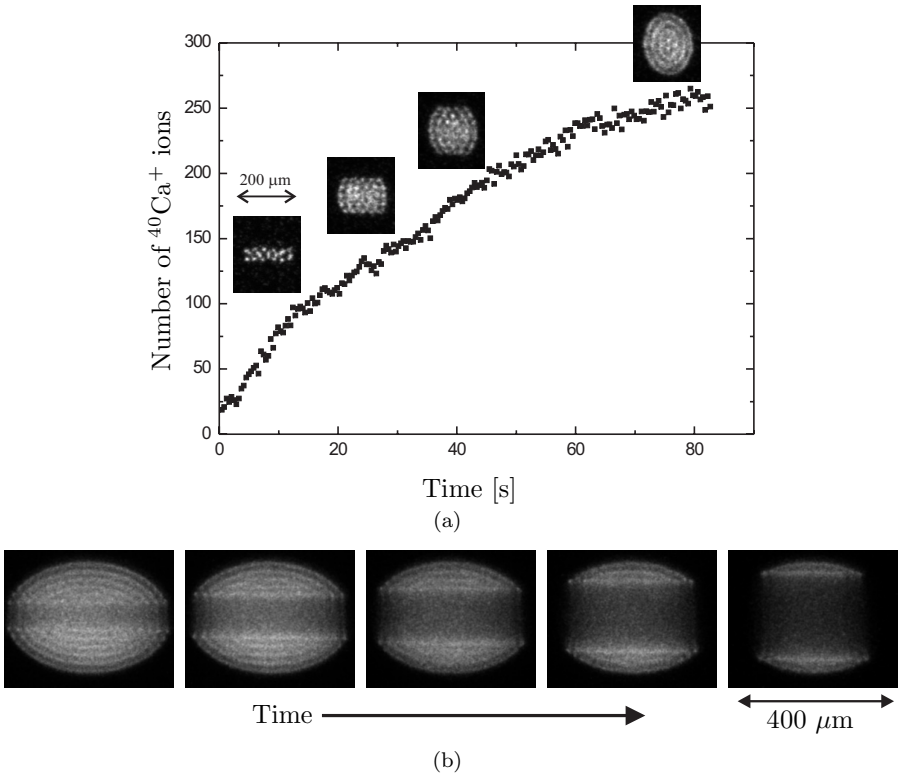


*Fig. 4.6:* (a) Charge transfer in a $^{40}Ca^+$–$^{44}Ca^+$ bi-crystal containing $\sim$ 250 ions, where the $^{40}Ca^+$ ions are laser cooled. The inserted pictures shows the crystal at different times in the charge transfer process. The graph shows the number of $^{40}Ca^+$ ions in the crystal. (b) Series of images illustrating charge transfer in a $^{44}Ca^+$–$^{40}Ca^+$ bi-crystal consisting of $\sim$ 1300 ions, where the $^{44}Ca^+$ ions (fluorescing) are laser cooled. The 5 images were recorded at times $t \sim (0, 5, 9, 18, 34)$ s after the oven was opened. Further details are described in the text.

The presence of $^{44}Ca^+$ ions in the crystal is typically inferred from the shape of the laser cooled $^{40}Ca^+$ ion plasma, but to prove that they actually are $^{44}Ca^+$ ions we can tune the cooling lasers to the $^{44}Ca^+$ cooling transitions and record

the fluorescence from the $^{44}Ca^{+}$ ions instead. In the image series shown in Fig. 4.6 (b) the $^{44}Ca^{+}$ ions are cooled directly using the Ti:Sapph laser system for generating cooling light at 397 nm and the 866 nm diode laser for the repump laser light (see Fig. 2.4). The oven temperature is $T \sim 533.8°C$, which should give the approximately same charge transfer rate as in Fig. 4.6(a). The whole sequence in Fig. 4.6(b) takes about 35 s and shows the evolution of the crystal from a $^{44}Ca^{+}$ ion crystal that only contains a small cylindrically shaped core of $^{40}Ca^{+}$ ions to a crystal mainly consisting of $^{40}Ca^{+}$ ions.

In Sec. 4.4 charge transfer will prove to be a very valuable tool when we need to determine the total number of ions loaded as a function of the photo-ionization laser frequency. The reason for this is that by using charge transfer to transform the calcium ion bi-crystals into almost pure $^{40}Ca^{+}$ ion crystals the total number of ions in the crystals can be counted using only the cooling laser system for $^{40}Ca^{+}$ ions, which reduces the technical complexity of the experiments considerably.

## 4.4 Experimental results

The results presented in this section were obtained using the techniques discussed in Sec. 4.3. Our goal with the experiments is to study the loading rate of the ion trap as a function the frequency of the 272 nm photo-ionization laser. The loading rate scans are interesting from an experimental point of view because these provide information about the isotope selectivity of the photo-ionization loading. From a more fundamental atomic physics point of view these measurements are also interesting as they reveal the isotope shifts of the $4s^2\ ^1S_0 \leftrightarrow 4s5p\ ^1P_1$ transition of all naturally occurring calcium isotopes and the hyperfine splitting of the $4s5p\ ^1P_1$ state for $^{43}Ca$. This will be treated later in Sec. 4.5.

### 4.4.1 Photo-ionization rate measurements

Figure 4.7 shows the measured photo-ionization rate as a function of the photo-ionization laser detuning. Each data point in the graphs represents a measurement of the trap loading rate for a particular detuning of the photo-ionization laser. In the following the measurement procedure for producing scans similar to the two shown in Fig. 4.7 is described. The basic experimental setup for these measurements is described in Sec. 4.2. At a given detuning of the photo-ionization laser the trap loading rate is measured by exposing the atomic beam to the photo-ionization laser beam for a certain time controlled by the mechanical shutter. The cooling lasers are tuned to the cooling transition in $^{40}Ca^{+}$ ions and as the ions get cold enough they crystallize. Generally, when the photo-ionization laser is tuned in between the resonances of the various isotopes two or more singly charged calcium isotope ions will be produced and trapped. The number of ions in the multi-component crystal could in principle be determined by imaging the fluorescence from the individual isotopes. This is, however experimentally very challenging as each isotope needs its own set

of laser frequencies due to the isotope shift of the cooling transitions. As an alternative route to quantify the total ion production, we choose to expose the multi-component crystals to the thermal beam of calcium atoms until nearly all the ions ($\sim 97\%$) have been converted into $^{40}Ca^{+}$ ions by near resonant charge transfer collisions as described in Sec. 4.3.3. The total number of ions initially produced and trapped by the photo-ionization can now be counted by measuring the size of the now nearly pure $^{40}Ca^{+}$ crystal. After saving the pictures of the final crystal to hard disk the linear Paul trap is initialized for a new measurement simply by switching trapping potentials off and on which will empty the ion trap for the trapped ions.

The scans similar to the two shown in Fig. 4.7 are obtained by manually tuning the photo-ionization laser in steps of $\sim 10$ MHz and for each step measuring the trap loading rate using the procedure described above. The oven temperature during the scans is approximately $\sim 600°$C. These high temperatures are chosen in order to have high calcium atom flux which gives a rapid conversion of the crystal into a nearly pure $^{40}Ca^{+}$ ion crystal through the near resonant charge transfer. Another reason for choosing the high oven temperature is that we need a relative high ion production rate in order to trap a sufficient amount of ions for the detection of the weak $^{46}Ca^{+}$ ion resonance. During each scan the oven temperature is kept stable within $\pm 2°$C corresponding to a maximum uncertainty of the density of the atomic beam of $\pm 7\%$ during a typical data acquisition time for one scan which is on the order of an hour. Since the time to measure a single resonance is only a fraction of this time, any systematic errors in the resonance profiles due to fluctuating oven temperatures can be neglected. The error bars seen in Fig. 4.7 take three effects into account. First, due to intensity fluctuations of the laser intensity there will be a fluctuation in the number of ions produced. Since for neighboring data points around a resonance this intensity fluctuation is maximally a few percent, the expected square dependence on the intensity of the ion production leads to an estimated uncertainty of $\sim 5\%$. Second, in determination of the Coulomb crystal volumes, both systematic and random uncertainties due to the measurements of the main axis of the elliptical projections of the crystals occur. Both these errors are of about 5%, but since the systematic errors are equal for points symmetrically positioned around a resonance, it will have a small effect on the determination of the resonance frequencies. Hence, in our analysis, we have only accounted for the random errors of 5%. Finally, due to the finite number of ions produced within one measurement, we have included an uncertainty of the square root of the estimated number of ions.

### *4.4.2 Normalized scan*

The photo-ionization rate measurements presented in Sec. 4.4.1 depends on the output power of the photo-ionization laser. As the output power of this laser is not stable throughout the scan we need to normalize the ionization rates in order to obtain scan profiles that are independent of the laser output power. If we assume that neither the $4s^2\ ^1S_0 \leftrightarrow 4s5p\ ^1P_1$ transition nor the following photo-

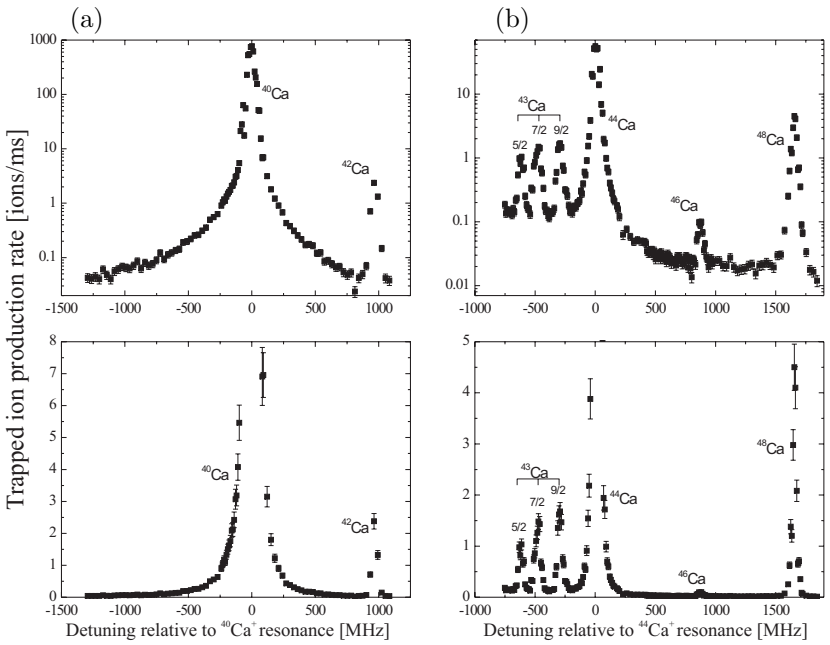


*Fig. 4.7:* Two scans of the trapped ion production rate plotted as function of the photo-ionization laser detuning. (a) A scan of the $^{40}$Ca and the $^{42}$Ca resonance. (b) A scan from the three hyperfine resonances of the $^{43}$Ca atom to the $^{48}$Ca resonance. The calcium oven temperature is (a) $T_{\text{oven}} = 612°\text{C}$ , and (b) $T_{\text{oven}} = 602°\text{C}$, and the power of the photo-ionization laser is (a) $P = 5.5$–$9.5$ mW, and (b) $P \sim 11$ mW. The data points in these plots have not been corrected for the variation in output power of the photo-ionization laser. The scans are both presented in a logarithmic and a linear plot.

ionization process is saturated, we can expect to see an ion production rate that is proportional to the laser intensity squared. We tested this assumption by measuring the ion production rate as a function of the photo-ionization laser output power, which is shown in Fig. 4.8. The photo-ionization laser is tuned approximately to the $4s^2\ ^1S_0 \leftrightarrow 4s5p\ ^1P_1$ transition of $^{40}\text{Ca}^+$. We then measure the number of ions loaded into the trap when the exposure time of the photo-ionization laser is 100 ms as function of the photo-ionization laser power. The oven temperature is $T = 579°\text{C}$ for the measurement in the $P \sim 0.5$–$2.5$ mW range and $T = 416°\text{C}$ for the measurement in the $P \sim 2.5$–$14$ mW range. The data points in the graphs are fitted with the function $y = aP^b$, where $a$ and $b$ are fitting parameters and $P$ is the power of the photo-ionization laser. The noticeable fluctuation of the data points around the fitted curves seen in Fig. 4.8 must come from a fluctuation that we have not accounted for in the error bars. We believe that this fluctuation originates from a slow frequency drift of the photo-ionization laser which, depending on how close the laser is tuned to the

$^{40}$Ca resonance (see Fig. 4.7 (a)), will appear as a fluctuation in the number of trapped ions. Accounting for this slow drift in the trapped ion production rate the exponents, $b$, found in the two fits in Fig. 4.8 of $b = 2.18 \pm 0.06$ and $b = 1.90 \pm 0.09$ does not seem to contradict our assumption that the photo-ionization rate depends on the square of the photo-ionization laser power.

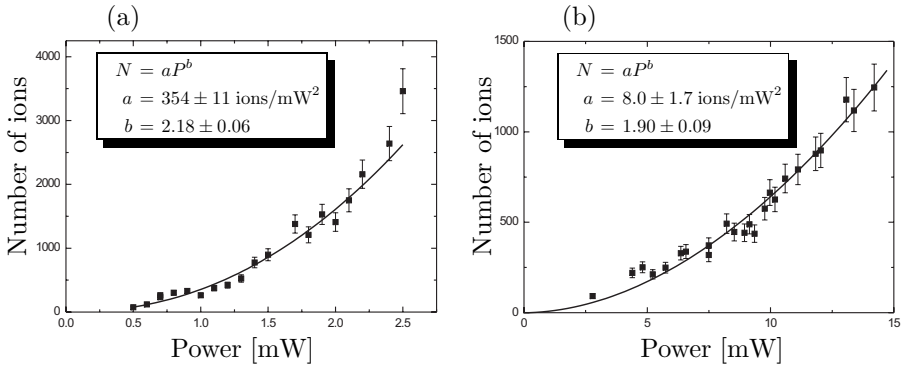


*Fig. 4.8:* Number of trapped ions produced with a laser pulse of a duration of 100 ms as a function of the laser power. Oven temperature is (a) $T = 579°$C and (b) $T = 416°$C.

Three partially overlapping normalized frequency scans are presented in Fig. 4.9. The three data-series were measured at slightly different oven temperatures: $T_{\text{oven}} = 612°\text{C}(\triangle)$, $T_{\text{oven}} = 630°\text{C}(\blacksquare)$, and $T_{\text{oven}} = 602°\text{C}(\square)$, while the photo-ionization laser power was $P = 5$–$9$ mW($\triangle$), $P = 8$–$9$ mW($\blacksquare$), and $P = 8.5$–$9$ mW($\square$).

The relative rates of the $\triangle$-data and the $\blacksquare$-data have been normalized, so they share the same fitted maximum value and position at the $^{42}$Ca resonance peak. In the same way the data indicated by $\blacksquare$ and $\square$ have been normalized to the three $^{43}$Ca hyperfine peaks.

The Doppler broadening of the resonances, which only depends slightly on the atomic mass, is best found by fitting the $^{40}$Ca resonance data to a Voigt profile fit. In Fig. 4.10 the Voigt profile fit is plotted in two double logarithmic plots in order to illustrate how the Lorentzian behavior of the profile becomes significant far away from the resonance frequency, while the Gaussian behavior dominates in the vicinity ($\sim$ 100 MHz) of the resonance. The Voigt profile fit of the resonance has a FWHM of 52 MHz, which consists of a Gaussian contribution of $w_{\text{G}} = 47.8 \pm 0.8$ MHz and a Lorentzian contribution of $w_{\text{L}} = 7.3 \pm 0.3$. This means that the FWHM of the resonance is clearly dominated by the Doppler broadening of the resonance. A Gaussian width of $\sim 50$ MHz is what we would expect from the oven geometry and an oven temperature of $\sim 612°$C.

If we assume that the first transition of the photo-ionization is not saturated, a Lorentzian contribution of $w_{\text{L}} = 7.3 \pm 0.3$ MHz corresponds to a lifetime of $\tau_{4s5p} = 21.8 \pm 0.9$ ns for the excited $4s5p\ ^1P_1$ state. If the first transition is

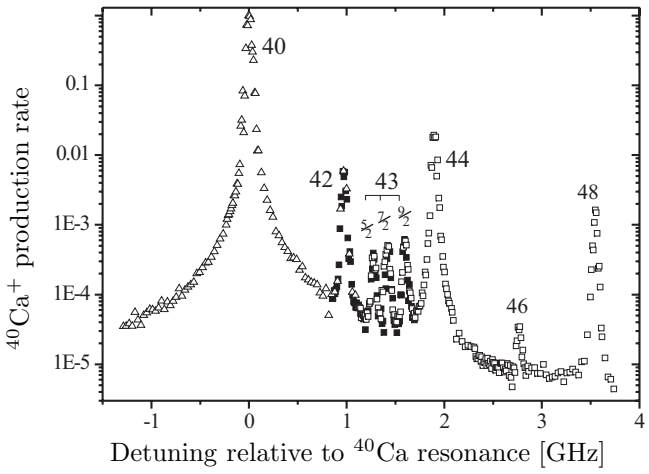


*Fig. 4.9:* Three partially overlapping frequency scans covering all the naturally occurring calcium isotopes. The scan ranges are $^{40}$Ca–$^{42}$Ca (△), $^{42}$Ca–$^{43}$Ca (■), and $^{43}$Ca–$^{48}$Ca (□).

saturation broadened the measured lifetime is shorter than the actual lifetime. It is interesting to compare this lifetime estimate with the lifetime that have been calculated or measured by others. The calculation of the $4s5p\ ^1P_1$ lifetime have been performed by Refs. [47, 52, 55], and they predict lifetimes of $\tau_{4s5p} = 57.6$ ns [47], $\tau_{4s5p} = 59.2$ ns [52], and $\tau_{4s5p} = 42.21$ ns [55]. The three calculations all predict a longer lifetime than the lifetime measured by us, which might imply that there is power broadening in our measurement. For the experimental work there are to our knowledge only reported two $4s5p\ ^1P_1$ lifetime measurements. These also disagree with the theoretical work yielding lifetimes of $\tau_{4s5p} = 16.6 \pm 2.0$ ns (Smith and Liszt [56]) and $\tau_{4s5p} = 20.07 \pm 1.15$ ns (Mathur and Kelly [57]). Our measurement disagrees slightly with the value determined by Smith and Liszt, while it is in good agreement with the value found by Mathur and Kelly.

## *4.5 Isotope shifts and hyperfine splitting*

Isotope shifts and hyperfine splitting of optical transitions provide valuable information about atomic electron configurations and properties of the nuclei. While nuclear charge distributions can be deduced from the isotope shifts (see, e.g., Refs. [58, 59]), the nuclear spins, magnetic dipole moments, and electric quadrupole moments can be determined from the hyperfine splitting [60].

Although isotope shifts and hyperfine splitting already have been measured for a large number of transitions in neutral Ca (see Refs. [61–63] and references therein) and in singly charged $Ca^+$ ions [23, 64, 65] the $4s^2\ ^1S_0 \leftrightarrow 4s5p\ ^1P_1$ transition considered here has hitherto not been studied experimentally.

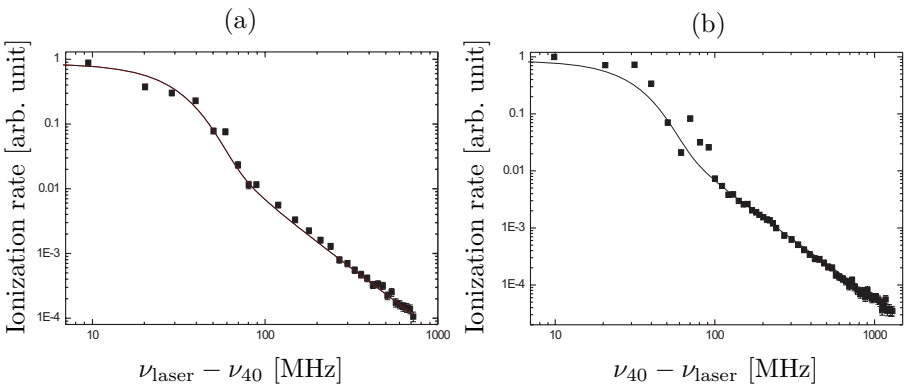


*Fig. 4.10:* Voigt profile fit of the $^{40}$Ca $4s^2\ ^1S_0 \leftrightarrow 4s5p\ ^1P_1$ resonance showing the photo-ionization laser blue detuned (a) and red detuned (b) from the resonance. The resonance frequency is denoted by $\nu_{40}$ and the laser frequency is $\nu_{\rm laser}$. The total resonance area found by integration of the peak is $50.3\pm1.8$ MHz. The fit parameters are the Lorentzian linewidth, $w_{\rm L} = 7.3\pm0.3$ MHz, and the Gaussian width, $w_{\rm G} = 47.8 \pm 0.8$ MHz.

### *4.5.1 Isotope shifts*

Before deriving the isotope shifts from data like the ones presented in Fig. 4.9, the uncertainty of the individual data points has to be estimated and taken into account. In Sec. 4.4.2 we concluded that three error sources must be taken into account. The three sources were power fluctuations of the photo-ionization laser ($\sim 5\%$), error in determining the correct number of ions in the crystal ($\sim 5\%$), and finally the number fluctuation which are just the square root of the number of trapped ions. When these uncertainties are accounted for in a weighted least squares Gaussian fit, the uncertainty on the resonance position is less than 2 MHz.

A more critical error arises when we compare similar scans. Here we find that the measured resonance peak positions are associated with much larger uncertainties than the ones from the Gaussian fits. This additional error originates from local frequency drift of the photo-ionization laser during a whole scan which typically lasts about 40 min. From a series of scans, we have found that this laser drift error leads to a RMS uncertainty in the resonance frequencies of about 9 MHz. An unimportant error of a few hundred kHz is introduced due to the fact the resonance frequencies have been determined from single Gaussian fits instead from a more realistic multi-peak Voigt profile fit. In addition to these statistical errors, there is also an systematic uncertainty of $\pm1\%$ arising from the calibration of the photo-ionization laser frequency scan to an optical spectrum analyzer with a known free-spectral-range.

The measured isotope shifts of the $4s^2\ ^1S_0 \leftrightarrow 4s5p\ ^1P_1$ transition with respect to the $^{40}$Ca resonance are given in Table 4.1. The isotope shift for $^{43}$Ca has been found as the center of gravity for the three hyperfine components of the

| Mass, $A$ | Shift [MHz] |
|---|---|
| 42 | $967 \pm 9$ |
| 43 | $1455 \pm 9$ |
| 44 | $1879 \pm 14$ |
| 46 | $2746 \pm 16$ |
| 48 | $3528 \pm 16$ |

*Tab. 4.1:* Isotope shifts of the $4s^2\ ^1S_0 \leftrightarrow 4s5p\ ^1P_1$ transition in calcium derived from the experimental data like the ones presented in Fig. 4.9. All shifts are with respect to the $^{40}$Ca resonance. The errors stated represent one standard deviation originating from the statistical errors in the experiments. In addition, the shifts are subject to an overall linear scaling uncertainty of 1% due to our frequency scan calibration (see text). The isotope shift for $^{43}$Ca is the center of gravity of the hyperfine components.

transition. The center of gravity and the hyperfine splitting will be discussed in Sec. 4.5.3.

### *4.5.2 Field shift and mass shift*

The isotope shift for a given transition is usually described as a sum of the mass and the field shift in the following way [58]

$$\delta\nu^{AA'} = M\frac{A'-A}{AA'} + F\delta\langle r^2\rangle^{AA'}, \tag{4.4}$$

where $M$ is the mass shift coefficient, $A$ and $A'$ denote the atomic masses of the two isotopes, $F$ is the field shift coefficient, and $\delta\langle r^2\rangle^{AA'}$ is the difference in mean square nuclear charge radii between the isotopes.

The mass shift is usually written as a sum of the normal mass shift (NMS) and the specific mass shift (SMS), which means that we can write the mass shift coefficient as $M = M_{\mathrm{NMS}} + M_{\mathrm{SMS}}$. Here the NMS coefficient is given by the simple expression $M_{\mathrm{NMS}} = \nu_0 m_e/m_u$, where $\nu_0$ is the transition frequency, $m_e$ is the electron mass and $m_u$ is the atomic mass unit. The NMS originates from the reduced mass correction for the electron, while the SMS comes from the change in the correlated motion of all the electrons (see, e.g., Ref. [66]). Subtraction of the NMS from the total isotope-shift gives the residual isotope shift (RIS),

$$\delta\nu_{\mathrm{RIS}}^{AA'} = M_{\mathrm{SMS}}\frac{A'-A}{AA'} + F\delta\langle r^2\rangle^{AA'}. \tag{4.5}$$

Rewriting Eq. (4.5) by multiplication by the factor $AA'/(A'-A)$ leads to

$$\frac{A'A}{A'-A}\delta\nu_{\mathrm{RIS}}^{AA'} = M_{\mathrm{SMS}} + F\left(\frac{A'A}{A'-A}\delta\langle r^2\rangle^{AA'}\right), \tag{4.6}$$

which shows that $M_{\mathrm{SMS}}$ and $F$ can be determined from a linear fit when the $\delta\langle r^2\rangle^{AA'}$'s are known. In Fig. 4.11 the left hand side of Eq. (4.6) is shown as

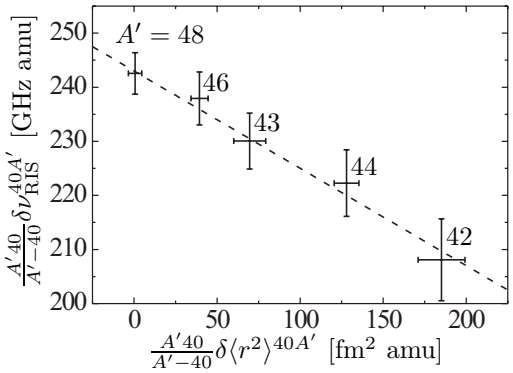


*Fig. 4.11:* Plot of the values $\frac{A'40}{A'-40}\delta\nu_{\rm RIS}^{40A'}$ derived from the measurements as function of $\frac{A'40}{A'-40}\delta\langle r^2\rangle^{40A'}$ for the $4s^2\ ^1S_0 \leftrightarrow 4s5p\ ^1P_1$ transition in Ca. The dashed line is a weighted linear regression fit to determine the coefficients $M_{\rm SMS}$ and $F$ from the relation given in Eq. (4.6).

function of $\frac{A'A}{A'-A}\delta\langle r^2\rangle^{AA'}$ for the fixed value of $A = 40$ and using the measured isotope shifts given in table 4.1. The root mean square charge radii from Ref. [59] used in the calculation of $\delta\langle r^2\rangle^{AA'}$ have been listed in Appendix A. The SMS coefficient and field shift coefficient, obtained by weighted linear regression fit to the data points in Fig. 4.11, are listed in Table 4.2.

Inasmuch as the neither the field shift coefficient nor the specific mass coefficient have earlier been measured or calculated for the $4s^2\ ^1S_0 \leftrightarrow 4s5p\ ^1P_1$ transition, a direct comparison with earlier results is not possible. It is though worth mentioning that the field shift coefficient for the $4s^2\ ^1S_0 \leftrightarrow 4s5p\ ^1P_1$ transition (Table 4.2) is, within the stated error, almost equal to the experimentally determined field shift coefficient for the $4s^2\ ^1S_0 \leftrightarrow 4s4p\ ^1P_1$ transition of $F = -175.8 \pm 1.2$MHz/fm$^2$ reported in [62]. Indeed the two field shifts are expected to be almost identical. The reason is that the $4p$ and $5p$ electrons have negligible overlap with the nucleus compared to the $4s$ electron in the ground state of the transition and hence the $4p$ and $5p$ electrons only contribute insignificantly to the total field shift of the transition. Therefore the main contribution to the field shift comes from the excitation of the $4s$ electron into a $np$ state independent of the quantum number $n$.

### *4.5.3 $^{43}$Ca hyperfine splitting*

The nuclear spin of $I = 7/2$ for $^{43}$Ca leads to three hyperfine levels of the $^1P_1$-state with total spins $F = 5/2, 7/2$ and $9/2$, respectively. The hyperfine structure (HFS) constants and isotope shift of $^{43}$Ca are determined by fitting

| $M_{\mathrm{SMS}}$ [GHz amu] | $F$ [MHz/fm$^2$] |
|---|---|
| $243 \pm 3 \pm 9$ | $-179 \pm 39 \pm 2$ |

*Tab. 4.2:* The specific mass shift $M_{\mathrm{SMS}}$ and field shift $F$ coefficients for the $4s^2\ ^1S_0 \leftrightarrow 4s5p\ ^1P_1$ transitions of calcium derived from the linear fit presented in Fig. 4.11. The first stated uncertainty estimate is the one standard deviation obtained from the linear regression to the data of Fig. 4.11. The systematic error in the isotope-shifts due to the frequency scan calibration is included as the second uncertainty estimate. The NMS coefficient is $M_{\mathrm{NMS}} = 604.3$ GHz amu.

to the Casimir formula [60]

$$\begin{aligned}\Delta E_F =& \Delta\nu_{\mathrm{cg}} + \frac{A}{2}C \\ &+ \frac{B}{4}\frac{\frac{3}{2}C(C+1) - 2I(I+1)J(J+1)}{(2I-1)(2J-1)IJ},\end{aligned} \tag{4.7}$$

where $C = F(F+1) - I(I+1) - J(J+1)$, $\Delta\nu_{\mathrm{cg}}$ is the isotope-shift of the center of gravity of the HFS, and $A$ and $B$ are the magnetic dipole and electric quadrupole coupling constants, respectively. Several scans across the three hyperfine resonances were made to increase the level of confidence of the $A$ and $B$ constants. The HFS constants derived from these scans are summarized in Table 4.3, while the center of gravity for $^{43}$Ca has been given in Table 4.1. The small value of the $B$ constant indicates that the magnetic dipole coupling has the most prominent contribution to lifting the degeneracy of the $4s5p\ ^1P_1$ level for $^{43}$Ca. Compared with the work of [62], where the HFS constants for the $4s4p\ ^1P_1$-state in $^{43}$Ca have been measured to be $A = -15.54 \pm 0.03$ MHz and $B = -3.48 \pm 0.13$ MHz, the $4s5p\ ^1P_1$ state has an opposite sign for the $A$ constant and the $B$ constant is of the same order of magnitude or smaller.

| $A$[MHz] | $B$[MHz] |
|---|---|
| $39.8 \pm 0.8 \pm 0.4$ | $-0.3 \pm 3 \pm 0.03$ |

*Tab. 4.3:* HFS constants for the $4s5p\ ^1P_1$ state in $^{43}$Ca. The first stated uncertainties originate from statistical errors in determining the resonance positions, while the second account for the systematic errors due to frequency calibration uncertainty.

## 4.6 Isotope selectivity

In order to quantify the isotope selectivity of the photo-ionization scheme we define a selectivity parameter

$$\eta_A = \frac{I_A(\nu_A)}{\sum_{A' \neq A} I_{A'}(\nu_A)}, \tag{4.8}$$

for the isotope with atomic mass $A$, where the $I_A(\nu)$ and $\nu_A$ are the resonance profile and the resonance frequency of the isotope with atomic mass $A$, respectively. In the special case of $^{43}$Ca the isotope selectivity is evaluated for the three hyperfine resonances individually, i.e., the $^{43}$Ca selectivity is described by three individual hyperfine resonance profiles $I_{43(F=5/2)}$, $I_{43(F=7/2)}$, and $I_{43(F=9/2)}$. As evident from Eq. (4.8) the selectivity parameter $\eta_A$ is just the ratio of the peak photo-ionization rate of the isotope, $A$, to the background photo-ionization rate of the other isotopes at the resonance frequency $\nu_A$. The parameter $\eta_A$ thus indicates the isotope purity of an ion crystal produced when we tune the photo-ionization laser to a given isotope resonance assuming that we can neglect near resonant electron transfer processes during the production of the ion crystal. The selectivity parameter is interesting from an experimental point of view, because it tells us which ions are favorable to load if we need big ion crystals consisting primarily of another calcium isotope than $^{40}$Ca.

The resonance profile functions, $I_A(\nu)$ are computed using Voigt profiles with identical FWHM widths. For this purpose we use the widths that were found by fitting the $^{40}$Ca resonance (see Sec. 4.4.2), i.e., a Lorentzian width of $w_{\mathrm{L}} = 7.3$ MHz and a Gaussian width of $w_{\mathrm{G}} = 47.8$ MHz. The resonance frequencies used for the different isotopes are the values presented in Table 4.1, while tabulated values of the natural abundances (see Table A.1) of the different calcium isotopes have been used to find the relative amplitudes of the different isotopes. In the special case of $^{43}$Ca, which has a hyperfine structure, we use the expected 3:4:5 ratio between the three hyperfine components to describe their relative strength.

The calculated full Voigt profile fit of all the isotopes ($I_{40}(\nu) + I_{42}(\nu) + \ldots$) have been plotted in Fig. 4.12 together with the three scans that were presented in Fig. 4.9. From this plot it is clear that the model presented above describes the photo-ionization data to a very good approximation. There is only a small discrepancy between the measured data and the Voigt profile between the detunings 2300 MHz and 2700 MHz. This is presumably just a consequence of the fact that it was not possible to load big ion crystals when measuring the ion production rate in this interval and thus have a bigger error in the size determination of the crystals.

The selectivity parameter $\eta_A$ have been calculated from this model using Eq. (4.8) for all the naturally occurring calcium isotopes and is presented in Table 4.6. In the case of $^{43}$Ca we have evaluated the isotope selectivity at the three hyperfine resonances. From the isotope selectivity of $^{40}$Ca, $\eta_{40} \sim 10^6$, it

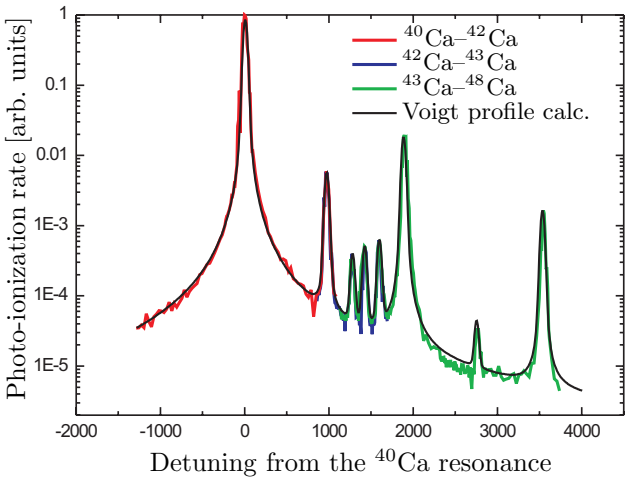


*Fig. 4.12:* Full Voigt profile calculation of the photo-ionization rate of all naturally occurring calcium isotopes compared to the normalized rate measurements introduced in Sec. 4.4.2.

is evident that it is indeed possible load a very clean $^{40}Ca^{+}$ crystal. Among the low abundant isotopes $^{44}$Ca is the one that have the highest selectivity of $\eta_{44} = 1.1 \times 10^3$, which is primarily coming from the bigger natural abundance of 2.086%. In comparison the $4s^2\ ^1S_0 \leftrightarrow 4s4p\ ^1P_1$ transition, which is used for ion trap loading by other groups [46, 51], have a maximum isotope selectivity of $\eta_{44} \sim 40$ as reported by [53]. This transition have a natural linewidth of $\sim 35.6$ MHz as well as an isotope shift that is about 2.3 times smaller than the isotope shift we have measured for the $4s^2\ ^1S_0 \leftrightarrow 4s5p\ ^1P_1$ transition (see Sec. 4.5). This illustrates that the advantage of the transition we have chosen for photo-ionization is the small natural linewidth together with a large isotope shift yielding an order of magnitude larger isotope selectivity. The drawback of the

| Isotope ($A$) | Selectivity($\eta_A$) |
|---|---|
| 40 | $\sim 10^6$ |
| 42 | 89 |
| 43(9/2) | 15 |
| 44 | $1.1 \times 10^3$ |
| 46 | 3.6 |
| 48 | $3.2 \times 10^2$ |

*Tab. 4.4:* Isotope selectivity derived from the measured isotope shifts, the Lorentz width, and the Doppler width of the $4s^2\ ^1S_0 \leftrightarrow 4s5p\ ^1P_1$-transition, as well as the natural abundance of the different isotopes found in Table A.1. The isotope selectivity of $^{43}$Ca is given for the hyperfine component $F = 9/2$ as this has the highest selectivity of the three hyperfine resonances.

transition we are using is that the oscillator strength of the $4s^2\ ^1S_0 \leftrightarrow 4s5p\ ^1P_1$ transition is about 3 orders of magnitude smaller than the oscillator strength of the $4s^2\ ^1S_0 \leftrightarrow 4s4p\ ^1P_1$ transition [52], which makes the efficiency of our scheme accordingly smaller.

## 4.7 Conclusion

We have demonstrated that the resonant photo-ionization of an atomic beam of calcium provides a method of isotope selective loading of an ion trap. The ionization rate measurements indicate that ions of all naturally occurring calcium isotopes can be produced. As the most prominent example the ionization spectrum revealed traces of the $^{46}$Ca isotope which has a very low abundance of only 0.004%. For the $^{44}$Ca isotope that has an abundance of 2.086% the isotope selectivity of $\eta_{44} = 1100$ is so good that production of ion crystals with a high content of this isotope is indeed feasible. Near resonant electron transfer between atoms in the atomic beam and trapped ion has been introduced as a method to control the ratio of $^{40}Ca^+$ and $^{44}Ca^+$ ions in bi-crystals, which is an essential ingredient in the quantum memory scheme.

The isotope shifts and the hyperfine splitting of the $4s^2\ ^1S_0 \leftrightarrow 4s5p\ ^1P_1$ transition was measured and from these data we deduced the field shift and specific mass shift coefficients as well as the hyperfine structure constants for $^{43}$Ca.

# 5. ELECTRON TRANSFER EXPERIMENTS

Trapped laser cooled ions offer an opportunity to study collisions between atoms in an effusive atomic beam and cold ions at velocities corresponding to thermal energies. In this chapter we will study the low-energy near resonant charge transfer between $^{44}Ca^+$ and $^{40}Ca$. We demonstrate a technique to measure the charge transfer rate at different ion Coulomb crystal positions relative to the Paul trap center axis. By estimating the atomic flux from the calcium oven we can use this rate measurement to estimate the charge transfer cross section at thermal energies. The measured cross section is compared to an estimate of the cross section found by extrapolation of some higher energy charge transfer data. The symmetric resonant charge transfer process $Ca+Ca^+ \rightarrow Ca+Ca^+$ has been studied experimentally at higher energies $\sim$ 8–500 eV by Panev *et al.* [67] and Rutherford *et al.* [68], and theoretically by Liu and Olson [69]. But at energies corresponding to thermal energies there are to our knowledge no experimental work on this transfer process.

## *5.1 Electron transfer cross section*

We have studied the asymmetric near resonant charge transfer process

$$^{40}Ca + {}^{44}Ca^+ \rightarrow {}^{40}Ca^+ + {}^{44}Ca + \Delta E, \tag{5.1}$$

where $\Delta E \sim 10^{-5}$ eV as mentioned in Sec. 4.3.3. This means $\Delta E$ is much smaller than the typical thermal collision energy in the process described in Eq. (5.1), and thus we will regard this process as a symmetric charge transfer process with respect to the electronic wave function.

There are two mechanisms responsible for the behavior of the charge transfer cross section as function of the relative velocity of the ion and the atom. In the following we will discuss the physics behind these mechanisms and try to give an estimate of the charge transfer cross section at thermal energies from this discussion.

The first mechanism is relevant when the relative speed between the ion and the atom is so low that their individual velocities are changed significantly by the attractive dipole potential that exists between an ion and a neutral atom due to the induced dipole moment of the atom. At large internuclear distances the potential energy in this interaction is described by the dipole potential

$$\phi(R) = -\frac{1}{4\pi\epsilon_0}\frac{e^2\alpha}{2R^4}, \tag{5.2}$$

where $R$ is the internuclear distance and $\alpha$ is the polarizability of the atom. The orbits in such a potential have been calculated by Langevin in 1905 (see Ref. [70]). Such orbits can be characterized by two parameters: the initial relative velocity $v$ and the impact parameter $b$, which is the distance at which the initial path of the atom passes the ion. For these orbits it is possible to define a critical parameter

$$b_0 = \left(\frac{e^2\alpha}{\pi\epsilon_0\mu v^2}\right)^{1/4} \tag{5.3}$$

for which the orbits with $b < b_0$ will go through the center, while the orbits with $b \geq b_0$ never come closer than $b_0/\sqrt{2}$ to the center. In other words at a low velocity, $v$, the orbits divide in two classes as a function of the impact parameter $b$. Those which only result in a grazing incidence and those which result in an atom ion impact. Neglecting the charge transfer in the grazing incidence collisions and assuming that the charge exchange probability for a symmetric process is $1/2$, when we have an ion atom impact the charge transfer cross section becomes $\sigma = \frac{1}{2}\pi b_0^2$. Inserting Eq. (5.3) into this expression we get

$$\sigma(v) = \frac{\pi}{v}\sqrt{\frac{e^2\alpha}{4\pi\epsilon_0\mu}}, \tag{5.4}$$

which I will refer to as the Langevin approximation. Inserting $\alpha = 154a_0^3$ which is the polarizability of calcium [71] and the reduced mass $\mu$ of $^{40}$Ca and $^{44}$Ca we get $\sigma \simeq 1.2 \times 10^{-11}/v$ cm$^2$, where $v$ is in m/s.

At higher impact velocity the Langevin approximation breaks down, because here the atomic motion is almost unaffected by the dipole potential. But as long as the velocities are well below $10^6$ m/s the charge transfer cross section can be calculated using the Born Oppenheimer separation of electronic and atomic motions (see, for example, Ref. [72]) and assuming that the atomic motion is rectilinear. In the case of symmetric charge transfer it can be shown that the cross section behaves as $\sigma(v) = [A + B\ln(v)]^2$, where $A$ and $B$ are coefficients [73]. Liu and Olson [69] have calculated the charge transfer cross section in the case of collisions between $Ca^+$ and Ca for collision energies 10–10000 eV, while Panev *et al.* [67] (8–500 eV) and Rutherford *et al.* [68] have investigated this experimentally.

The charge transfer cross section for $^{40}$Ca–$^{44}$Ca$^+$ collisions is plotted as function of the impact velocity in Fig. 5.1. From this plot we conclude that the main contribution to the cross section at the thermal velocities comes from the extrapolated $\sigma(v) = [A + B\ln(v)]^2$ behavior and that we should expect a cross section $\sigma \sim 5 \times 10^{-14}$ cm$^2$ at thermal collision energies.

## 5.2 Characteristics of the effusive beam

To make a quantitative measurement of the charge transfer rate that can be used to determine the charge transfer cross section we have to consider the

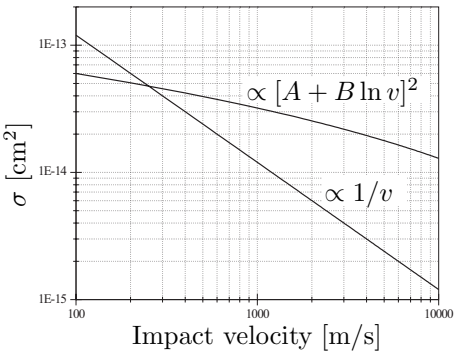


*Fig. 5.1:* Charge transfer cross section as function of the impact velocity. Graph (a) is the described by the formula $\sigma \simeq 1.2 \times 10^{-11}/v$ cm$^2$ and graph (b) is of the form $\sigma(v) = [A + B \ln v]^2$, where the $A$ and $B$ coefficients have been calculated by Ref. [69].

characteristics of the effusive atomic beam of calcium. In this section we will describe the spatial atomic flux distribution in the beam and make a quantitative statement about the beam intensity based on gas kinetics. Most of the discussion in this section is based on textbook of N. F. Ramsey on molecular beams [74].

A schematic of the oven setup is shown in Fig. 5.2 (a) (see also Sec. 3.2 and Fig. 4.2). The skimmer width is denoted $w$ and the line marked 'Detection' denotes the center of the linear Paul trap, where the atomic flux is going to be detected as a function of the position. The beam of calcium effuses through a 4–5 mm long canal that have a cross section of $A = 0.785$ mm$^2$. Before the atomic beam reach the Paul trap it is collimated with a skimmer that has a height of a few 100 $\mu$m and a width of 2.4 mm. The distance between the oven and the skimmer is 72.6 mm and the Paul trap is located 44.3 mm away from the skimmer.

It can be shown that the flux of atoms from an effusive source can be expressed as [74]

$$\phi_{\mathrm{a}} = 1.118 \times 10^{22} \frac{pA}{l^2\sqrt{MT}} \text{ atoms}/(\text{cm}^2 \cdot \text{s}), \tag{5.5}$$

where $p$ is the oven source pressure in mm Hg, $l$ is the length to the oven source, $M$ is the atomic mass, and $T$ is in Kelvin. This result is usually derived for an oven with a thin walled orifice, but it also applies in our case where the atoms effuse through a long circular canal. The condition for this to be true is that the mean free collision path inside the oven source $\lambda_{\mathrm{M}}$ is sufficiently long for collisions inside the canal to be negligible. The mean free collision path can be calculated from the expression $\lambda_{\mathrm{M}} = 1/n\sigma\sqrt{2}$, where $n$ is the density of atoms and $\sigma$ the collision cross section. The collision cross section $\sigma \sim 600 \times 10^{-16}$cm$^2$ is used as an upper limit for the collision cross section of calcium [74]. At the working temperature of $T \sim 700$°K the density of atoms is $n \sim 10^{12}$ m$^{-3}$, which

is found from Eq. (A.1) in appendix A. From these values a mean free path length of $\lambda_M \gtrsim 10$ cm is found, which is much longer than the canal length and thus Eq. (5.5) also applies to the long canal length.

The reader may find it a bit disturbing that the flux given by Eq. (5.5) is the same for the long canal as the thin walled orifice. After all the total flux and the angular distribution out of an oven is not the same in the two situations due to the atoms, that strike the wall of the canal, have a smaller probability of escaping the oven and if they do so they will emerge at a different angle. The reason why the flux in forward direction of the oven is unaltered is that the atoms striking the wall of the canal will emerge again distributed according the Knudsen law. This says that if $N$ atoms strike a wall for which there is no specular reflection or diffraction then the number $dN$ that emerge from the surface within the solid angle $d\Omega$ making an angle $\theta$ with the normal to the surface is $dN = (1/\pi)N\cos\theta d\Omega$. For the canal wall $\theta = \pi/2$ in the forward direction of the oven. This means $dN = 0$ is this direction, i.e., there are no attenuation of the atomic flux in the forward direction and Eq. (5.5) is valid in the case of a long canal.

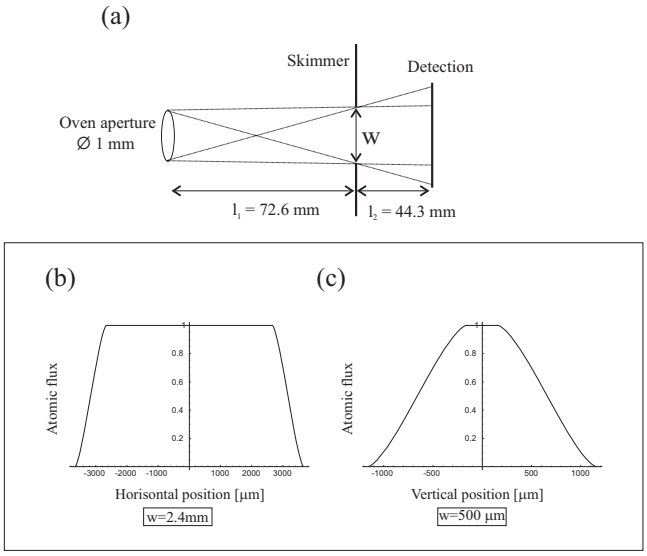


*Fig. 5.2:* The atomic beam flux as a function of the position transverse to the atomic beam direction. (a) illustrates basic geometric principles of how oven source and skimmer widths relate to the atomic beam shape. The two graphs shows the expected atomic beam shape in the horizontal direction (b) ($w = 2.4$ mm) and the vertical direction (c) ($w \sim 500$ $\mu$m). The atomic flux is given in units of the flux calculated from Eq. (5.5).

The atomic beam shape at the location of the ion crystal depends on the size of the oven aperture, the horizontal and vertical widths of the rectangular skimmer hole($w$), and their relative positions as illustrated in Fig. 5.2 (a). The

beam shape for a given geometry is calculated evaluating the area of the oven orifice which is not obscured by the skimmer at a given point of the line marked by 'detection' in Fig. 5.2 (a). This calculation has been done assuming a circular oven aperture with diameter ∅1 mm, while the skimmer widths are $w = 2.4$ mm horizontally (Fig. 5.2 (b)) and $w = 500$ $\mu$m vertically (Fig. 5.2 (c)), which resembles the real oven setup. When the oven orifice diameter is sufficiently small there are locations on the 'detection' line, where the oven orifice is completely unobscured by the skimmer. In these locations the atomic flux is just the same as would be observed in the absence of the skimmer, i.e., the flux is constant and given by Eq. (5.5). In Fig. 5.2 (b) and (c) this is just given by the region of constant flux. The region where the oven orifice is partly obscured we refer to as the *penumbra* region. In Fig. 5.2 it is apparent that the expected beam shape vertically is dominated by the penumbra region, as opposed to the horizontal direction where the appreciable skimmer width gives constant flux over a large range.

The vertical beam shape shown in Fig. 5.2 (c) illustrates that it is essential that we measure the charge transfer rate at the position at maximum flux, because here the flux is known and given by Eq. (5.5). How information about the beam shape in the vertical direction is obtained experimentally is the theme of Sec. 5.3.

## 5.3 Vertical beam shape

We want to measure the rate of charge transfer between the $^{40}$Ca atoms in the effusive atomic beam and the $^{44}Ca^{+}$ ions trapped in the linear Paul trap and then from an estimate of the flux of $^{40}$Ca atoms this measurement is converted to an estimate of the charge transfer cross section. The basics of the setup used in these experiments were described in Sec. 3.2.

In order to be sure that the charge transfer rate is measured at the position of maximum atomic beam flux, i.e., at the position where the atomic beam flux is given by Eq. (5.5), we need to measure the vertical profile of the flux. The experimental method used for mapping the atomic beam shape is described in this section.

The basic idea is to use a small $^{40}Ca^{+}$–$^{44}Ca^{+}$ bi-crystal to probe the electron transfer rate between $^{40}$Ca atoms in the atomic beam and $^{44}Ca^{+}$ ions in the crystal, when the crystal is displaced vertically from the trap center. The electron transfer rate is proportional with the atomic beam flux at the position of the ion crystal and we can therefore map out the vertical atomic beam flux profile.

The displacement of the crystal away from the trap center is done by applying offset DC voltages to the Paul trap electrodes. In Fig. 5.3 the 12 electrodes are numbered from 1 to 12. In order to make a displacement of the ions we choose to apply an offset DC voltage, $-V$, to the 1–2–3 electrodes, which translates the ions in the $x'y'$ plane in the $(\hat{x}' + \hat{y}')/\sqrt{2}$ direction. To compensate the horizontal displacement of the ions we also apply the offset voltage $V$ to the 4–

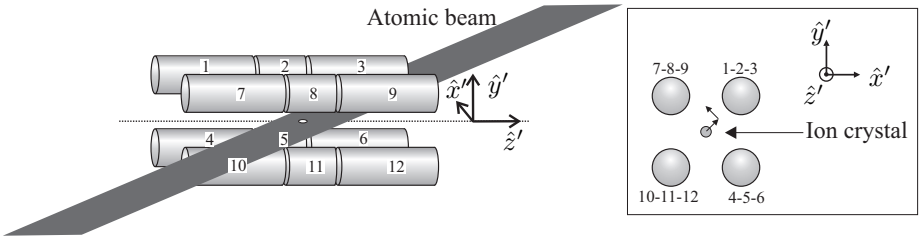


*Fig. 5.3:* Overview of the Paul trap electrode numbering and a sketch of the crystal displacement when an offset voltage is applied to the electrodes 1–2–3 and subsequently to 4–5–6.

5–6 electrodes, which translates the ions in the $(-\hat{x}'+\hat{y}')/\sqrt{2}$ direction. Because the CCD-camera is placed vertically above the trap (see Sec. 3.3), it is not possible to directly measure the vertical position of the ions relative to the trap center from the images of the crystal. In order to circumvent this problem the horizontal displacement of the ions relative to the trap center is calibrated with respect to the applied offset voltage of electrodes 1–2–3 and 4–5–6, when the applied voltage has the same sign, i.e., horizontal $\hat{x}'$ displacement only. The calibration which is done with a small Coulomb crystal containing $\sim 300$ $^{40}Ca^{+}$ ions, and the applied rf-voltage is $U_{\mathrm{rf}} \sim 200$ Volt. The calibration result is shown in Fig. 5.4 and from this plot we can conclude that there is a nice linear dependence between the displacement of the crystal and the applied offset voltages.

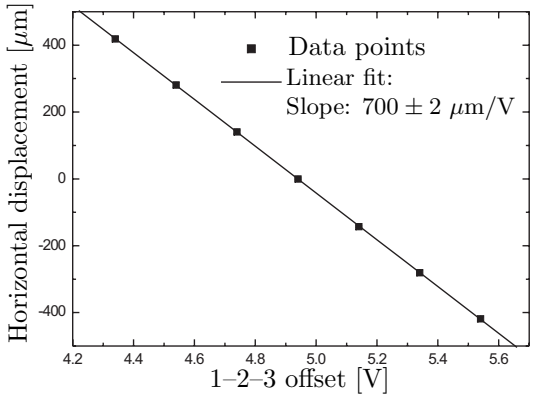


*Fig. 5.4:* Calibration of the horizontal displacement of $^{40}Ca^{+}$ ions from the trap center versus the offset voltage on electrodes 1–2–3 and 4–5–6.

The beam profile measurement, which is seen in Fig. 5.6, was taken by measuring the charge transfer rate using small $^{40}Ca^{+}$–$^{44}Ca^{+}$ bi-crystals containing $\sim 1000$ ions. The thermometer read off of the oven temperature during

the beam measurement was $533 \pm 2°$C. In the following the method used for measuring the charge transfer rate for different vertical positions of the crystal is described. Initially a small bi-crystal of $^{40}Ca^{+}$–$^{44}Ca^{+}$ consisting mainly of $^{44}Ca^{+}$ ions is loaded. Only the $^{40}Ca^{+}$ ions are directly laser cooled, so we can only count the number of $^{40}Ca^{+}$ ions situated in the core of the crystal from pictures like in Fig. 5.5(a) recorded by the CCD-camera. After the $^{40}Ca^{+}$ ion core has been imaged, the crystal is moved vertically from the trap center to the position where we want to measure the charge transfer, where it is exposed to the atomic beam for about 10 s. The exposure time is controlled manually by un-blocking and blocking the oven beam using the oven shutter (see Sec. 3.2), while the exact exposure time is measured using a stop watch. Subsequently the crystal is moved back to the trap center, where it is in focus of the camera, such that the increase in the number of $^{40}Ca^{+}$ ions can be determined (Fig. 5.5(b)). In order to measure the decay rate of the $^{44}Ca^{+}$ ions, we need to deduce the number of $^{44}Ca^{+}$ ions instead of the number of $^{40}Ca^{+}$ ions. To accomplish this only the total number of ions in the crystal needs to be known, which is found by completing the measurement by converting the remaining $^{44}Ca^{+}$ ions into $^{40}Ca^{+}$ ions using charge transfer (Fig. 5.5(c)).

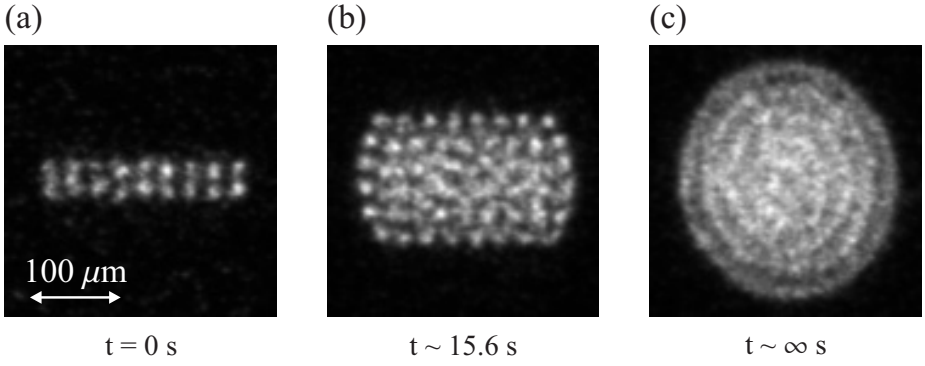


*Fig. 5.5:* Example of a $^{40}Ca^{+}$–$^{44}Ca^{+}$ bi-crystal used for the beam shape measurements. The crystal shape during the charge transfer measurement is prolate. See text for further details.

During the $\sim 10$ s charge transfer measurement the crystal has a horizontally elongated shape obtained by lowering the end-cap potential of the linear Paul trap. This is done to ensure that the vertical extend of the crystal is below 100 $\mu$m, which consequently is the maximum size of our atomic flux detector. When the number of ions needs to be counted the end-cap potentials are increased to shape the crystal like a sphere as shown in Fig. 5.5 for a precise determination of the number of $^{40}Ca^{+}$ ions present in the crystal.

The result of the electron transfer measurements is shown in Fig. 5.6 as a function of the vertical crystal position with respect to the Paul trap center. Each data point presented in the graph is the average of 3 measurements and the error bars represents two standard deviations of the measurements. Inspired by

the beam shape graphs presented in Fig. 5.2 a free-hand drawing of a trapezoid has been added to the plot to guide the eye. Even though the measured beam shape deviates somewhat from what we would expect from the simulation shown in Fig. 5.2(c) it still features the expected characteristics, namely a flat constant flux region with a rate of $\sim 0.032$/s and two penumbra regions. It is difficult to say why the data in Fig. 5.6 differs from the simulation in Fig. 5.2(c). The truth about the beam shape obviously depends on the exact geometry of the oven setup. An opening of the vacuum chamber could provide us with the information needed to make a correct interpretation of the data shown in Fig. 5.6.

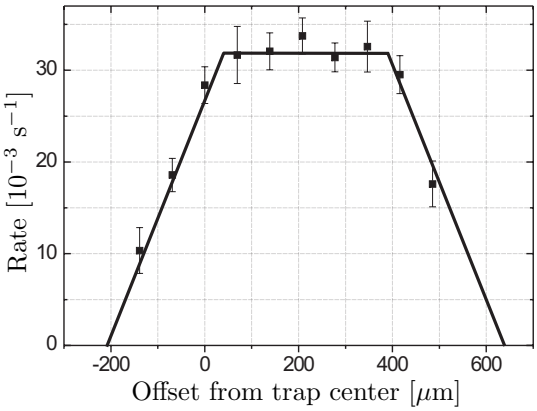


*Fig. 5.6:* Vertical beam profile measurement.

## *5.4 Oven temperature*

Establishing the correct oven temperature is essential for estimating the atomic flux of calcium given by Eq. (5.5). During experiments the oven temperature is monitored with a thermosensor coupled to the oven graphite (see Sec. 3.2), but due to temperature gradients in the oven graphite the temperature read off the thermosensor is not necessarily the same as the temperature of the calcium vapor residing inside the oven chamber. To find the correct temperature of the calcium vapor we have to measure the velocity distribution of the calcium atoms in the atomic beam. For simplicity the same oven temperature has been chosen for all the experiments in present chapter, i.e., the oven temperature measured by the thermosensor is $T = 533°$C. In this section we will establish what the corresponding actual temperature of the calcium vapor is.

The normalized velocity distribution of the number density of calcium atoms in an effusive atomic beam depends only on the temperature $T$ and the mass $M$ of the atoms [75]

$$f_v(v)dv = \frac{4v^2}{\sqrt{\pi}\alpha_T^3} e^{-v^2/\alpha_T^2} dv, \tag{5.6}$$

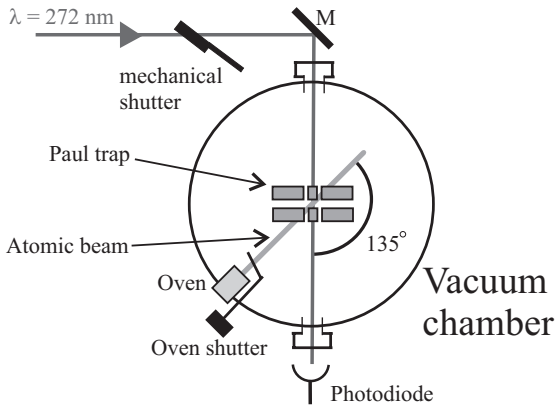


*Fig. 5.7:* Experimental setup for the velocity distribution measurement. The 397 nm and 866 nm cooling lasers have not been included in this figure, but the cooling laser setup is the same as in Fig. 4.2

where $\alpha_T = \sqrt{2k_{\mathrm{B}}T/M}$ and $v$ is the atomic velocity. We can therefore find temperature of the calcium vapor from a measurement of the velocity distribution of the atomic beam. The experimental setup for this measurement is shown in Fig. 5.7. The experimental method for measuring the velocity distribution is similar to the method we used in the photo-ionization rate measurements described in Sec. 4.4 with the modification that the 272 nm photo-ionization laser beam direction has a $135° \pm 0.5°$ angle with respect to the atomic beam direction. After a simple geometric consideration it is seen that the photo-ionization transition frequency, $\nu$, is shifted by an amount $\Delta = v\nu/\sqrt{2}c$ for atoms belonging to the velocity class $v$. Using this expression in Eq. (5.6) we find that the normalized photo-ionization spectrum for photo-ionization under this angle is

$$f_\Delta(\Delta)d\Delta = \frac{4\Delta^2}{\sqrt{\pi}\beta_T^3}e^{-\Delta^2/\beta_T^2}d\Delta, \tag{5.7}$$

where $\beta_T = \alpha_T\nu/\sqrt{2}c$.

Figure 5.8 shows the photo-ionization rate as function of the photo-ionization laser frequency when the thermosensor temperature is 533°C. The full curve is a weighted fit of the data points to Eq. (5.7). For each curve the temperature found from the fit is noted in the graph. The uncertainties stated are the statistical fit uncertainty and a systematic uncertainty. There are two contributions to the systematic uncertainty, namely the calibration uncertainty of the photo-ionization laser (2.2%) and the 0.5° uncertainty in the 135° angle between the atomic beam and the photo-ionization laser beam (1.7%). The total systematic uncertainty is 2.8%, and this naturally sets the lower bound on how precise the temperature can be determined. The velocity profile was measured 4 times and the corresponding temperatures was found from a fits of Eq. (5.7) to the profiles as shown in Fig. 5.8. The weighted average of the 4 temperatures shown

in Fig. 5.8 is $T = 691 \pm 8 \pm 19$°K, which we will regard as the actual oven temperature when the temperature sensor measures $T = 533$°C.

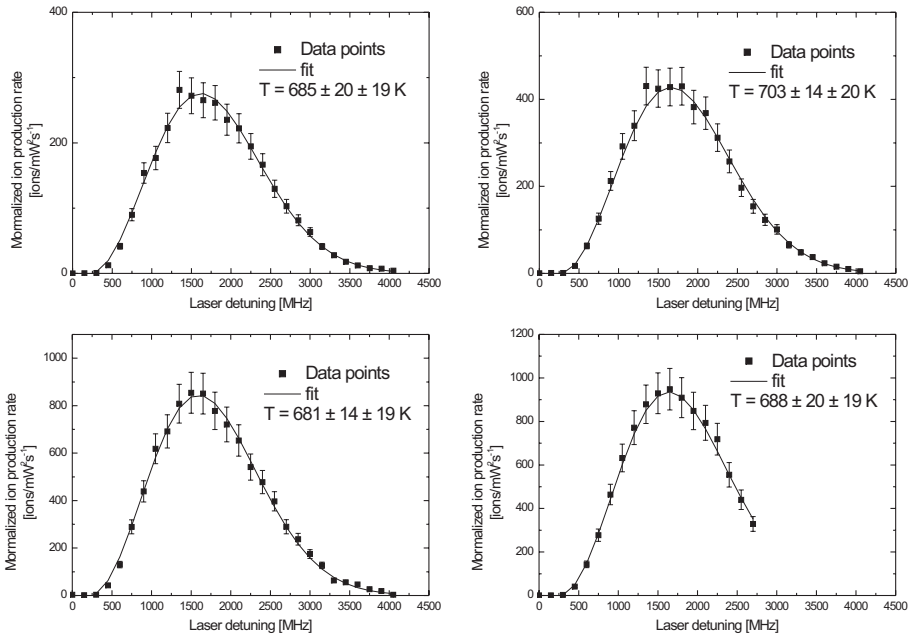


*Fig. 5.8:* Normalized ionization rates as function of the ionization laser detuning.

Inserting this temperature into Eq. (5.5) we find that the atomic flux of calcium at the Paul trap position is

$$\phi_{\mathrm{a}} = 9 \times 10^{10} \pm \left\{ \begin{array}{l} +140\% \\ -60\% \end{array} \right. \text{ atoms/(cm}^2 \cdot \text{ s)}, \tag{5.8}$$

assuming that no collimating slit or other obstruction intercepts with the beam on its way the trap. This flux result is used in Sec. 5.5 to find the charge transfer cross section between $^{44}$Ca$^+$ ions and $^{40}$Ca atoms.

## 5.5 Charge transfer cross section

After having determined the approximate vertical profile of the atomic beam in Sec. 5.3 it still remains to make a precise measurement of the electron transfer rate at position where the atomic beam profile has its maximum. The charge transfer rate is measured at the vertical position $\sim 150$ $\mu$m from the center-axis (see Fig. 5.6) . The charge transfer rate was measured using only one $^{40}$Ca$^+$–$^{44}$Ca$^+$ bi-crystal with a total of $\sim 580$ ions and using the almost same method as described in Sec. 5.3. The only difference is that we make several intermediate measurements of the $^{40}$Ca$^+$ fraction of the crystal before the crystal has become

almost a pure $^{40}Ca^+$ crystal. The result is shown in Fig. 5.9(a), where the number of $^{44}Ca^+$ ions in the crystal is plotted as a function of the time that the crystal has been exposed to the atomic beam. As expected the number of $^{44}Ca^+$ is exponentially decaying as a function of time, and a weighted fit of the data points in Fig. 5.9(a) reveals a $^{44}Ca^+$ decay rate of $\gamma = 0.032 \pm 0.002$ s$^{-1}$. It is reassuring to see that this decay rate agrees with the decay rates found in the beam profile measurement seen in Fig. 5.6.

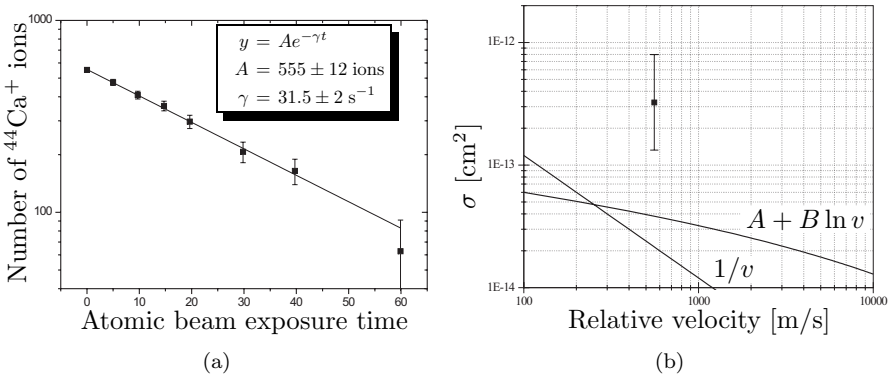


*Fig. 5.9:* (a) Measurement of the charge transfer rate at the vertical position $\sim 150$ $\mu$m from the trap axis (see Fig. 5.6). (b) Comparison between theory (Sec. 5.1) and experimentally determined cross section. The experimental result has been plotted at 600 m/s which corresponds to the average atomic velocity in the beam.

Using the atomic flux, which is found in Eq. (5.8), and the charge transfer rate measurement, we find that the charge transfer cross section is

$$\sigma = 3.5 \times 10^{-13} \pm \begin{cases} +140\% \\ -60\% \end{cases} \text{ cm}^2. \tag{5.9}$$

A comparison between the result reported in Eq. (5.9) and the theory presented in Sec. 5.1 is plotted in Fig. 5.9(b). It is seen that the theoretically predicted cross section is an order of magnitude smaller than the measured cross section. Experimentally there are two factors that can contribute to this discrepancy, namely erroneous temperature measurement of the atomic beam, and the 'unknown' oven collimator geometry. The temperature is indeed critical for the cross section measurement, which is seen by considering that the large error bars in Fig. 5.9(b) solely comes from the temperature uncertainty, and it is hence not possible to completely rule out the temperature measurement as a significant error source. While it remains unsaid if the temperature measurement is erroneous, it more interesting to consider the oven geometry. At present the only knowledge we have about the oven collimator setup is from technical drawings. Many differences are found when comparing the theoretical atomic beam shape (Fig. 5.2) with the measured beam shape (Fig. 5.6), which indicates

that oven setup may be different from what we expect. The beam collimator can only reduce the maximum atomic flux measured at the Paul trap, which in turn would increase the cross section calculated from this flux and our result would be closer to the theory. We can obtain knowledge about the real oven collimator setup once the vacuum chamber (see Sec. 3.2) is opened again, but there are no plans of doing so in the nearest future.

Looking at the beam scan result in Fig. 5.6 and the measurement of the charge transfer rate in Fig. 5.9(a) it is clear that the thermal charge transfer rate can be measured to a high precision using ion Coulomb crystals. The Achilles' heel of the cross section measurement is the atomic flux estimate, so it would indeed be satisfactory if we could improve this estimate. The ideal way to determine the atomic flux would be to use absorption spectroscopy on the $4s^2\ {}^1S_0 \leftrightarrow 4s4p\ {}^1P_1$ transition in neutral calcium, which has the transition wavelength $\lambda = 422.7$ nm. Currently a laser source at this wavelength is not present in our laboratory.

# 6. CRYSTAL STRUCTURE STUDIES

In this chapter we report on the structural properties of single component as well as two component ion Coulomb crystals in a linear Paul trap. The main emphasis here will be on the ordering of the ions in different lattice structures and shell structures. Lattice structures as face-centered cubic (fcc) and body-centered cubic (bcc) are observed. Concerning the single component Coulomb crystals we will concentrate on small crystal sizes in the regime $\sim 1000$ ions, and for the bi-crystals the observed fcc structure in the $^{40}Ca^{+}$ ion core is directly compared to Molecular Dynamics (MD) simulations of bi-crystals.

## *6.1 One component crystal structures*

The Wigner crystallization of electrons in metals was suggested in 1934 [24] and since then there have been extensive experimental and theoretical studies of various systems exhibiting these crystalline states. Experimentally laser cooled ions confined in an electromagnetic field are excellent targets for studying the structure of Coulomb crystals containing a single component. This has been done both in Paul traps [76–80] and in Penning traps [81–84]. In Nature these ion Coulomb crystals are believed to be present in ultra dense stellar objects as in the interior of cooling white dwarf stars [27].

In smaller ion Coulomb crystals, where surface effects dominate, the crystal structures are determined by the boundary condition set by the trapping potentials. This is not the case for larger ion Coulomb crystals with more than 10,000 particles where the predicted ground state structure of the crystal has both theoretically [85, 86] and experimentally [83, 84] proven to be a body-centered cubic structure . In contrast the fcc structure is predicted for clusters where the particles interact via short range potentials as for instance the Lennard-Jones potential [87]. In the case of mesoscopic systems of up to 10,000 charged particles confined in a spherically symmetric harmonic potential the theoretical prediction is that in the ground state of the system the ions will order in a spherical concentric shell structure, where the shells are filled according to certain "magic numbers" of particles [88]. On the other hand as the number of particles in the Coulomb crystal is increased the difference in binding energy of the various spatial configurations becomes smaller due to the decreasing influence of surface effects[1]. Furthermore the number of isomeric configurations is

[1] This has been confirmed by MD simulations performed by Thierry Matthey and Michael Drewsen (to appear in Ref. [VI]).

generally expected to grow exponentially with the number of particles [89]. This means that at a finite temperature the crystal structure might undergo transitions between the various configurations when the ion number is above a certain threshold. This phenomenon has not yet been investigated for spherically symmetric ion Coulomb crystals containing about 1000 ions. In the following we report on direct observations of long-range order in ion Coulomb crystals containing down to 1000 ions.

### 6.1.1 Experimental method

The experiments on $^{40}Ca^{+}$ single component crystals were performed in the linear Paul trap described in Sec. 3.1. The standard laser systems for laser cooling and ion production described in Chap. 3 were used. The camera system has a resolution of $0.71 \pm 0.01$ $\mu$m/pixel. The depth of focus of the imaging system is at least a few times the inter-ion spacing, so when a lattice structure occurs in the two-dimensional projection images of the crystal it must originate from a 3D long-range ordered lattice structure in the crystal oriented such that the lattice is translational invariant in the direction towards the camera. In the camera focus the ion micromotion is approximately directed along the direction of view of the camera system. Further away from the camera focus the micromotion is perpendicular to the direction of view of the camera. This is illustrated in Fig. 6.1.

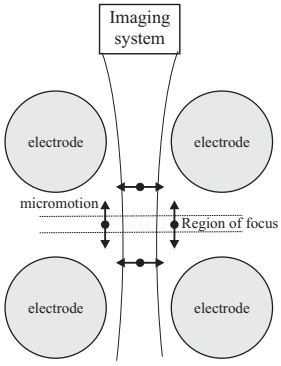


*Fig. 6.1:* Illustration of the direction of the micromotion of the ions relative to the focus of the imaging system. The arrows indicate the micromotion of the ions.

### 6.1.2 Observed structures in large crystals

Two projection images of a big crystal containing $\sim 13,000$ $^{40}Ca^{+}$ ions are seen in Fig. 6.2. The Paul trap is operated at an rf-voltage of $U_{\mathrm{rf}} \sim 400$ V corresponding to an ion density of $n = 2.2 \times 10^{8}$ cm$^{-3}$. The exposure time of the camera is 100 ms. In Fig. 6.2(a) a hexagonal structure is visible in the projection of the crystal. The simple cubic (sc), face-centered cubic (fcc),

body-centered cubic (bcc) structures all exhibit such a hexagonal structure when viewed along one of the cube diagonals (e.g., the [111] direction), but for a given length $d$ of the sides of the equilateral triangles in the hexagonal structure the density of ions $n$ is different for the three different cubic structures such that $n_{\rm bcc} = 2n_{\rm sc} = 4n_{\rm fcc}$. Assuming that the observed crystal structure in Fig. 6.2(a) is a bcc structure projected in the [111]-direction the ion density deduced from the length $d = 17.2 \pm 0.2$ $\mu$m is $n_{\rm bcc} \sim 2.1 \pm 0.1 \times 10^8$ cm$^{-3}$. In view of the fact that $n_{\rm fcc} = \frac{1}{4} n_{\rm bcc}$ and $n_{\rm sc} = \frac{1}{2} n_{\rm bcc}$ it is safe to conclude that the hexagonal structure in Fig. 6.2(a) presumably arise from a bcc structure and not a fcc structure or a sc structure.

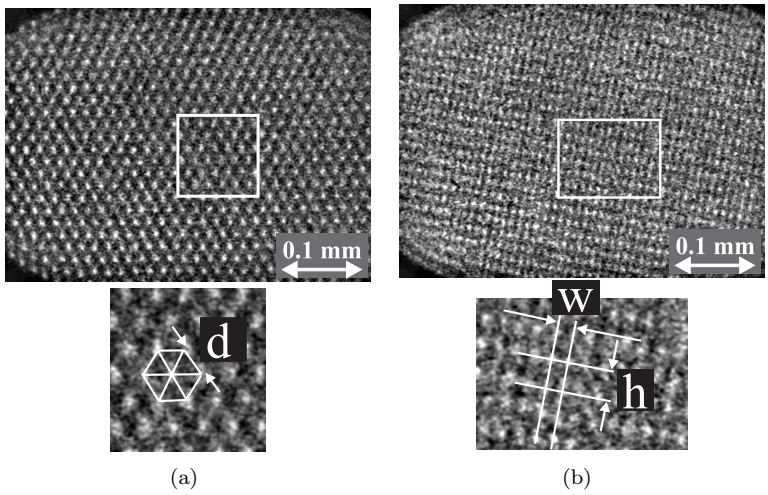


*Fig. 6.2:* $^{40}Ca^+$ ion crystal showing both bcc structure (a) and fcc structure (b). The inserts below the pictures indicate the projected structure of the crystals as well as define the lengths $d$, $w$, and $h$ used in the text.

In Fig. 6.2(b) a rectangular structure is visible in the projection of the crystal. The sides of the rectangle are $h = 15.2 \pm 0.5$ $\mu$m and $w = 9.71 \pm 0.2$ $\mu$m revealing that the ratio of the sides is $h/w = 1.55 \pm 0.06$. A structure that exhibits such a rectangular crystal projection is the fcc structure when viewed along the [211] direction and the ratio of the sides of the rectangle is $h/w = \sqrt{8/3} \approx 1.63$. Although there is not perfect agreement this could indicate that the projected structure in Fig. 6.2(b) is an fcc structure viewed along the [211] direction. This is supported by the ion density deduced from the lengths of the sides of the projected rectangle if it is assumed that the crystal structure is fcc. For the longest side of the rectangle ($h$) the deduced ion density is $n_{{\rm fcc},h} = 2.2 \pm 0.2 \times 10^8$ cm$^{-3}$ and for the shortest side the deduced density is $n_{{\rm fcc},w} = 1.9 \pm 0.1 \times 10^8$ cm$^{-3}$. It is seen that $n_{{\rm fcc},h}$ agrees with the expected ion density, while there is a 10% difference between the expected ion density and $n_{{\rm fcc},w}$. The origin to the discrepancy between the observed projected structure and a fcc lattice [211] projection is at present unknown, but one explanation could be that the

observed structure is distorted by the micromotion of the ions in the crystal. In conclusion we have observed both bcc structures and fcc like structures in large ion crystals with ion numbers exceeding $\sim 10,000$.

### 6.1.3 Observed structures in small ion clusters

MD simulations [85, 86] previously indicated that bcc structures are not present in ion clusters which have less than $\sim 10,000$ ions. We here report on bcc structures in spherically shaped one component ion Coulomb crystals containing down to $\sim 1000$ ions.

Figure 6.3 shows a series of projection images of nearly spherically symmetric ion Coulomb crystals with ion numbers in the range 300–2700 ions. The Paul trap is operated at an rf-voltage of $U_{\rm rf} \sim 400$ V which corresponds to an ion density of $n = 2.2 \times 10^8$ cm$^{-3}$. The exposure time of the camera is 100 ms. In Fig. 6.3 (a), (c), (e), and (g) the fluorescence from the crystallized ions exhibits clear ring structures indicating that the ions are localized in concentric shells as predicted by Hasse *et al.* [88]. In Fig. 6.3 (b), (d), (f), and (h) lattice structures are present, at least locally, in the projection images, which indicates that the crystals must have undergone a transition to lattice like cluster structures. In the two largest crystals, hexagonal structures are present and clearly seen in the projection images (Fig. 6.3 (f) & (h)) indicating that long-range ordering is present throughout the entire crystal except at the crystal surface.

The side lengths of the triangles in the hexagonal projection seen in Fig. 6.3(f) are $d = 16.8 \pm 1$ $\mu$m. When it is assumed that the hexagonal projection arise from a bcc lattice structure oriented in the [111] direction, this side length gives the density $n_{\rm bcc} = 2.3 \pm 0.3 \times 10^8$ cm$^{-3}$. This is in agreement with the expected density and we conclude that a bcc lattice structure is observed. The long-range ordered bcc structures are thus present in spherically symmetric Coulomb crystals with ion numbers down to $\sim 1000$. This is quite a surprising result since MD simulations have predicted that such a long-range order first appear when ion numbers exceed $\sim 10,000$ ions. The presence of bcc structures in the small clusters does not critically depend on the crystal shape, since the bcc structures have also been observed in small prolate and oblate crystals with ion numbers of $\sim 2000$.

Although the projection image in Fig. 6.3(h) at first sight also seem to have the same projected hexagonal structure as Fig. 6.3(f) a closer look reveals that the projected structure is not made up of equilateral triangles. Rather the three angles of the triangle are $\sim 66°$, $\sim 58°$, and $\sim 56°$. The reason for this discrepancy could be found in some micromotion induced distortion of the lattice structure, but the exact cause of the change in the observed projection is at present unknown.

## 6.2 Bi-crystal structures

There are several interesting aspects of the structural properties of two-component Coulomb crystals, which have earlier been studied by the Aarhus Ion Trap

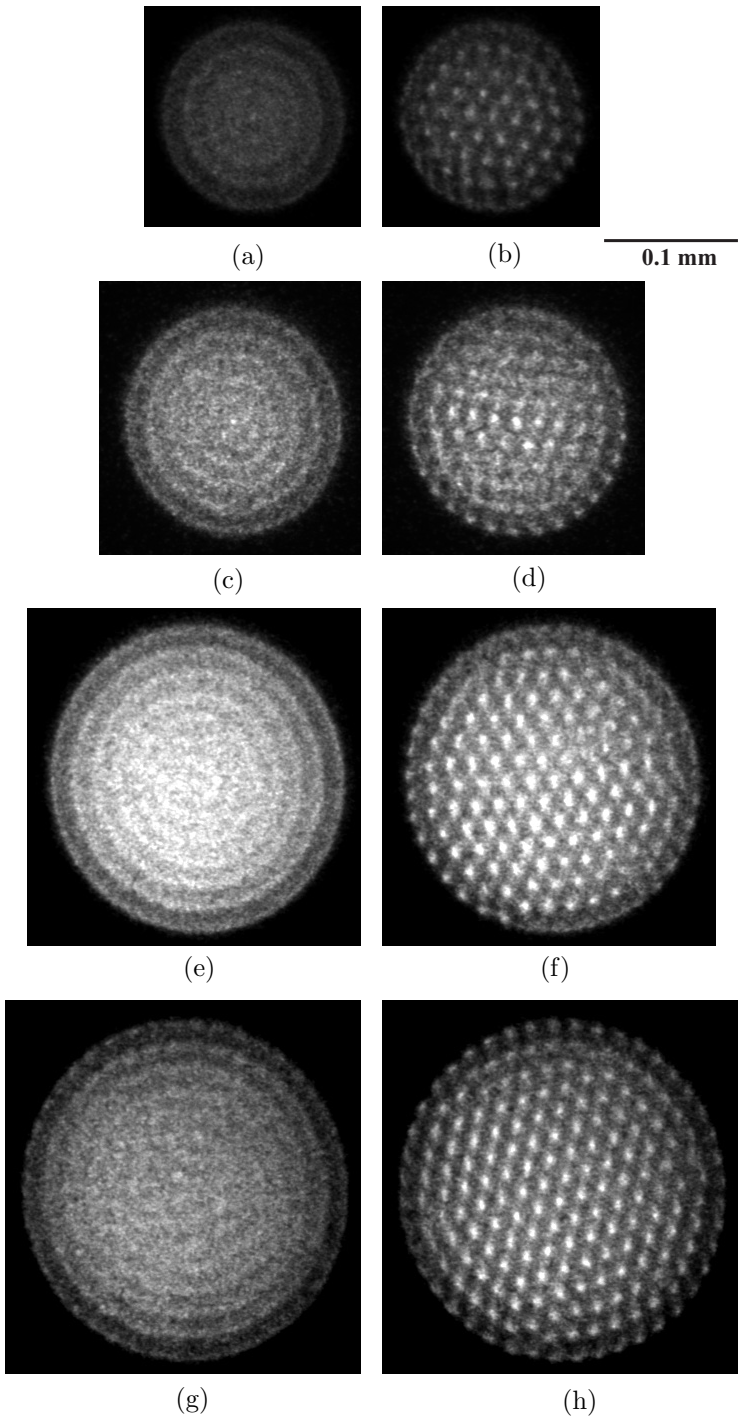


*Fig. 6.3:* Near spherical crystals showing both concentric shell structures (left) and lattice structures (right). The ion crystals contain about 300 ions ((a) & (b)), 700 ions ((c) & (d)), 1400 ions ((e) & (f)), and 2700 ions ((g) & (h)). For the crystals (f) and (h) real long-range order is observed.

Group in bi-crystals consisting of $^{24}Mg^+$ ions and $^{40}Ca^+$ ions. For a review see Refs. [34, 90]. Here we will mainly focus on the structural properties of the central $^{40}Ca^+$ core of $^{40}Ca^+$–$^{44}Ca^+$ bi-crystals. New results are presented which indicate that the concentric shell structure of the central $^{40}Ca^+$ core predicted from MD simulations [34], and observed for bi-crystals trapped in a linear Paul trap [90] is not unique. Instead a transition to a 3D long-range ordered lattice structure exists when the crystal core contains a sufficiently high number of $^{40}Ca^+$ ions.

### 6.2.1 Experimental method

The experiments on $^{40}Ca^+$–$^{44}Ca^+$ bi-crystals were performed in the Paul trap described in Sec. 3.1 and the bi-crystals were produced using the resonant two-photon photo-ionization method described in Chap. 4. In order to study the structural properties of both isotope ions in the crystal laser cooling needs to be applied to the individual isotopes. Due to the isotope shift of the cooling transition (see Tab. 2.1) each isotope ion species has its own unique laser frequencies that is applied for laser cooling. A very elaborate method of applying laser cooling to the individual isotopes would be to manually tune the cooling lasers to each of the isotopes in turn. This is not an ideal experimental situation, because in the process of tuning the cooling lasers to another isotope the trapped ions will inevitably get warm resulting in possible ion losses.

To avoid this we use individual laser systems for Doppler cooling of each of the two calcium isotopes. All the laser systems mentioned in the following are described in Sec. 3.4. For the $^{44}Ca^+$ ions we use the 397 nm Ti:Sapph laser for the $4S_{1/2} \leftrightarrow 4P_{1/2}$ transition, and the 866 nm diode laser for the $3D_{3/2} \leftrightarrow 4P_{1/2}$ transition. See Fig. 2.4 for a level scheme of $Ca^+$. At the time that the experiments were performed there were not two 866 nm diode laser systems available in the laboratory, which would be needed for re-pumping via the $3D_{3/2} \leftrightarrow 4P_{1/2}$ transition for both $Ca^+$ isotopes simultaneously. Instead re-pumping for the cooling transition in $^{40}Ca^+$ was done via the $4P_{3/2}$ state using an 850 nm diode laser and an 854 nm diode laser tuned to the $3D_{3/2} \leftrightarrow 4P_{3/2}$ transition and the $3D_{5/2} \leftrightarrow 4P_{3/2}$ transition, respectively. During the experiments the 850 nm and the 854 nm diode lasers are locked to the same temperature stabilized cavity using a Pound-Drever-Hall lock (see Sec. 3.4.4). The $4S_{1/2} \leftrightarrow 4P_{1/2}$ transition in $^{40}Ca^+$ is covered by 397 nm diode laser, which is locked to an optical cavity using an offset lock.

A schematic of the cooling laser setup is shown in Fig. 6.4. The two laser beams at $\lambda = 397$ nm coming from the diode laser and the Ti:Sapph laser are made co-propagating using a PBS. Shaping of the laser beams using lenses before the PBS is done to ensure a good spatial overlap of the two beams. The $\lambda = 397$ nm laser light is then split in two arms using a $\lambda/2$-plate and a PBS in order to make two power balanced, counter-propagating cooling laser beams at the ion crystal. The $\lambda = 866$ nm laser and the $\lambda = 850$ nm laser light are made co-propagating using a PBS, while the $\lambda = 854$ nm is sent into the Paul trap in the opposite direction. The infrared re-pump laser beams are overlapped with

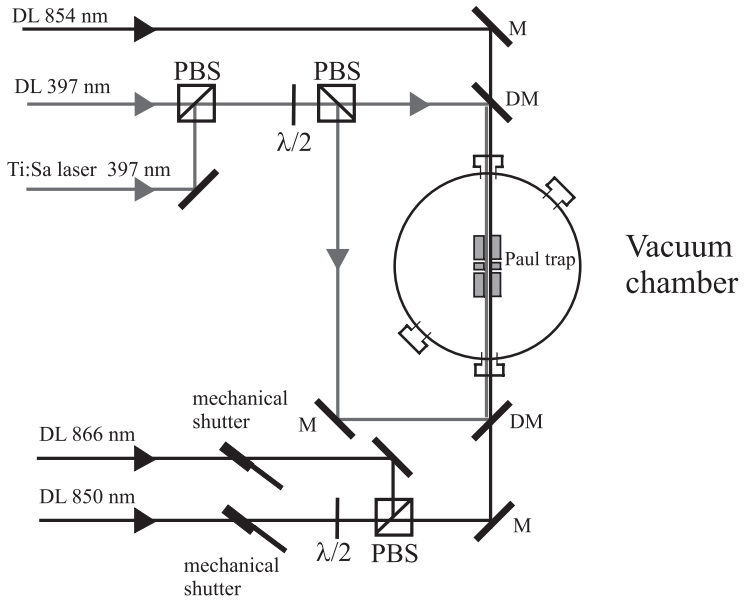


*Fig. 6.4:* Experimental setup for cooling $^{40}Ca^+$ and $^{44}Ca^+$. M: Mirror, DM: Dichroic Mirror, PBS: Polarization Beam Splitter, $\lambda/2$: half wave plate, DL: Diode Laser.

the UV light ($\lambda = 397$ nm) using dichroic mirrors that transmit infrared light and reflects UV light.

In order to be able to distinguish between the two ion isotopes laser cooling is applied in an alternating sequence between $^{40}Ca^+$ and $^{44}Ca^+$. An example of such a sequence for a $^{40}Ca^+$–$^{44}Ca^+$ bi-crystal is shown in Fig. 6.5. The laser cooling of the two isotopes is effectively turned off by introducing mechanical shutters in the laser beam pathways of the re-pump cooling lasers. In the case of the $^{40}Ca^+$ ions the $\lambda = 850$ nm diode laser is blocked and for the $^{44}Ca^+$ ions the $\lambda = 866$ nm diode laser is blocked (see Fig. 6.4). To illustrate both isotopes in the bi-crystals in one picture the RGB color coding scheme is used to color the $^{40}Ca^+$ ions red and the $^{44}Ca^+$ ions blue and then subsequently add the pictures[2]. An example of such a color coded illustration can be seen in Fig. 6.14(a).

### *6.2.2 Central core shell structures in bi-crystals*

The shell structure of the central core of bi-crystals in linear Paul traps has previously been studied for bi-crystals consisting of $^{24}Mg^+$ ions and $^{40}Ca^+$ ions [90]. As mentioned in Chap. 2 the radially mass dependent force will spatially separate the two calcium ion isotopes, such that $^{40}Ca^+$ ions are situated closest

[2] This was done using the image analysis program ImageJ.

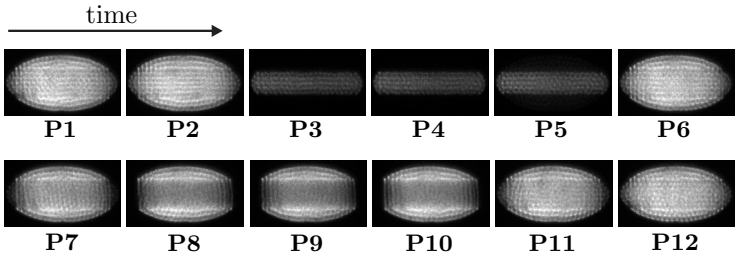


*Fig. 6.5:* Image sequence showing the alternating cooling of $^{40}Ca^+$ and $^{44}Ca^+$ ions. The $^{40}Ca^+$ ions are laser cooled in images **P1**–**P6** and **P11**–**P12**. The $^{44}Ca^+$ ions are cooled in images **P1**, **P2**, and **P6**–**P12**. The crystal contains about 500 $^{40}Ca^+$ ions and 1400 $^{44}Ca^+$ ions. The image acquisition rate is $\sim 6$ Hz, and $U_{\mathrm{rf}} \sim 400$ V.

to the linear Paul trap axis. This can be seen in Fig. 6.6(a), where it is evident that the separation of the two isotopes is total. The observed core shell structure of these bi-crystals is surprisingly similar to the shell structure which have been observed [78] and predicted [91] for one component Coulomb crystals confined in an infinitely long cylindrically symmetric harmonic potential. Here we present observations of shell structure in the $^{40}Ca^+$ core of $^{40}Ca^+$–$^{44}Ca^+$ bi-crystals.

Figure 6.6(a) shows a small bi-crystal containing $\sim 270$ $^{40}Ca^+$ ions and $\sim 500$ $^{44}Ca^+$ ions, which illustrates the general structural properties of the bi-crystals. The inner $^{40}Ca^+$ core of the crystal has a cylindrical shell structure with a string of twelve $^{40}Ca^+$ ions on the trap axis surrounded by other $^{40}Ca^+$ ions forming three cylindrical shells. The presence of the $^{40}Ca^+$ ions in the bi-crystal is observed to have only a weak influence on the spheroidal shape of the outer envelope of the $^{44}Ca^+$ ions. On the other hand the cylindrical envelope of the $^{40}Ca^+$ core is indeed shaped by the $^{44}Ca^+$ ions surrounding the $^{40}Ca^+$ core. This manifests itself very explicitly in Fig. 6.6(b), where the three outer $^{44}Ca^+$ shells clearly have a spheroidal shape and the inner $^{40}Ca^+$ ions core have one cylindrical shell surrounding a string of 11 $^{40}Ca^+$ ions.

Figure 6.7 shows the projection onto the $x$-axis of the $^{40}Ca^+$ fluorescence intensity from a radial cross section though a $^{40}Ca^+$–$^{44}Ca^+$ bi-crystal consisting of $\sim 550$ $^{40}Ca^+$ ions and $\sim 1450$ $^{44}Ca^+$ ions at three different end-cap voltages. The crystal shell structure is evident from the local intensity maxima and minima in the three graphs. The graph plotted with ■ data points and featuring seven local intensity maxima reflects the crystal structure where the $^{40}Ca^+$ ion core has one $^{40}Ca^+$ ion string surrounded by three cylindrical ion shell structures. At another setting of the end-cap potential the crystal has become more elongated and the ion string in the center of the ion core has disappeared, which gives the projection plotted with ▲ data points and featuring six local intensity maxima that indicate that only three shells are present in the $^{40}Ca^+$ crystal core. The graph plotted with ● data points and marked 'transition' is the $^{40}Ca^+$ core projection when the ion string is not complete. A small peak in the center

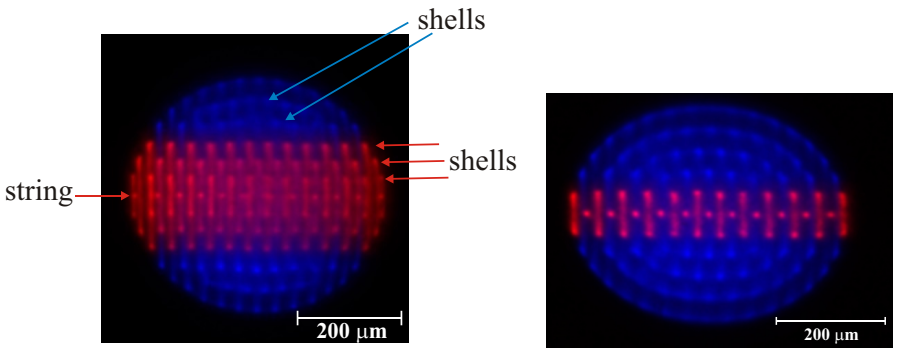


(a) (b)

*Fig. 6.6:* Bi-crystals with cylindrical shell structure. (a) The crystal contains $\sim 270$ $^{40}Ca^{+}$ and $\sim 500$ $^{44}Ca^{+}$ ions and the $^{40}Ca^{+}$ ion density is $n_0 = 1.0 \times 10^8$ cm$^{-3}$. (b) The crystal contains $\sim 100$ $^{40}Ca^{+}$ and $\sim 800$ $^{44}Ca^{+}$ ions and the $^{40}Ca^{+}$ ion density is $n_0 = 1.3 \times 10^8$ cm$^{-3}$.

of this graph indicates that a sharp transition between the two structures does not exist, but instead ions gradually start to disappear from the Paul trap axis when the end-cap potential is lowered.

In Fig. 6.8 the number of shells in the Coulomb crystal shown in Fig. 6.7 has been plotted against the dimensionless linear ion density of the $^{40}Ca^{+}$ ions, which is defined as

$$\lambda = \frac{\sigma}{e} a_{\mathrm{ws}}, \tag{6.1}$$

where $a_{\mathrm{ws}}$ is the Wigner-Seitz radius of the ions defined by $\frac{4}{3}\pi a_{\mathrm{ws}}^3 = n_0^{-1}$, and $\sigma$ is the linear charge density of the $^{40}Ca^{+}$ ions defined as the $^{40}Ca^{+}$ ion charge density per unit length of the Paul trap axis. For the cylindrical $^{40}Ca^{+}$ core of the crystal we calculate $\sigma$ from

$$\sigma = \pi n_0 R^2 a_{\mathrm{ws}}, \tag{6.2}$$

where $R$ is the radial distance from the Paul trap axis to the outer $^{40}Ca^{+}$ ion shell plus the half of a $^{40}Ca^{+}$ ion inter-shell distance. The points in Fig. 6.8 plotted in-between the reported shell structures are transitional structures corresponding to the transition ion core structure shown in Fig. 6.7. The plot reveals that the number of shells increases for increasing $\lambda$. I Ref. [91] MD simulations of ions in a infinitely long cylindrically symmetric static potential showed that the structure with 1 string + 3 shells appears at $\lambda \sim 19.9$ and the structure with 4 shells appear at $\lambda \sim 26.6$, which agrees with observations presented in Fig. 6.8.

### *6.2.3 Lattice structure in the $^{40}Ca^{+}$ ion core*

The observed structures of the $^{40}Ca^{+}$ ion core of bi-crystals presented so far in this section are in good agreement with the cylindrical shells predicted by

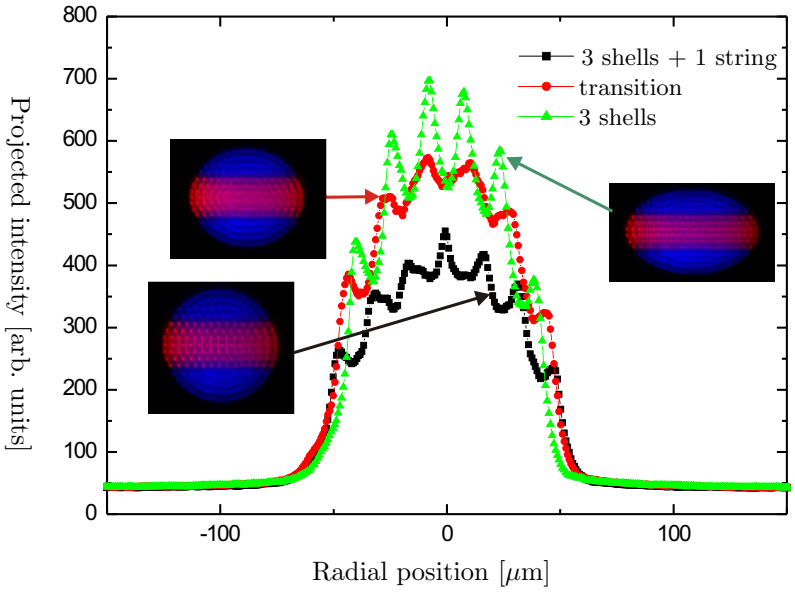


*Fig. 6.7:* The projected radial intensity of the $^{40}Ca^{+}$ ion core for a bi-crystal consisting of $\sim 550$ $^{40}Ca^{+}$ ions and $\sim 1450$ $^{44}Ca^{+}$ ions at three different end-cap voltages. The ion density of the $^{40}Ca^{+}$ ions is $\sim 2.2 \times 10^{8}$ cm$^{3}$.

the MD simulations for infinitely long single component crystals [91] and also observed and predicted for bi-crystals consisting of $^{40}Ca^{+}$ ions and $^{24}Mg^{+}$ ions [34, 90]. The crystals presented in the following do, however, not exhibit this shell structure, but instead there are indications of a 3D long range ordered lattice structure.

An example of such a bi-crystal is shown in Fig. 6.9. The bi-crystal consists of $\sim 1500$ $^{40}Ca^{+}$ ions and $\sim 2000$ $^{44}Ca^{+}$ ions and the density of $^{40}Ca^{+}$ ions is $n_0 \sim 4.0 \times 10^{8}$ cm$^{-3}$. The observed projected structure is a rectangular structure having side lengths $h = 12.6 \pm 0.3$ $\mu$m and $w = 7.8 \pm 0.3$ $\mu$m. This gives the ratio $h/w \sim 1.62 \pm 0.07$ between the sides of the rectangle. Similar to the findings in Sec. 6.1.2 this indicates that the $^{40}Ca^{+}$ ion core structure is a fcc lattice viewed along the [211] direction where a ratio of $h/w = 1.63$ is expected. The ion density calculated from the $h$ and $w$, assuming a fcc structure [211] projection, is $n_{\mathrm{fcc}} = 3.8 \pm 0.2 \times 10^{8}$ cm$^{-3}$ in good agreement with the expected ion density of $n_0 \sim 4.0 \times 10^{8}$ cm$^{-3}$.

Figure 6.10 shows the $^{40}Ca^{+}$ part of the same crystal at different end-cap voltages and it is observed that the lattice structure is present at all four end-cap voltages. The lattice structure is oriented along the Paul trap axis for the bi-crystal, which was not the case for the fcc structure observed for the single component $^{40}Ca^{+}$ crystal in Fig. 6.2(b) Sec. 6.1.2. A reasonable explanation for this alignment of the lattice structure along the Paul trap axis is that the

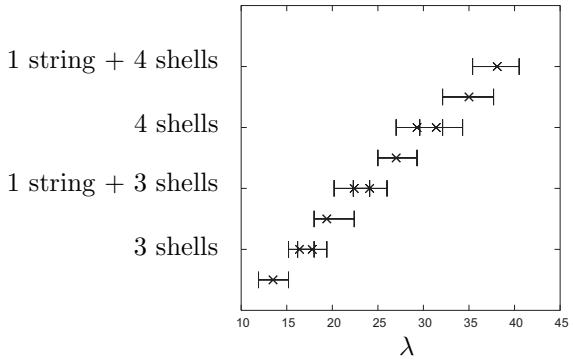


*Fig. 6.8:* Number of shells in the crystal plotted against the dimensionless linear ion density.

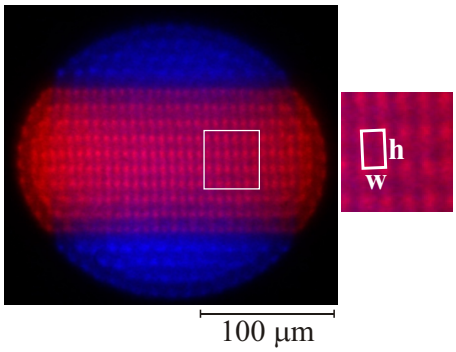


*Fig. 6.9:* Large bi-crystal containing $\sim 1500$ $^{40}Ca^{+}$ and $\sim 2000$ $^{44}Ca^{+}$ ions. The insert highlights the rectangular structure in the $^{40}Ca^{+}$ ion core and defines lengths $h$ and $w$.

cylindrically shaped outer envelope of the $^{40}Ca^{+}$ ions imposes a boundary condition on the lattice that determines the orientation of the fcc structure. This explanation is supported by the observation that in the single component case the orientation of the lattice structure does not exhibit the same stability as in the two component case.

### *6.2.4 Comparison with simulations*

To get a better understanding of the observed bi-crystal structures MD simulations were performed by Esben S. Nielsen in collaboration with Thierry Matthey [92, 93].

Conventionally the ions in the MD simulations are confined by the harmonic pseudopotential introduced in Eq. (2.6)

$$\Phi_{\mathrm{ps}}(r,z) = \frac{1}{2}M(\omega_r^2 r^2 + \omega_z^2 z^2), \tag{6.3}$$

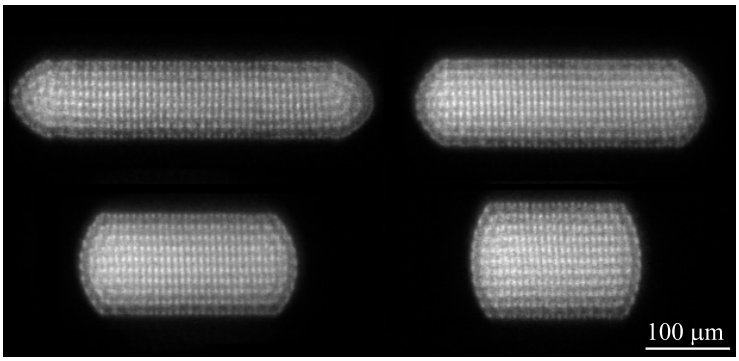


*Fig. 6.10:* The $^{40}Ca^{+}$ component of a bi-crystal containing $\sim 1500$ $^{40}Ca^{+}$ and $\sim 2000$ $^{44}Ca^{+}$ at different end-cap voltages.

that describes the dynamics of an ion in the Paul trap when the micromotion is ignored. In the MD simulations presented here we shall sometimes use the full time-dependent electric potential (see Sec. 2.1)

$$\phi_{\mathrm{tot}}(x,y,z,t) = -\frac{1}{2}U_{\mathrm{rf}}\cos\Omega_{\mathrm{rf}}t\frac{x^2-y^2}{r_0^2} - \frac{1}{2}\eta U_{\mathrm{ec}}\frac{x^2+y^2-2z^2}{z_0^2}, \tag{6.4}$$

instead of the pseudopotential in Eq. (6.3). The projection in the $x'y'$ plane[3] of a simulated $^{40}Ca^{+}$–$^{44}Ca^{+}$ bi-crystal using the full electric potential is shown in Fig. 6.11 at different stages of the micromotion during half an oscillation period. The projection at $\Omega_{\mathrm{rf}}t = 2\pi N + \pi/2$ shown in Fig. 6.11(b) is the stage at which the highest degree of rotational symmetry is exhibited and the projections shown in the remainder of this section are consequently from $\Omega_{\mathrm{rf}}t = 2\pi N + \pi/2$.

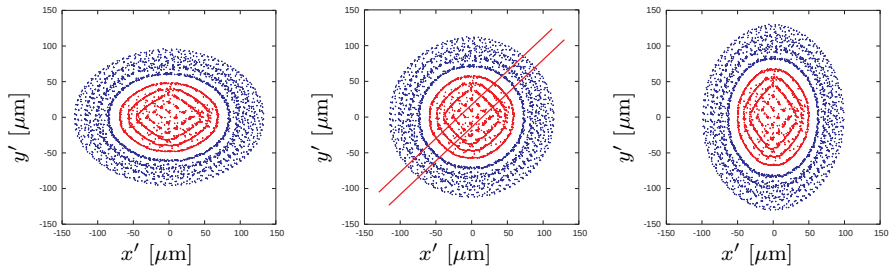


(a) $\Omega_{\mathrm{rf}}t = 2\pi N$ (b) $\Omega_{\mathrm{rf}}t = 2\pi N + \pi/2$ (c) $\Omega_{\mathrm{rf}}t = 2\pi N + \pi$

*Fig. 6.11:* Projection in the $x'y'$-plane of a simulated bi-crystal containing 1509 $^{40}Ca^{+}$ ions and 1979 $^{44}Ca^{+}$ ions at three different stages of the micromotion. The lines in (b) indicate the region used for the projections in Fig. 6.13(b) and Fig. 6.14(b). $N$ is an integer.

[3] The unit vectors $\hat{x}'$ and $\hat{y}'$ were defined in Fig. 2.1.

Figure 6.12 shows projection of an ion crystal simulated at two different end-cap potentials using both the pseudopotential (Fig. 6.12(a) & (c)) and the full time-dependent potential (Fig. 6.12(b) & (d)). Figure 6.12(a) shows a setting of the end-cap potential for which the pseudopotential simulation predicts a crystal structure with three $^{40}Ca^{+}$ ion shells. Using the full potential instead but with the same trapping parameters in Fig. 6.12(b) we see that a lattice structure appears in place of the inner shell. Apart from the appearing lattice structure the two outer $^{40}Ca^{+}$ ion shells do no longer have the rotational symmetry observed in Fig. 6.12(a). At another setting of the end-cap potential both the pseudopotential simulation and the full potential simulation predicts a string of $^{40}Ca^{+}$ ions on the Paul trap axis, as seen in Fig. 6.12(c) and Fig. 6.12(d), and a rotationally symmetric shell structure.

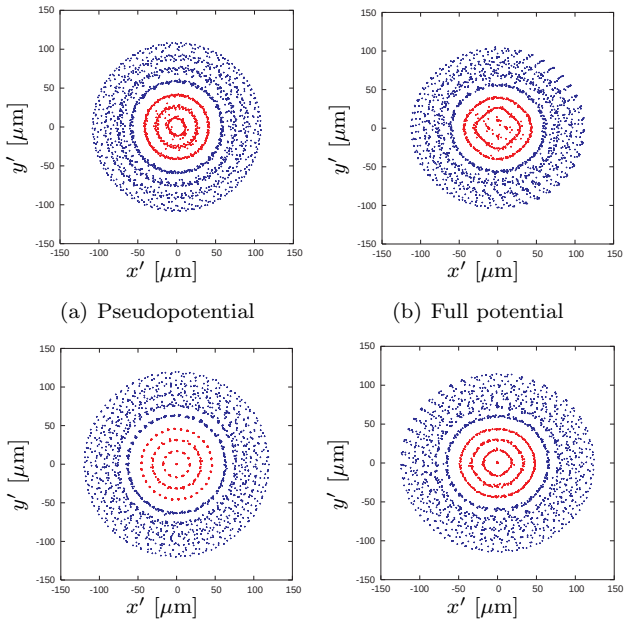


(a) Pseudopotential (b) Full potential

(c) Pseudopotential (d) Full potential

*Fig. 6.12:* Projection in the $x'y'$ plane of a simulated ion Coulomb crystal containing 553 $^{40}Ca^{+}$ ions and 1460 $^{44}Ca^{+}$ ions at the end-cap potentials $U_{ec} = 14.31$ V ((a) & (b)) and $U_{ec} = 18.26$ V ((c) & (d)). $U_{rf} = 400$ V. The corresponding trap frequencies can be calculated using the Paul trap parameters given in Sec. 3.1.

For a direct visual comparison between the experiments and the simulations a projection of the region indicated in Fig. 6.11(b) is made resulting in the projection images seen in Figs. 6.13 and 6.14 which are compared experimentally observed bi-crystals.

In Fig. 6.13 an observed bi-crystal exhibiting shell structure in the $^{40}Ca^{+}$ core is compared to a simulation, where the pseudopotential is used. The num-

ber of ions as well as the trap parameters have been chosen to correspond to the experimental parameters. It is seen that there is a nice visual agreement between the observed crystal and the projection of the simulation. The similarity between the two is expected because the pseudopotential indeed predicts a shell structure for the central $^{40}Ca^{+}$ core.

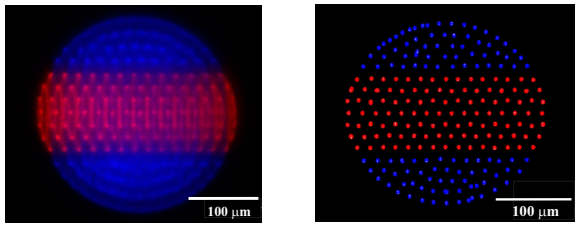


(a) Observed (b) Pseudopotential

*Fig. 6.13:* (a) Observed bi-crystal with $\sim$ 500 $^{40}Ca^{+}$ ions and $\sim$ 1400 $^{44}Ca^{+}$ ions. (b) Simulated using the pseudopotential bi-crystal with 553 $^{40}Ca^{+}$ ions and 1460 $^{44}Ca^{+}$ ions. The rf-potential is $U_{\mathrm{rf}} = 400$ V. The projected region of the crystal is indicated in Fig. 6.11(b).

Figure 6.14 shows a comparison between the large $^{40}Ca^{+}$ bi-crystal from Fig. 6.9 and crystal simulations that use the full potential (Fig. 6.14(b)) as well as the pseudopotential (Fig. 6.14(c)). Whereas the pseudopotential simulation clearly fails to reproduce the observed crystal, the resemblance between the full potential simulation and the observed crystal is striking in that they both exhibit a rectangular structure in the crystal projection of the $^{40}Ca^{+}$ core.

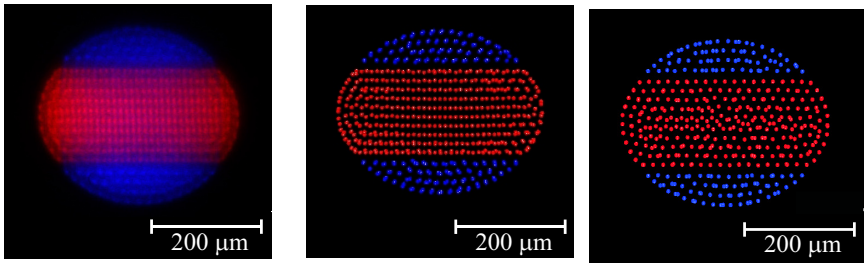


(a) Observed (b) Full potential (c) Pseudopotential

*Fig. 6.14:* An observed bi-crystal with $\sim$ 1500 $^{40}Ca^{+}$ ions and $\sim$ 2000 $^{44}Ca^{+}$ ions is shown in (a). Simulated bi-crystals with 1509 $^{40}Ca^{+}$ ions and 1979 $^{44}Ca^{+}$ ions using the full potential (b) and the pseudopotential (c). The rf-potential is $U_{\mathrm{rf}} = 400$ V. The projected region of the crystal is indicated in Fig. 6.11(b).

A more careful examination of the crystal structure of the $^{40}Ca^{+}$ ion core in the simulation reveals that the ions are arranged in an fc-orthorhombic structure. The lattice cell of the fc-orthorhombic structure is shown in Fig. 6.15. The

ratio of the sides of the rectangular shaped structure seen in the projection of this crystal structure in Fig. 6.14(b) is $h/w = \sqrt{3} \simeq 1.73$. This does not agree with the observed aspect ratio of $h/w \sim 1.62 \pm 0.07$ (see Fig. 6.9), which is found for the observed crystal structure in Fig. 6.14(a). The result $h/w \sim 1.62 \pm 0.07$ rather indicates that the observed structure is an fcc structure, which predicts $h/w \simeq 1.63$. Because the binding energy difference between the fcc and fc-orthorhombic structures is small it is possible though that experimental factors that are not accounted for in the simulations make the fcc structure more favorable than the fc-orthorhombic structure.

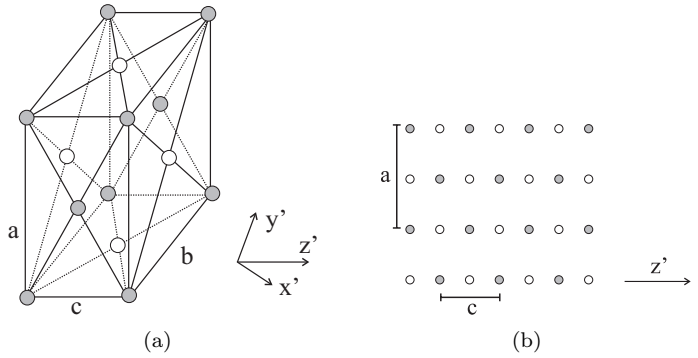


*Fig. 6.15:* (a) Face-Centered Orthorhombic lattice cell with the side lengths $c = l$ and $a = b = \sqrt{3}l = 1.73l$. The lattice orientation with respect to the $(x', y', z')$-coordinate system is indicated. (b) The projection of the lattice as seen from the camera. The white and the gray lattice points relate to the different layers in the projection.

## 6.3 Conclusion

We have observed that for large one component ion Coulomb crystals with ion numbers exceeding 10,000 there exist a long-range structural order throughout almost the entire crystal. The observed 3D long-range ordered lattice structures for these crystals are presumably bcc and fcc. In contradiction with earlier theoretical predictions we have observed transitions to bcc lattice structures in smaller one component spherical crystals of ion numbers down to $\sim 1000$ ions.

In the case of two-component Coulomb crystals we have seen that the shell structure is not an unique property of the central core of the bi-crystal. Instead, for certain configurations of the trapping parameters and sizes of the Coulomb crystals, there exists a transition to a 3D long-range ordered lattice structure in the central core. The MD simulations of the bi-crystals indicate that the existence of the lattice structure in the crystal core is induced by the time variation of the confining rf-potential of the linear Paul trap. The simulations furthermore predict that this lattice has an fc-orthorhombic structure with projection ratio $h/w \simeq 1.73$, which is not fully consistent with the observed $h/w = 1.62 \pm 0.07$.

# 7. LIGHT MEMORY PHYSICS

In this second part of the Thesis we will turn to the subject of storage of quantum states of light in ion Coulomb crystals. The use of the word 'storage' means here that the quantum state of a light field is mapped onto some metastable state of the ions, or more generally some metastable state of matter, and then later, on demand, retrieved as a light field that has the same quantum state as the original light field.

The recent efforts within quantum information science to manipulate the quantum states of matter and light have stimulated the research on the subject of light storage. A major issue in quantum information science is the desire to make a quantum computer, which can solve tasks that are in practice unsolvable on a classical computer [94]. One of the challenges in quantum information processing is the transport of unknown quantum states between specified locations [95] as well as having quantum memories with short access times. Photons are good candidates for carrying such quantum states. The quantum states can be encoded in the polarization state or the spatial wave function of the photon. As carriers of information photons have the advantage that they are robust and very fast, but at the same time this also implies that they are difficult to localize and store. In the ideal quantum information scheme one would like to store and manipulate quantum states in matter and then map these states onto photons, when desired. A network of such quantum information processors where photons act as the carriers of quantum information between the nodes of the network has been proposed [96].

The spin states of atoms are good candidates for a long-lived temporary storage of photons. At the same time several quantum information processing schemes are based on the manipulation of the spin states of atoms [97–99] or in particular ions [6, 18, 100, 101]. In this context it makes good sense to study the subject of coherent transfer of quantum states carried by light onto internal states of atoms. In order to be useful for quantum computational schemes reliable storage of quantum states on the level of individual quanta has to be achieved.

The conceptually most simple approach is to store single photons in individual atoms using stimulated Raman adiabatic passage (STIRAP) techniques [1] to make coherent reversible mapping of the photon state onto the atomic spin states. At the same time this is a difficult approach as the absorption cross section of an isolated atom is very small. Placing the atom in a high Q resonator effectively increases the absorption cross section by a factor determined by the number of photon round trips in the cavity. When the absorption cross section

is sufficiently enhanced we enter the strong-coupling regime of cavity quantum electrodynamics (QED) [2]. Experimentally it is extremely challenging to realize the strong-coupling regime and to localize the atom inside the mode volume of the cavity, but there is still much experimental progress in this field.

A different approach is to increase the number of atoms and in this way increase the total absorption cross section. Absorption in an atomic ensemble would normally lead to dissipation, i.e., loss of information about the quantum state of the incoming photon. This information loss can, however, be avoided using special techniques originally put forward by Ref. [8, 102]. In this approach the quantum state of the photon is mapped onto a coherently driven atomic media using dissipation-free adiabatic passage techniques. It is based on Raman adiabatic transfer of the quantum state of photons to collective atomic excitations using *electromagnetically induced transparency* (EIT) [3] in which the optical properties of atoms can be manipulated by an external classical control field.

## 7.1 Coupling between cavity field mode and atoms

When the optical density of the atomic medium used for the light storage is low, it is necessary to enhance the interaction between the photon and the atom by means of an optical cavity surrounding the atomic medium. The ideas regarding this intra-cavity light storage, originally put forward Ref. [8, 102], are presented in this section. First, EIT and the adiabatic passage techniques for such a setup are discussed. Next, storage of an one photon state utilizing these techniques in a way that maximizes the fidelity of the storage will be discussed.

### 7.1.1 Dark states

To introduce the basic idea of a controlled and reversible quantum state transfer via STIRAP, let us first consider an ensemble of $N$ identical 3-level $\Lambda$-atoms with two metastable eigenstates $|b\rangle$ and $|c\rangle$ as the two lower states and an exited state $|a\rangle$ with decay rate $\gamma_a$. The energy of an eigenstate $|\mu\rangle$ is denoted $\hbar\omega_\mu$ and we assume that $\hbar\omega_b = 0$. The atoms interact with a quantized mode of an optical resonator that couples the states $|b\rangle$ and $|a\rangle$ and a classical coupling field that couples the states $|c\rangle$ and $|a\rangle$. The level scheme of a single atom is illustrated in Fig. 7.1(a), where $\Omega(t)$ is the Rabi frequency of the classical coupling field, and $g$ is the single atom–single photon coupling constant of the $|b\rangle \leftrightarrow |a\rangle$ transition. The coupling constant $g$ is given by the expression

$$g = \frac{\mathcal{D}}{\hbar}\sqrt{\frac{\hbar\omega_{ca}}{2\epsilon_0 V}}, \tag{7.1}$$

where $V$ is the cavity mode volume, $\mathcal{D}$ is the dipole moment of the $|b\rangle \leftrightarrow |a\rangle$ transition, and $\omega_{ca} \equiv \omega_a - \omega_c$. For simplicity we assume that the coupling constant $g$ is equal for all the atoms. The dynamics of this system is given by

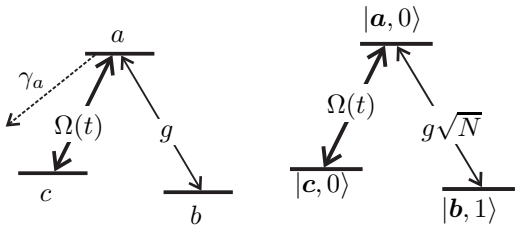


*Fig. 7.1:* (a) Interaction level scheme of a single atom interacting with a single quantized cavity mode and a classical control field of Rabi frequency $\Omega(t)$. (b) Interaction of a single photon in the cavity with an ensemble of $N$ 3-level atoms in the lowest excited states.

the complex Hamiltonian [103]

$$\begin{aligned} H =& \hbar\omega a^\dagger a + \hbar(\omega_a - i\gamma_a)\sum_{i=1}^{N}\sigma_{aa}^j + \hbar\omega_c\sum_{i=1}^{N}\sigma_{cc}^j \\ &+ \left[\hbar g\hat{a}\sum_{i=1}^{N}\hat{\sigma}_{ab}^i + \hbar\Omega(t)e^{-\nu t}\sum_{i=1}^{N}\hat{\sigma}_{ac}^i + \text{h.c.}\right] \end{aligned} \tag{7.2}$$

where $\nu$ is the optical frequency of the classical coupling field and $\hat{\sigma}_{\mu\nu}^i = |\mu\rangle_{ii}\langle\nu|$ is the spin flip operator between the states $|\mu\rangle_i$ and $|\nu\rangle_i$ in the $i$th atom. The annihilation (creation) operator of one photon in the cavity mode is denoted by $\hat{a}$ ($\hat{a}^\dagger$) [104].

We now assume that the cavity mode is resonant with the $|b\rangle \leftrightarrow |a\rangle$ transition and the classical control laser field is resonant with the $|c\rangle \leftrightarrow |a\rangle$ transition. When working in a frame rotating with optical frequencies and using the rotating wave approximation the interaction part of the Hamiltonian (Eq. (7.2)) reads

$$\tilde{H} = \hbar g\hat{a}\sum_{i=1}^{N}\hat{\sigma}_{ab}^i + \hbar\Omega(t)\sum_{i=1}^{N}\hat{\sigma}_{ac}^i + \text{h.c.} - i\hbar\gamma_a\sum_{i=1}^{N}\sigma_{aa}^i. \tag{7.3}$$

The symmetry of this interaction Hamiltonian invites us to introduce the collective operators $\hat{\Sigma}_{ab} = \sum_{i=1}^{N}\hat{\sigma}_{ab}^i$ and $\hat{\Sigma}_{ac} = \sum_{i=1}^{N}\hat{\sigma}_{ac}^i$. When all $N$ atoms are initially prepared in the state $|b\rangle$, which we will denote by $|\boldsymbol{b}\rangle \equiv |b_1 \dots b_N\rangle$ it is obvious that the subspace spanned by eigenstates of the collective operators $\hat{\Sigma}_{ab}$ and $\hat{\Sigma}_{ac}$ must consist of symmetric atomic states. More specifically the

subspace is spanned by the symmetric state vectors

$$\begin{aligned}
|\boldsymbol{b}\rangle &= |b_1 \dots b_N\rangle, \\
|\boldsymbol{a}\rangle &= \tfrac{1}{\sqrt{N}} \textstyle\sum_{i=1}^{N} |b_1 \dots a_i \dots b_N\rangle, \\
|\boldsymbol{c}\rangle &= \tfrac{1}{\sqrt{N}} \textstyle\sum_{i=1}^{N} |b_1 \dots c_i \dots b_N\rangle, \\
|\boldsymbol{aa}\rangle &= \tfrac{1}{\sqrt{2N(N-1)}} \textstyle\sum_{i\neq j=1}^{N} |b_1 \dots a_i \dots a_j \dots b_N\rangle, \\
|\boldsymbol{ac}\rangle &= \tfrac{1}{\sqrt{N(N-1)}} \textstyle\sum_{i\neq j=1}^{N} |b_1 \dots a_i \dots c_j \dots b_N\rangle, \quad \text{etc.},
\end{aligned} \tag{7.4}$$

which we will refer to as the collective atomic states. Dicke discussed the symmetric collective states in the simpler case of 2-level atoms in 1954 [105]. These so-called Dicke states are of relevance in the description of superradiance from atomic ensembles [106].

In the following we will consider the simplest non-trivial case, where there is one photon in the cavity mode while the atoms are in the $|\boldsymbol{b}\rangle$ state. This state we will denote by $|\boldsymbol{b}, 1\rangle$ where the number of photons in the cavity mode is indicated by the second index in the state vector. The interaction Hamiltonian in Eq. (7.3) couples the $|\boldsymbol{b}, 1\rangle$ state to two other states of the combined atom-field system, namely $|\boldsymbol{b}, 1\rangle \overset{\tilde{H}}{\longleftrightarrow} |\boldsymbol{a}, 0\rangle \overset{\tilde{H}}{\longleftrightarrow} |\boldsymbol{c}, 0\rangle$. In the basis consisting of these three state vectors, $\mathcal{B} = \{|\boldsymbol{a}, 0\rangle, |\boldsymbol{b}, 1\rangle, |\boldsymbol{c}, 0\rangle\}$, the interaction Hamiltonian is represented by the $3 \times 3$ matrix

$$\tilde{H}_{\mathcal{B}} = \hbar \begin{bmatrix} -i\gamma_a & g\sqrt{N} & \Omega^*(t) \\ g\sqrt{N} & 0 & 0 \\ \Omega(t) & 0 & 0 \end{bmatrix}. \tag{7.5}$$

The eigenvalues of this matrix are given by $\lambda_\pm = -i\frac{\gamma_a}{2} \pm \sqrt{g^2 N + \Omega^2 - (\frac{\gamma_a}{2})^2}$ and $\lambda_0 = 0$. The instantaneous (adiabatic) eigenstate corresponding to the zero eigenvalue $\lambda_0$ reads

$$\begin{aligned}
|D, 1\rangle &= \frac{\Omega|\boldsymbol{b}, 1\rangle - g\sqrt{N}|\boldsymbol{c}, 0\rangle}{\sqrt{\Omega^2 + g^2 N}} = \cos\theta(t)|\boldsymbol{b}, 1\rangle - \sin\theta(t)|\boldsymbol{c}, 0\rangle, \\
\tan\theta(t) &\equiv \frac{g\sqrt{N}}{\Omega(t)}
\end{aligned} \tag{7.6}$$

where the *mixing angle* $\theta(t)$ has been introduced. The important feature of the $|D, 1\rangle$ eigenstate is that it does not contain the excited $|\boldsymbol{a}, 0\rangle$ state and is thus immune to spontaneous emission from this state. For this reason this eigenstate is called a dark state (see, e.g., [107]) while the eigenstates corresponding to the eigenvalues $\lambda_\pm$ are called bright states because they are superpositions of all three states in the basis $\mathcal{B}$. More generally if the number of photons in the cavity is $n$, where $n \ll N$, the dark states of the Hamilton become [102]

$$|D, n\rangle_N = \sum_{i=1}^{N} \sqrt{\frac{n!}{k!(n-k)!}} \frac{(-g)^k N^{k/2} \Omega^{n-k}}{(g^2 N + \Omega^2)^{n/2}} |\boldsymbol{c}^k, n-k\rangle, \tag{7.7}$$

i.e., the dark states are composed by the symmetric Dicke-like atomic states presented in Eq. (7.4) containing $k$ atoms in the level $|c\rangle$ and the rest in level $|b\rangle$ and field states with $n-k$ photons. In Ref. [108, 109] the dark states $|D, n\rangle$ are shown to correspond to elementary excitations of bosonic quasiparticles called dark state polaritons.

### 7.1.2 Stimulated Raman adiabatic passage

To discuss the mechanisms behind STIRAP [1, 110], which has already been explored in the context of cavity QED with single atoms [111] we consider the asymptotic behavior of the dark states. From Eq. (7.6) we see that when the mixing angle is $\theta \sim 0$ the dark state is $|D, 1\rangle = |\boldsymbol{b}, 1\rangle$ and when $\theta \sim \pi/2$ the dark state is $|D, 1\rangle = |\boldsymbol{c}, 0\rangle$. This means that by varying the mixing angle adiabatically, i.e., varying the Rabi-frequency of the classical control field $\Omega(t)$, the dark state of the atom-cavity system can be rotated from a cavity-like state (where the excitation is of photon nature) to an atom-like state (where the excitation is shared in the collective state of the atoms). Later we will state more quantitatively what is meant with the term 'adiabatically' here.

In the limit where the control field is strong $\Omega(t) \gg g\sqrt{N}$ ($\theta(t) \sim 0$) the atoms do not interact with the cavity mode and the dark state resembles the 'bare' cavity mode. This coherently induced transparency of the $|c\rangle \leftrightarrow |a\rangle$ transition of an atomic ensemble is called *electromagnetically induced transparency* (EIT) [3, 112], and in the case where the atoms are situated in a cavity it is called intra-cavity EIT [113]. The transparent atomic medium allows photons to circulate in the cavity as if it was empty, and the lifetime of the dark state excitation is then set by the cavity decay rate.

In the opposite limit where the control field is weak, i.e., $\Omega(t) \ll g\sqrt{N}$ ($\theta(t) \sim \pi/2$), the dark state is as mentioned purely an atomic excitation with no photons in the cavity. The lifetime of the dark state is then obviously not limited by the cavity decay rate, but set by the decay rate of the collective atomic state. This is ultimately set by the decoherence rate $\gamma_{bc}$ of the two metastable states $|b\rangle$ and $|c\rangle$, which can be much smaller than the cavity decay rate, i.e., the photon is stored in the atomic collective states.

### 7.1.3 Decoherence and loss

At this stage it is interesting to ask how fragile the collective Dicke like states of Eq. (7.4) are with respect to decoherence and losses. After all, the decoherence of some many-particle states are known to exhibit linear ($\propto N$) or even quadratic ($\propto N^2$) scaling behavior with the number of particles involved (see [114]). This is not the case with the Dicke-like states. It can be argued [103] that if one atom of an $N$-atom Dicke like state is spin flipped (decays) the resulting state is almost identical to an $N-1$ atom Dicke like state with an error that scales as $\sim 1/N$. This scaling property is found to compensate the factor $N$ of the total probability of a spin flip error to occur in any atom. So the characteristic decoherence rate of the state $|\boldsymbol{c}, 0\rangle$ describing a single stored photon is indeed

given by the single atom decay rate $\gamma_{bc}$. We can therefore conclude that the symmetric Dicke like states are very robust with respect to decoherence.

To conclude we have argued that the coupling of the dark state to the environment can be changed by varying the Rabi frequency of the classical control field $\Omega(t)$. In the next section we will present a scheme that makes use this to load a single incoming photon wave packet in the dark state of the atom cavity system and also allows for subsequent release the wave packet after some storage time.

## 7.2 Transfer of an One-photon State

In this section we will present the ideas on how to transfer a single photon state from a free field onto the dark state of the cavity atom system and back again. The derivation of the results presented can be found in Fleischhauer *et al.* [8] and Lukin *et al.* [102]. Here we will not try to repeat these derivations, but rather introduce the model and state the main results.

### 7.2.1 Dark state coupling to outside states

The cavity-atom dark states introduced in the previous section were derived under the assumption that the cavity mode is decoupled from it's surroundings. We will now explore what happens when photons are allowed to leak in and out of the cavity.

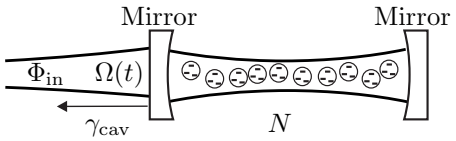


*Fig. 7.2:* Overview of basic setup.

To this end an effective one-dimensional model is considered. The $z$-axis is assumed to be the propagation axis of the incoming and outgoing modes. We assume that we have a traveling wave Fabry-Perot like cavity with one partially transmitting input mirror (at $z = 0$) and the other mirror being 100% reflecting.

The coupling of the cavity modes to the environment is modeled by introducing a continuum of free space modes with field creation operators $\hat{b}_k^\dagger$ which are coupled to the cavity modes with a coupling constant $\kappa_{\rm cav}$. The effective Hamiltonian for this coupling is governed by

$$V = \hbar \sum_k \kappa_{\rm cav} \hat{a}^+ \hat{b}_k + \text{h.c.}, \tag{7.8}$$

which added to the cavity atom Hamiltonian given in Eq. (7.2), gives the complete Hamiltonian for the model. The initial state of the free field is taken to

be $|\Psi_{in}(t)\rangle = \sum_k \xi_k(t)|1_k\rangle$, where $\xi_k(t) = \xi_k(t_0)e^{-i\omega_k(t-t_0)}$. The state $|1_k\rangle$ describes a state with one photon in the free space mode $k$ outside the cavity. In the continuum limit, i.e., $\xi_k(t) \to \xi(\omega_k, t)$, the envelope "wave function" of the incoming wave packet is given by $\Phi_{\rm in}(z,t) = (L/2\pi c)\int d\omega_k \xi(\omega_k, t)e^{ikz}$, where $L$ is the quantization length (for further details see [8]).

To describe the dynamics of the total system of free field modes and the combined atom cavity system it is convenient to write the total state as

$$|\Psi(t)\rangle = b(t)|\boldsymbol{b}, 1\rangle|0_k\rangle + c(t)|\boldsymbol{c}, 0\rangle|0_k\rangle + a(t)|\boldsymbol{a}, 0\rangle|0_k\rangle + \textstyle\sum_k \xi(t)|\boldsymbol{b}, 0\rangle|1_k\rangle, \quad (7.9)$$

where the state vector $|0_k\rangle$ describes a state with zero photons in the free space mode $k$ outside the cavity. In Eq. (7.9) it is an implicit assumption that the atoms are initially all prepared in the state $|b\rangle$.

We assume that the bare cavity resonance frequency coincides with that of the atomic $|c\rangle \leftrightarrow |a\rangle$ transition and that the carrier frequency of the incoming wave packet is on resonance with the cavity. It is then a simple matter to derive the equations of motion for the amplitude functions in Eq. (7.9). In Sec. 8.2 we will use these equations to make realistic simulations of the transfer of a single photon state in the limit where adiabatic following of the dark state is not, or only barely, fulfilled. For now we will restrict the discussion to the limit where adiabatic following is fulfilled. The criterium for adiabatic following of the dark state is [102]

$$\Omega^2(t) + g^2 N \gg \max[\gamma_{\rm cav}\gamma_a,\, \gamma_a/T,\, \sqrt{\gamma_{\rm cav}/T}\gamma_a], \quad (7.10)$$

where the typical pulse duration of the incoming wave packet $T$ and the bare cavity decay rate $\gamma_{\rm cav} = \kappa_{\rm cav}^2 L/c$ have been introduced. Since the spectral width of the incoming wave packet should not exceed the width of the optical resonator, i.e., the characteristic time $T$ is larger than the bare cavity decay time $\gamma_{\rm cav}^{-1}$, the first condition is the most stringent one. Therefore in the case of one-photon storage the adiabatic following criterium becomes

$$g^2 N \gg \gamma_{\rm cav}\gamma_a. \quad (7.11)$$

For an $n$-photon Fock state the bare cavity decoherence rate is $n\gamma_{\rm cav}$ and therefore the adiabaticity condition changes to $g^2 N \gg n\gamma_{\rm cav}\gamma_a$ [1].

If the adiabatic criterium in Eq. (7.11) is fulfilled and under assumption of perfect two-photon resonance, the envelope of the outgoing wave packet becomes

$$\Phi_{\rm out}(t) = \Phi_{\rm in}(t) - \sqrt{\gamma_{\rm cav}L/c}D(t), \quad (7.12)$$

where the dark state amplitude $D(t)$ of the full state given in Eq. (7.9) is given by [102]

$$D(t) = \sqrt{\gamma_{\rm cav}c/L}\int_{t_0}^{t} d\tau \cos\theta(\tau)\Phi_{\rm in}(0,\tau) \times \exp\left[-\frac{\gamma}{2}\int_{\tau}^{t} d\tau' \cos^2\theta(\tau')\right]. \quad (7.13)$$

### 7.2.2 Impedance Matching

In the ideal storage of a photon wave packet there is no reflection of the incoming photon wave packet at the in-coupling mirror, such that after the loading of the wave packet the dark state amplitude of the atom cavity system is maximized. The dark state amplitude can be maximized by optimizing the time dependence of $\cos\theta(t)$. By imposing the condition $\Phi_{\rm out}(t) = \dot{\Phi}_{\rm out}(t) = 0$ on Eq. (7.12) we find

$$-\frac{d}{dt}\ln\cos\theta(t) + \frac{d}{dt}\ln\Phi_{\rm in}(t) = \frac{\gamma}{2}\cos^2\theta(t), \tag{7.14}$$

which corresponds to a *dynamical impedance matching condition.* The term on the right hand side of Eq. (7.14) is the effective cavity decay rate of the dark state $|D,1\rangle$, where it has been taken into account that the $|\boldsymbol{b},1\rangle$ state has an amplitude of $\cos\theta(t)$ (see Eq. (7.6)). The first term on the left hand side of Eq. (7.14) describes the transfer rate of the intra cavity photon field into the collective atomic state $|\boldsymbol{c},0\rangle$. The second term on the left hand side of Eq. (7.14) comes from the time dependence of the incoming photon field $\Phi_{\rm in}(t)$. If $\Phi_{\rm in}(t)$ is constant Eq. (7.14) just reduces to the impedance matching condition known from laser theory [115], where the internal 'loss' rate in the cavity exactly matches the in-coupling rate of the field $\Phi_{\rm in}(t)$. When this condition is fulfilled there is complete destructive interference between the directly reflected part of the incoming wave packet and the circulating field that leaks out of the cavity through the in-coupling mirror (see also Sec. 9.3).

Solving Eq. (7.14) gives

$$\cos^2\theta(t) = \frac{\Phi_{\rm in}(t)}{\gamma_{\rm cav}\int_{-\infty}^{t} dt'\Phi_{\rm in}(t')}. \tag{7.15}$$

From this solution we see that for a photon envelope function $\Phi_{\rm in}(t)$ the mixing angle $\theta \to \frac{\pi}{2}$ as $t \to \infty$, i.e., if the cavity-atom system stays in the dark state (Eq. (7.6)) through the entire loading process the excitation is purely atomic as $t \to \infty$. Releasing the stored photon can now be accomplished in a straight forward way, because reversal of the time dependence of the mixing angle $\cos\theta(t)$ at a later time, $t = t_{\rm s}$, leads to a mirror image $\Phi_{\rm out}(t)$ of the initial pulse $\Phi_{\rm in}(t)$. Note that $\cos\theta(t)$ can also be rotated back to the initial value in another way, which would yield a re-shaping of the initial pulse. In this way one can tailor the pulse shape of the released photon.

A basic storage sequence is shown in Fig. 7.3. The shape of the incoming photon wave packet envelope $\Phi_{\rm in}(t)$ has been chosen to be a hyperbolic secant (see appendix B). At the arrival of the incoming pulse ($t = 0$) the mixing angle is changed according to Eq. (7.15) such that the photon state is mapped onto the collective state of the atoms and not reflected at the in-coupling mirror. Later at $t = 25T$ the adiabatic rotation of the mixing angle is reversed and the stored photon is released into a free-field photon $\Phi_{\rm out}(t)$ with the original wave packet envelope preserved.

The product $\gamma_{\rm cav}T$ serves as a figure of merit for how the control field $\Omega(t)$ has to be shaped to fulfill the dynamical impedance matching condition. This

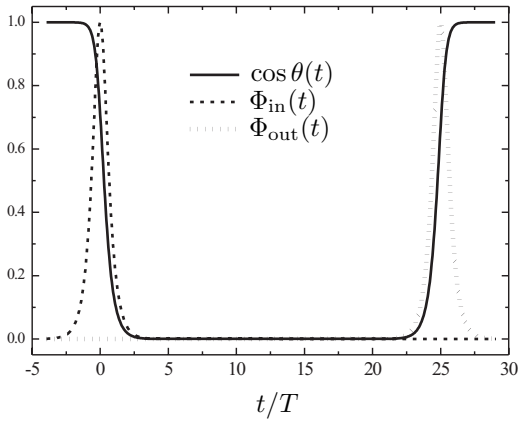


*Fig. 7.3:* Storage of hyperbolic secant input wave packet $\Phi_{\rm in}(t)$. The characteristic time $T$ is chosen such that $\gamma_{\rm cav}T = 4$.

is illustrated in figure 7.4, where the input one-photon field is a hyperbolic secant pulse. For this pulse shape the dynamical impedance matching condition requires that $\gamma_{\rm cav}T \geq 4$. We see that when $\gamma_{\rm cav}T \gtrsim 6$, which is close to the values we would like to use in our experiments, $\Omega(t)$ is initially on the order of $g\sqrt{N}$. When $\gamma_{\rm cav}T \gtrsim 4$ the initial value of $\Omega(t)$ becomes much larger than $g\sqrt{N}$. In particular the coupling field $\Omega(t) \to \infty$ as $t \to -\infty$ for the special value $\gamma_{\rm cav}T = 4$.

### 7.2.3 *Fidelity*

The success of the quantum memory depends on the ability for a certain set of experimental parameters to reproduce the incoming photon wave packet envelope $\Phi_{\rm in}(t)$, after the storage time $t_{\rm s}$, in the released photon wave packet envelope $\Phi_{\rm out}(t)$. As a quantitative measure of this reproduction success we introduce the *fidelity* of the photon storage process as

$$F = \int dt \frac{\Phi^*_{\rm out}(t)\Phi_{\rm in}(t - t_{\rm s})}{\int dt |\Phi_{\rm in}(t)|^2}. \tag{7.16}$$

In Chap. 8.2 we shall explore how the fidelity depends on the experimental parameters, when the adiabaticity condition $g^2N \gg \gamma_{\rm cav}\gamma_a$ is barely fulfilled and additional loss mechanisms in the cavity are introduced.

## 7.3 *Experimental work on light storage*

In this section the current experimental status of EIT-based light storage is described. At the end of the section we will briefly mention a recent experiment where the quantum state of a light pulse has been mapped onto an atomic sample using a completely different approach.

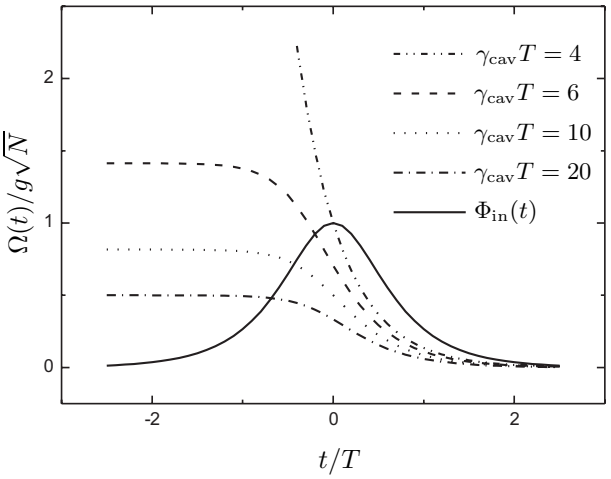


*Fig. 7.4:* Control field $\Omega(t)$ optimized according to the dynamic impedance matching condition (Eq. (7.15)) for a one-photon field with a hyperbolic secant shaped wave function envelope shown for different values of $\gamma_{\rm cav}T$. The full line shows the envelope function of the photon field.

Some of the fundamental features of EIT-based light storage of classical light pulses were demonstrated in 2001 by Liu *et al.* [4] and Phillips *et al.* [5]. In particular the experiments have shown that the pulse shape is not destroyed in the process of storing and releasing the light pulse. Phase coherence conservation in the process has also been demonstrated [116]. Here it is important to emphasize that storage of the quantum properties of the light pulses have not been demonstrated in these experiments and hence, they do not represent the realization of a true quantum memory.

For the present, the setups in the experiments on light storage have been quite different from the scheme presented in Sec. 7.1, although most of the physics underlying the light storage experiments is the same. The major difference is that in these experiments the atoms are not situated in an optical cavity. This implies that to have a sufficient collective interaction between the atoms and the light pulse the atomic sample has to be optically dense. In order to be able to store a pulse of light in an atomic sample using techniques similar to the ones we described in Sec. 7.1, the light pulse obviously needs to be contained inside the atomic sample at the instant the control field $\Omega(t)$ is adiabatically switched off. This is also the case in the light storage experiments. Even though typical light pulses in these experiments are $\sim 1$ km in vacuum, this can be accomplished since the low group velocity [117] associated with EIT leads to a spatial compression of the light pulse [109]. In 1999 Hau *et al.* [112] slowed light pulses down to group velocities of 17 m/s in an ultra cold gas of Na atoms, which meant that the pulse was localized entirely inside the atomic gas. Soon after this experiment very slow group velocities in hot atomic vapor

was also reported [118, 119].

The first experiments demonstrating dynamic reduction of the group velocity until the light pulse is brought to a halt inside the atomic medium and adiabatic following of the so-called dark state polaritons [109, 120], were reported in 2001. The atomic mediums used in these experiments are diverse. Liu *et al.* [4] use an ultra cold ($\sim \mu$K) gas of Na as the medium for light storage, obtaining storage periods of up to 1.5 ms. Phillips *et al.* [5] use a hot ($T \sim 70$–$90°$C) Rb vapor and obtain storage times of up to 0.5 ms. Even though these systems are different they exhibit nearly same properties when it comes to light storage. One common property is that the light pulse shape can be preserved in the light storage process. In Ref. [4] it is also demonstrated that a re-shaping of the pulse by an appropriate timing of the control field is possible. The coherence properties of the light storage technique has been probed in experiments on Rb vapor using a pulsed magnetic field during the storage interval to vary the Zeeman coherence in the Rb vapor in a controlled way [116]. After the light pulse was released again the phase shift was probed in an interferometric measurement. In Ref. [121] the phase coherence of light storage in Rb vapor is probed using purely optical techniques.

Storage of classical light pulses has also been accomplished in solids [122]. More specifically an optically dense crystal of Pr doped $Y_2SiO_5$ is used. Again the light storage is based on the dispersive properties of EIT, even though the EIT in solids [123] is quite different from EIT in the atomic systems [3].

Other interesting experimental effects of light storage and slow light has been observed. In Ref. [124] Bajcsy *et al.* store a light pulse using the conventional methods to map the light pulse onto the atomic coherence. They then apply forwards and backwards propagating control fields to obtain a periodic spatial variation of the light intensity, which gives a periodically modulated absorption in the atomic medium. This results in a situation where the stored light pulse is regenerated as a light field, but still not released from the atomic ensemble, because the modulation of the refractive index acts as a stack of mirrors for the stored light.

All of the light storage experiments described above are based on EIT, but there is another approach to light storage based on off-resonant interaction of a light pulse with a spin-polarized atomic sample. Due to the interaction, the atomic sample and the light pulse become entangled [125]. The light pulse is subsequently measured and a magnetic field feedback to the atoms conditioned on the measurement results in an one-to-one mapping of the initial quantum state of the light pulse onto the quantum state of the atomic sample. The mapping of light pulses containing on average eight photons per pulse onto an atomic cesium sample was achieved experimentally by Julsgaard *et al.* [126]. They proved that the mapping conserved the quantum state of the original light pulse by a subsequent measurement of the polarization state of the atomic sample. The retrieval of the original light pulse from the stored state using this method has not yet been demonstrated, but proposals to how this could be accomplished can be found in Refs. [127, 128].

# 8. LIGHT STORAGE IN ION COULOMB CRYSTALS

Trapped cold ions forming a Coulomb crystal is a good candidate for an atomic medium that can be used for storage of quantum states of light. There are several reasons why this is the case. First of all the ions are spatially confined to a small region, which means that they can stay in the interaction region during the storage and read-out processes. The ions are also well-isolated from the environment implying that the decoherence times in the states of these systems are notably long, which in turn makes it possible to achieve long storage times. The light storage fidelity may also be sensitive to Doppler shifts of the transitions involved in the scheme and it is accordingly desirable to cool the ions down to very low temperatures. This can be achieved through sympathetic cooling using another laser coolable ion species, which has cooling transition wavelengths that are different from the transition wavelengths in the ions used for the light storage.

The drawback of using ion Coulomb crystals for light storage is the low optical density in these crystals that originates from the low ion density ($\sim 10^8$ $\mathrm{cm}^{-3}$). To amend this the ion crystal needs to be placed in a moderately high finesse optical cavity as described in Chap. 7 to increase the photon-ion coupling strength. The realization of such an experimental setup involving an ion trap with an integrated optical resonator is the theme of current chapter.

## *8.1 Implementation of the quantum memory in ion Coulomb crystals*

The atomic medium we are working towards using as a storage medium for quantum states of light is a big ion Coulomb bi-crystal trapped in a linear Paul trap. The bi-crystal will consist of the two ion isotopes $^{44}Ca^+$ and $^{40}Ca^+$. As we know from the first part of this Thesis these isotopes separate spatially due to the mass dependent confinement of the ions with respect to the Paul trap axis. As a consequence the $^{40}Ca^+$ ions are situated closest to the trap axis as a cylindrical core of the crystal surrounded by the $^{44}Ca^+$ ions. Our scheme relies on using the $^{40}Ca^+$ ions as the atomic medium for light storage and using the $^{44}Ca^+$ ions for sympathetic cooling of the $^{40}Ca^+$ ions.

### *8.1.1 Quantum memory transitions*

In this section the transitions in the $^{40}Ca^+$ ion that can be used for the quantum memory $\Lambda$-level scheme are discussed in more detail. There will be a discussion

of different experimental parameters leading to this choice.

Following the discussion in Chap. 7 we situate the ion Coulomb crystal in the mode of an optical cavity to compensate for the low optical density of the ion crystal. The fidelity of the storage scheme depends critically on the quality of this optical cavity. The transmission of the in-coupling mirror has to be low enough for the cavity decay rate $\gamma_{\mathrm{cav}}$ to fulfill the requirement for adiabatic following of the dark state, i.e., $g^2N \gg \gamma_{\mathrm{cav}}\gamma_a$. At the same time unwanted cavity loss mechanisms should be much lower than this transmission loss. In the latter case the loss mechanisms originate from the non-zero transmission of the high reflective mirrors as well as the scatter or absorption losses in the mirrors. In practice this sets considerably restrictive demands to the experimental parameters, because the resonance transitions of the ions have wavelengths in the ultra violet (UV). In this wavelength range the lowest obtainable mirror reflection loss is in the range $10^{-3}$ [7], which for our purposes is very poor. At infrared wavelengths the mirror coatings are much better. Here it is possible to get mirrors with reflection losses as low as a few parts per million (ppm). In $^{40}Ca^{+}$ we can accordingly choose from three infrared transitions available at 866 nm, 854nm, and 850 nm for the signal field transition in the quantum memory adiabatic transfer scheme. From these wavelengths the 866 nm $3D_{3/2} \leftrightarrow 4P_{1/2}$ transition has been chosen for the quantum memory.

Even though the $^{40}Ca^{+}$ ions are sympathetically cooled to temperatures as low as a few tens of mK [34], there is still some Doppler broadening of the transitions due to the thermal motion of the ions. For a $\Lambda$-scheme Raman transition the Doppler broadening is divided into two classes, namely single photon Doppler broadening and the two-photon Doppler broadening. As is well known the Doppler broadening originates from a velocity dependent shift of the atomic resonances. For illustrative purposes Fig. 8.1 shows the single photon Doppler shift dependent detunings $\delta_1$ and $\delta_2$ of two laser beams with optical frequencies $\omega_1$ and $\omega_2$, respectively, and the corresponding two-photon detuning of the transition $\Delta_{2\mathrm{ph}} = \delta_1 - \delta_2$. While the width of the single photon Doppler broadening depends exclusively on the temperature of the ions this is not the case for the two-photon Doppler broadening. In the special case where the two laser beams are co-propagating, the two lower states, $|b\rangle$ and $|c\rangle$, in the $\Lambda$ level scheme are degenerate in energy and $\omega_1 = \omega_2$, we have that the two-photon detuning $\Delta_{2\mathrm{ph}} = \delta_1 - \delta_2 \equiv 0$ independent of the ion velocity. This means that there is a zero Doppler broadening of the two-photon transition. In general this is not the case. If for instance we choose to use one of the UV transitions as the coupling transition to store an infrared photon in $^{40}Ca^{+}$ a temperature of 20 mK would result in a Doppler broadening of the two-photon resonance of $\sim 4$ MHz. As the resonance width of the two-photon transition is much narrower than the width of the individual one-photon transitions ($\sim 20$ MHz) a 4 MHz broadening of the two-photon resonance would severely diminish the fidelity of the quantum memory scheme.

It is thus necessary to use a control beam transition in $^{40}Ca^{+}$ that has a similar transition wavelength as the transition which is used for storage of the signal field. Furthermore, the control beam $\Omega(t)$ needs to be co-propagating with

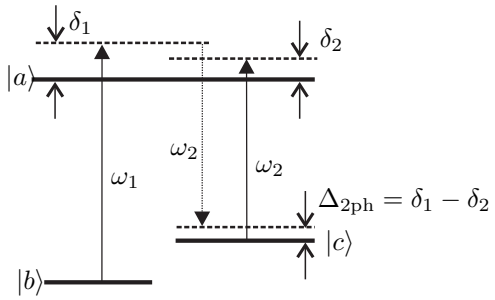


*Fig. 8.1:* Level scheme illustrating the difference between single photon detuning and two-photon detuning.

the signal field in the optical resonator at the location where the fields interact with the $^{40}Ca^{+}$ ions. To comply with these requirements the possibility of using the magnetic substates of the $3D_{3/2}$ state as the lower levels in the $\Lambda$ level scheme is attractive. More specifically, the control laser is an 866 nm $\sigma_+$-polarized laser beam that couples the $3D_{3/2}(m_j = -1/2)$ and the $4P_{1/2}(m_j = 1/2)$ states and the signal field is $\sigma_-$-polarized light resonantly coupling the $3D_{3/2}(m_j = 3/2)$ and the $4P_{1/2}(m_j = 1/2)$ states as shown in Fig. 8.2.

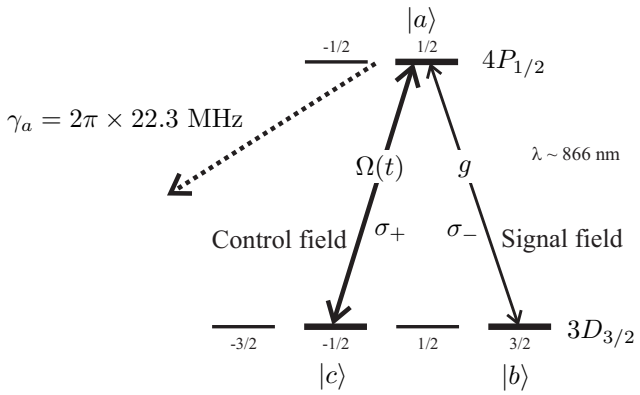


*Fig. 8.2:* The magnetic substates of the $3D_{3/2}$ state and the $4P_{1/2}$ state. The three magnetic substates constituting the $\Lambda$-system for the quantum memory are indicated by their coupling to the control field ($\sigma_+$-polarized) and the signal field ($\sigma_-$-polarized). The states $|a\rangle$, $|b\rangle$, and $|c\rangle$ refer to the level scheme discussed in Chap. 7 (see Fig. 7.1).

Apart from minimizing the two-photon Doppler broadening there is another good reason for choosing the same wavelength for the signal and control field. The infrared coating of the mirrors is very broadband ($\sim 80$ nm), so a laser beam with wavelength in the infrared would get reflected off the in-coupling mirror unless it is mode-matched and on (near) resonance with the cavity. Inasmuch as the control and signal beams have to be co-propagating the two beams can only

be coupled into the optical cavity if it is resonant with the signal beam frequency and at least near-resonant with the control beam frequency at the same time. On the other hand, the signal beam and the control beam frequencies have to be resonant with transitions in $^{40}Ca^{+}$, so in practice the only way to comply with these restrictions is to choose Zeeman substates of the same level for the lower states of the $\Lambda$ scheme, and hence equal wavelength for the signal and the control fields.

In the beginning of the storage sequence the $\sigma_{+}$-polarized control field is on and the population of the magnetic substates $m_j = -3/2$ and $m_j = -1/2$ of the $3D_{3/2}$-state are depleted. To initialize all the ions in the $|b\rangle$ state, which is the dark state condition before the signal pulse enters the cavity (see Sec. 7.1), a resonant $\pi$-polarized laser beam is also applied to deplete population in the $3D_{3/2}(m_j = 1/2)$ level. Shortly before starting the actual transfer of the signal pulse to the atomic dark state the $\pi$-polarized laser beam is switched off, such that adiabatic transfer between the $|b\rangle$ and $|c\rangle$ states can begin.

### 8.1.2 Basic setup

In Fig. 8.3 the basic configuration for the light storage in the calcium ion crystals is shown. The basic setup consists of an optical cavity for which the fundamental mode is a running wave bow-tie mode. The bow-tie cavity consists of three high reflecting mirrors and one partly transmitting in-coupling mirror with a transmission of $\mathcal{T} \sim 0.0015$. This gives an expected cavity finesse of $\mathcal{F} = 2\pi/\mathcal{T} \sim 4200$. The radius of curvature of the mirrors is 10 mm and the distance between the mirrors is $l_{\mathrm{cav}} \gtrsim 10$ mm. The distance between the two parallel arms of the mode is $\sim 400$ $\mu$m, and for the 866 nm laser light coupled into cavity the mode minimal waist, which occurs half-way between the mirrors, is $w_0 \sim 37$ $\mu$m, while the mode waist increases to $w_{\mathrm{m}} \sim 52$ $\mu$m at the mirror surfaces. The control field and the signal field are both coupled into this fundamental mode via the in-coupling mirror. The $^{40}Ca^{+}/^{44}Ca^{+}$ ion crystal is situated such that the $^{40}Ca^{+}$ cylindrical crystal core interacts only with one of the arms of the bow-tie mode.

The $^{40}Ca^{+}$ ions interact with the laser light at the location where one of the arms of the bow-tie mode is overlapping with the $^{40}Ca^{+}$ crystal core. To minimize the Doppler broadening of the $^{40}Ca^{+}$ transitions with respect to the light circulating in the bow-tie mode the orientation of the crystal is such that the micromotion of the trapped ions is perpendicular to the direction of propagation of the light interacting with the ions (see Sec. 2.1).

### 8.1.3 Adiabatic following

The criterium for adiabatic following in the quantum memory scheme is $g^2 N \gg \gamma_{\mathrm{cav}}\gamma_a$, and it is thus desirable to maximize the number $N$ of $^{40}Ca^{+}$ ions situated in the cavity mode to take advantage of the collective enhancement of the ion-photon field coupling strength. There are two ways of increasing $N$. The first is to have a high density of ions in the crystal and the second is to increase the

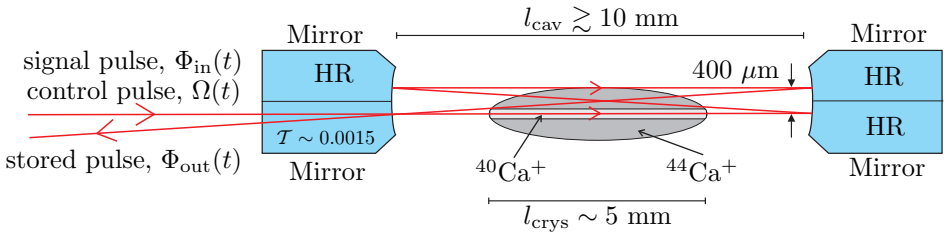


*Fig. 8.3:* Schematic of the setup for light storage in ion Coulomb crystals. The red lines illustrate the laser beam paths of the control field and the signal field. The mirrors have different coatings: high reflecting (HR) and transmitting ($\mathcal{T} \sim 0.0015$).

length of the crystal $l_{\mathrm{crys}}$ (Fig. 8.3) to maximize the spatial overlap between the ion crystal and the cavity mode. A realistic goal for the ion crystal is to have an ion density of $n = 3 \times 10^8$ cm$^{-3}$, and a crystal length of $l_{\mathrm{crys}} \sim 5$ mm. An experimental demonstration of such a crystal consisting of $\sim 5000$ $^{44}$Ca$^+$ ions and $\sim 3000$ $^{40}$Ca$^+$ ions has been performed in the linear Paul trap described in Sec. 3.1. Figure 8.4 shows a section of this crystal, where the center string of the crystal and the first shell are the cylindrical $^{40}$Ca$^+$ part of the crystal surrounded by the $^{44}$Ca$^+$ ions. The last sketch in Fig. 8.4 illustrates the $\sim 5$ mm long part of the crystal that is outside the view of the camera system.

In Appendix C we have derived an expression of the collective coupling strength of the $^{40}$Ca$^+$ ions to one photon in the cavity mode. The result is that for an ion crystal of length $l_{\mathrm{crys}} \sim 5$ mm and density $n \sim 3 \times 10^8$ cm$^{-3}$, $N \sim 3200$ $^{40}$Ca$^+$ ions will interact with the cavity mode and the collective coupling strength is $g\sqrt{N} \sim 2\pi \times 11.6$ MHz. To simplify the model it was assumed in the Hamiltonian introduced in Chap. 7 (see Eq. (7.2)) that all the ions couple equally to the cavity mode. As seen in Appendix C the individual coupling strengths are actually not equal for all ions, because the ions are situated at different positions in the cavity mode. These individual coupling strengths have been accounted for in the calculation of $g\sqrt{N}$ by an integration over the mode volume of the cavity mode, but not in the Hamiltonian. The real world experimental conditions are thus somewhat more complex than the model leading to the rate equations which are used in the next section to calculate the fidelity of the light storage.

## 8.2 Simulations on storage of a single photon

In the adiabatic limit, where the condition $g^2 N \gg \gamma_{\mathrm{cav}}\gamma_a$ is fulfilled, the fidelity is $F$ approaches 1. Experimentally it is hard to fulfill the adiabatic following strictly, because experimental conditions restrict the parameters. The decay rate out of the excited state $\gamma_a$ is fixed once the transition for the light storage has been chosen. The coupling parameter $g$ also depends on the chosen transition, but here there is also a dependence of the cavity mode volume $V$ (see Eq. (7.1)). The number of ions situated in the cavity mode $N$ is limited by the spatial

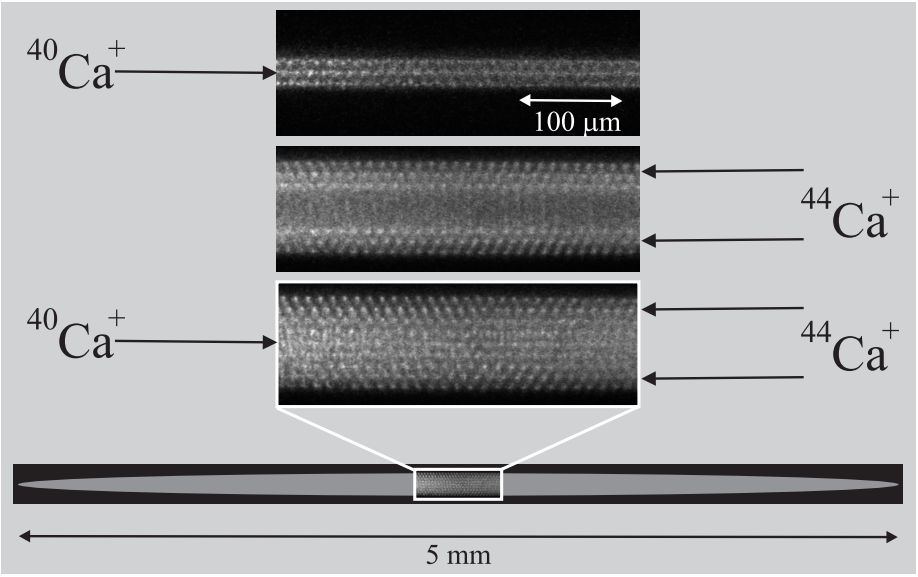


*Fig. 8.4:* Section of a bi-crystal consisting of $\sim 3000$ $^{40}Ca^{+}$ and $\sim 5000$ $^{44}Ca^{+}$ which is approximately the size needed for the quantum memory ion Coulomb crystals. Laser cooling is applied to $^{40}Ca^{+}$ (first insert), $^{44}Ca^{+}$ (second insert), and both ion isotopes (third insert). The drawing indicates the actual size of the crystal from which the crystal section is taken.

overlap of the ion Coulomb crystal and the cavity mode as well as the density of ions in the crystal. When these parameters have been fixed by the experimental conditions the final parameter to consider is the cavity decay rate $\gamma_{\text{cav}}$.

In general we can write the total cavity decay rate as

$$\gamma_{\text{tot}} = \gamma_{\text{cav}} + \gamma_{\text{loss}}, \tag{8.1}$$

where $\gamma_{\text{cav}} \equiv \frac{\mathcal{T}c}{4l_{\text{cav}}}$ is the cavity decay rate originating from the transmission of the in-coupling mirror and $\gamma_{\text{loss}}$ is the decay introduced by absorption and scattering losses on the mirror surfaces of the cavity. Ideally $\gamma_{\text{loss}}$ should be zero, because the fidelity of the light storage is directly influenced by these loss mechanisms, but in real world experiments there are always these unwanted dissipative effects in a cavity. A condition that certainly should be fulfilled to have a fidelity of $F \simeq 1$ is $\gamma_{\text{cav}} \gg \gamma_{\text{loss}}$. This condition follows from the simple reasoning that in order to preserve a stored photon field during the photon release process it needs to be favorable for the photon to leak out of the in-coupling mirror ($\gamma_{\text{cav}}$) rather than dissipate through the other decay channel ($\gamma_{\text{loss}}$). The minimum allowable length of the photon wave packet also depends on the cavity decay rate $\gamma_{\text{cav}}$. In the specific example of a hyperbolic secant pulse (Sec. 7.2.2) the condition for photon transfer is that $\gamma_{\text{cav}} T \geq 4$, where $T$ is the characteristic length of the secant pulse (see appendix B). In the following we

shall explore how the storage fidelity depends on the parameters $\gamma_{\rm cav}$ and $\gamma_{\rm loss}$ by numerical simulations of the light storage based on the model introduced in Chap. 7. The main purpose of the simulations is to find the in-coupling mirror transmission $\mathcal{T}$, or equivalently $\gamma_{\rm cav}$, for which the storage fidelity in optimized when cavity losses are taken into account. The simulations were carried out in collaboration with Claudia Mewes and Michael Fleischhauer.

Under the condition of perfect two-photon resonance, the equations of motion for the amplitude functions of the full state vector $|\Phi(t)\rangle$ defined in Eq. (7.9) are given by

$$\begin{aligned}
\dot{a}(t) &= -(\gamma_a/2) - ig\sqrt{N}b(t) - i\Omega(t)c(t), \\
\dot{b}(t) &= -ig\sqrt{N}a(t) - i\kappa_{\rm cav}\Phi_{\rm in}(t) - (\gamma_{\rm cav}/2)b(t) - (\gamma_{\rm loss}/2)b(t), \\
\dot{c}(t) &= -i\Omega(t)a(t),
\end{aligned} \tag{8.2}$$

which are solved numerically in the simulations. The envelope of the outgoing wave packet is found from

$$\Phi_{\rm out}(t) = \Phi_{\rm in}(t) - i\frac{\gamma_{\rm cav}}{\kappa_{\rm cav}}b(t), \tag{8.3}$$

and subsequently the fidelity of the sequence can be calculated using Eq. (7.16).

The simulations are based on the single photon storage of a hyperbolic secant pulse (see appendix B) $\Phi_{\rm in}(t)$, where we have chosen the pulse length $T$ such that $\gamma_{\rm cav}T = 4$. At $t = 0$ the pulse enters the cavity and the classical control field $\Omega(t)$ is changed according to Eq. (7.15). At $t = t_{\rm s}$ the time evolution of the control field is reversed to release the stored photon wave packet.

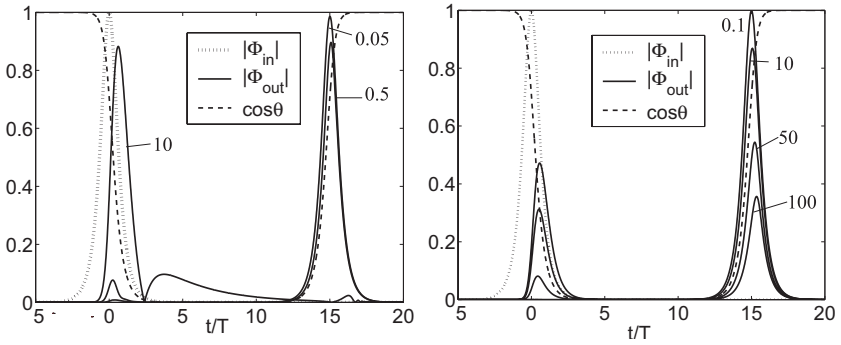


(a) $\gamma_{\rm cav}/g\sqrt{N} = [0.05, 0.5, 10]$ (b) $\gamma_a/g\sqrt{N} = [0.1, 10, 50, 100]$

*Fig. 8.5:* Output $|\Phi_{\rm out}(t)|$ wave packet envelopes for a hyperbolic secant input wave packet $|\Phi_{\rm in}(t)|$ and optimized $\cos\theta(t)$. In (a) the cavity decay rate $\gamma_{\rm cav}$ is varied and the parameters are $\gamma_{\rm cav}/g\sqrt{N} = [0.05, 0.5, 10]$, $\gamma_a/g\sqrt{N} = 1$, and $\gamma_{\rm loss} = 0$. In (b) the atomic excited state decay rate $\gamma_a$ is varied and the parameters are $\gamma_a/g\sqrt{N} = [0.1, 10, 50, 100]$, $\gamma_{\rm cav}/g\sqrt{N} = 0.05$, and $\gamma_{\rm loss} = 0$. Further details are described in the text.

Figure 8.5(a) and Fig. 8.5(b) show the output field envelopes for different parameter sets of the decay rates $\gamma_a$ and $\gamma_{\mathrm{cav}}$. The dissipative loss decay rate is set to $\gamma_{\mathrm{loss}} = 0$ and the storage time is $t_{\mathrm{s}} = 15T$. It is seen that the output wave packet preserves the shape and amplitude of the input wave packet when the adiabaticity condition $g\sqrt{N} \gg \gamma_a\gamma_{\mathrm{cav}}$ is fulfilled. When the condition is barely or not fulfilled the input field $\Phi_{\mathrm{in}}$ is partly reflected on the arrival of the pulse ($t \sim 0$). A closer look on the output wave packet reveals that apart from decreasing the amplitude of the output wave packet the non-adiabatic effects also tend to shift the effective storage time. This can be corrected by replacing the storage time $t_{\mathrm{s}}$ by an effective storage time $t_{\mathrm{s,eff}}$ that maximizes the overlap integral (Eq. (7.16)) used in the calculation of the fidelity.

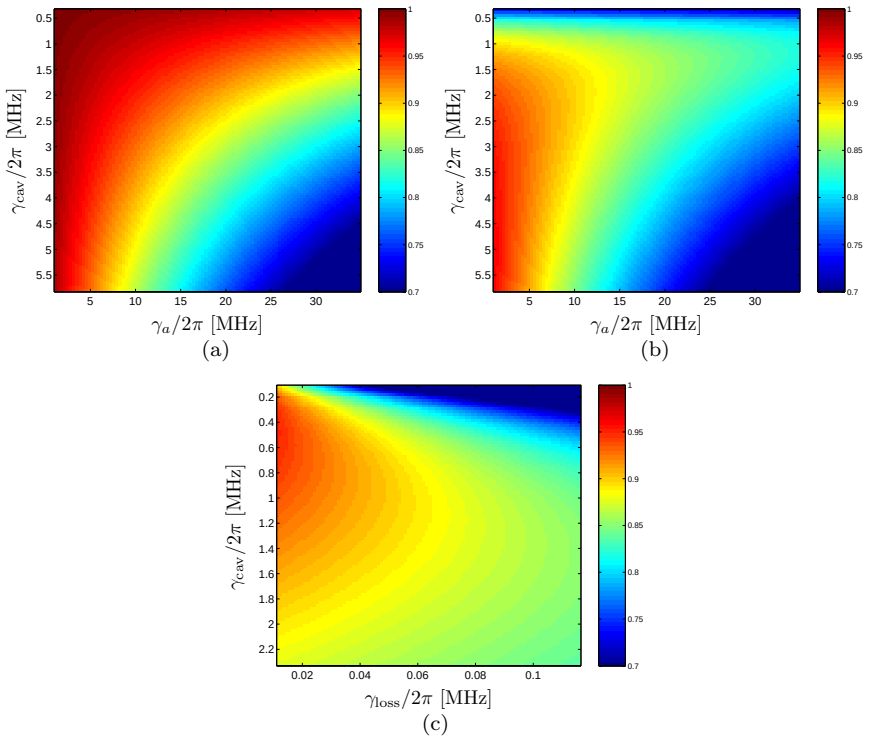


*Fig. 8.6:* Color maps of the fidelity $F$. In all the simulations the collective coupling strength is $g\sqrt{N} = 2\pi\times 11.6$ MHz. The pulse is released after $t_{\mathrm{s}} = 15T$, where $T = 4\gamma_{\mathrm{cav}}^{-1}$. Graph (a) shows $(\gamma_a, \gamma_{\mathrm{cav}}, F)$, while $\gamma_{\mathrm{loss}}$ is set to zero. Graph (b) also shows $(\gamma_a, \gamma_{\mathrm{cav}}, F)$, but here a dissipative loss of $\gamma_{\mathrm{loss}} = 2\pi \times 120$ kHz is included. Graph (c) shows $(\gamma_{\mathrm{loss}}, \gamma_{\mathrm{cav}}, F)$ for the excited state decay rate $\gamma_a = 2\pi \times 22.3$ MHz.

Figure 8.6 shows color maps of the calculated fidelity for different decay rate parameters. The fidelity has been calculated using the effective storage time $t_{\mathrm{s,eff}}$ rather than the storage time $t_{\mathrm{s}}$. In Fig. 8.6(a) the dissipative decay rate

$\gamma_{\rm loss} = 0$, so the only loss of fidelity is due to non-adiabatic effects. In this idealized case we see that for a given atomic excited state decay rate $\gamma_a$ the fidelity can in principle be increased at will by decreasing the cavity decay rate $\gamma_{\rm cav}$. A small cavity decay rate implies that the cavity finesse is high which in turn makes the experiment more elaborate. Furthermore, the photon wave packet length still needs to fulfill the adiabaticity criterium $T \geq 4\gamma_{\rm cav}^{-1}$, which could also limit the range of $\gamma_{\rm cav}$ in practice.

In Fig. 8.6(b) the fidelity is plotted in the situation where a dissipative loss of $\gamma_{\rm loss} \sim 2\pi \times 120$ kHz is included. An obvious conclusion from this plot is that $\gamma_{\rm cav} \gg \gamma_{\rm loss}$ is indeed a requirement for a high fidelity storage process. In the last graph, Fig. 8.6(c), the fidelity dependence on the loss decay rate $\gamma_{\rm loss}$ has been plotted. The range of $\gamma_{\rm loss}$ has been chosen as representative for what is expected in the experiment. The excited state decay rate is $\gamma_a = 2\pi \times 22.3$ MHz. This plot illustrates that there is a dependence of the fidelity on $\gamma_{\rm loss}$ and that it is advantageous to choose $\gamma_{\rm cav} \gtrsim 2\pi \times 0.5$ MHz. At higher values of $\gamma_{\rm cav}$ the adiabaticity criterium $g^2 N \gg \gamma_{\rm cav}\gamma_a$ is violated and the fidelity decreases.

## 8.3 The bow-tie mode cavity

In Sec. 8.1.2 the basic optical resonator setup was introduced. Now we shall discuss the possibility of obtaining a running wave bow-tie mode cavity based on spherical mirrors. It should be mentioned that Hemmerich *et al.* [129] have designed a small high finesse running wave resonator. This resonator unfortunately suffers from a large mode volume that would make it unsuited for our experiment.

The basic geometry of the bow-tie mode resonator is shown in Fig. 8.7. Light circulating in the bow-tie mode is reflected at the points $a$, $b$, $c$, and $d$. The two lengths $L_1$ and $L_2$ are the distances $|ab|$ and $|bc|$, respectively. The distance between the parallel arms of the mode is denoted by $x$ and as was mentioned in Sec. 8.1.2 the aim is to have $x \sim 400$ $\mu$m. The mirrors have a radius of curvature of $\mathcal{R} = 10$ mm.

We shall now examine the stability of the resonator by the use of ray transfer matrices ($ABCD$-matrices). A general treatment of this subject can be found in Kogelnik and Li [130]. The resonator stability is crucial when considering Gaussian beam modes in the resonator as these modes only apply to stable resonators. To describe the cavity round trip ray propagation in the bow-tie mode of the resonator it is sufficient to calculate the $ABCD$-matrix for the propagation $a \rightarrow b \rightarrow c$, because it is equivalent to the $ABCD$-matrix for the $c \rightarrow d \rightarrow a$ propagation. The ray propagation matrix for $a \rightarrow b \rightarrow c$ is given by

$$\begin{bmatrix} A & B \\ C & D \end{bmatrix} = \begin{bmatrix} 1 - 2\frac{L_2}{\mathcal{R}} & L_1 + L_2 - 2\frac{L_1 L_2}{\mathcal{R}} \\ -4\frac{1}{\mathcal{R}} + 4\frac{L_2}{\mathcal{R}^2} & 1 - 4\frac{L_1}{\mathcal{R}} - 2\frac{L_2}{\mathcal{R}} + 4\frac{L_1 L_2}{\mathcal{R}^2} \end{bmatrix}. \tag{8.4}$$

A necessary and sufficient condition for stability of periodic sequences of an $ABCD$-matrix is that $\frac{1}{2}|A+D| \leq 1$, which for our ray transfer matrix (Eq. (8.4)) gives the condition

$$0 \leq (1 - L_1/\mathcal{R})(1 - L_2/\mathcal{R}) \leq 1 \tag{8.5}$$

on the lengths $L_1$ and $L_2$.

In the case where the mirror radius of curvature equals the distance between the mirrors the resonator is said to be confocal. In such a geometry a bow-tie ray is supported. The resonator is however unstable in this situation because $L_1 < \mathcal{R}$ and $L_2 > \mathcal{R}$ and this violates Eq. (8.5). In order to meet the criterium we thus choose lengths $L_1 > \mathcal{R}$ and $L_2 > \mathcal{R}$. The graph in Fig. 8.7 (b) shows how the minimal waists of the Gaussian bow-tie mode ($\lambda = 866$ nm, $x = 400$ $\mu$m) depends on $L_1$. The minimal waists have been calculated by using the $ABCD$-law to propagate the $q$ parameter of the Gaussian beam (see Ref. [131]) and assuming that the $q$-parameter is unchanged after one round trip in the resonator. It is seen that the waist at the point $\alpha$ defined in Fig. 8.7(a) goes to zero, while the waist at the point $\beta$ diverges as the length of the cavity, approaches the unstable resonator geometry. The dotted graph in Fig. 8.7 (b) is the minimal waist in a standing wave resonator geometry ($x = 0$, $L_1 = L_2$). For the real trap setup the cavity length of 10.7 mm has been chosen. At this cavity length the minimal waists of the bow-tie mode are $\sim 37$ $\mu$m.

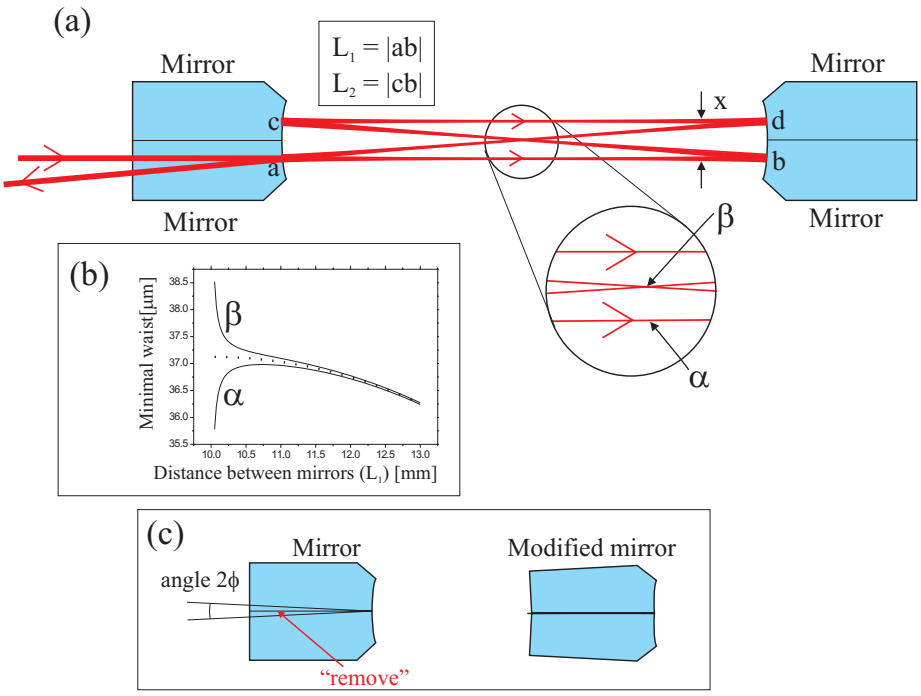


*Fig. 8.7:* (a) The geometry of the bow-tie mode resonator. (b) Minimal waist as a function of the cavity length $L_1$ at the points $\alpha$ and $\beta$ defined in Fig. 8.7(a) The dotted graph is the minimal waist for a standing wave cavity of length $L_1$ and mirror radius of curvature of 10 mm. (c) The modification of the mirror substrates needed for a bow-tie ray supporting geometry.

A simple geometric ray tracing argument reveals that conventional spherical

mirrors fail to support a bow-tie ray unless the resonator is in a confocal geometry. In the light of the previous discussion we need a non-confocal geometry in order to have stable oscillation. In order to obtain a bow-tie mode in the non-confocal geometry the mirrors need to be modified. We envision this is done by removing a little more than half of a mirror substrate under an angle $\phi$ defined in Fig. 8.7(c). Then taking two such half mirror substrates and set them together tilted at the angle $2\phi$. The angle $\phi$ required for a bow-tie mode cavity can be calculated using the formula

$$\phi = \arcsin \frac{x}{2\mathcal{R}} - \frac{1}{2} \arctan \frac{x}{L_1}. \tag{8.6}$$

Inserting $x \sim 400$ $\mu$m, $L_1 \sim 10.7$ mm, and $\mathcal{R} = 10$ mm in Eq. (8.6) we find the angle $\phi \sim 0.076°$.

The manufacturing of the bow-tie cavity still needs to be done. In the present setup we have a standing wave near confocal resonator geometry with spherical mirrors. Further details about this resonator geometry will be discussed in Sec. 9.3.2.

## 8.4 Linear Paul trap with integrated optical resonator

This section describes the design considerations concerning the implementation of an optical resonator into a linear Paul trap. Some of the challenges we have encountered in this design phase are known from the relatively young field in quantum optics concerning one ion coupled to the mode of a high finesse optical cavity. The significant progress in this field is mainly due to the groups of H. Walther [7, 132] and R. Blatt [133–135], which both work with a single $Ca^+$ ion coupled to the mode of an optical resonator. There are some advantages of using an ion instead of neutral atoms coupled to the cavity mode. To mention the most important ones the ions have long trapping times and a high degree of localization, which for instance can be used to probe the standing wave pattern of an optical cavity [132]. On the other hand, introducing an optical cavity in the vicinity of the ion trap changes the electric trapping fields produced by the Paul trap electrodes. With the present ion trap technology this fact actually prohibits the cavity mode volume from getting small enough that a strong coupling between the ion and the cavity mode can be reached.

In the quantum memory setup we are going to trap big ion crystals in between the mirrors using a linear Paul trap. The ions in these big ion crystals are not stationary but move under the influence of the harmonically varying rf-field that gives the radial confinement of the ions. This micromotion which was introduced in Sec. 2.1 is in an ideal linear Paul trap perpendicular to the trap axis. Because we want to minimize the Doppler broadening of the storage transitions (see Fig. 8.2) we have chosen to have the control and signal light propagate along the trap axis in the interaction region, i.e., the light propagates perpendicular to the micromotion. But in the real trap setup the fields from the electrodes are perturbed by the presence of the cavity mirrors.

The dielectric constant of fused silica which is used for the mirror substrates is $\epsilon = 3.78\epsilon_0$ for static electric fields and harmonically varying electric fields with frequencies in the $\sim$ MHz range [136]. The electric field lines from the electrodes are hence strongly attracted by the mirror substrates. The distortion of electric field lines introduces an unwanted component of the micromotion towards the mirrors, i.e., an axial component of the micromotion. This axial component is unwanted as it Doppler broadens the transitions used for the light storage. Furthermore the laser cooling of the $^{44}Ca^{+}$ ions is affected by axial micromotion and in the worst case it prohibits crystallization of the ion plasma.

### *8.4.1 Trap dimensions*

In order to design the Paul trap electrodes and the shape of the mirror substrates the 3D partial differential equation solver 'FlexPDE' was used. The program enables us to define the geometry of the linear Paul trap and the mirrors in 3D, and to solve the Laplace equation for the potential $V$ when the potentials on the Paul trap electrodes have been specified.

In the design of the linear Paul trap we aim at getting as close to a harmonic potential as possible in the region where the ions are located. In order to minimize anharmonicity in the radial direction the potential is simulated in the situation where only the rf-voltage $U_{\mathrm{rf}}$ (see Eq. (2.1)) has been applied and the electrode radius is varied. According to Ref. [137] the best approximation to a harmonic quadrupole potential is obtained when the electrode radius is $r_e \sim 1.147 r_0$, where $r_0$ is the inter electrode inscribed radius (see Fig. 2.1). The simulations indicate that this is also the case when the mirror substrates are present, and we have thus chosen to keep this ratio. The center-electrode length $2z_0$ determines the shape of the static potential $U_{\mathrm{ec}}(z)$ that confines the ions axially.

In Fig. 8.9 the axial potential for different center-electrode lengths is shown. The trap dimensions used in the simulation are given in the figure caption. As seen from the axial potential curve plotted in Fig. 8.9 will the presence of the mirrors act to confine the trapped ions stronger in the axial direction. The least squares fits of the axial potential reveal that a center-electrode length of $2z_0 = 5$ mm gives an axial potential with a very small deviation from a harmonic potential in the region $|z| < 2.5$ mm which is where the ion crystal is located. This is in accordance with the findings of C. E. Brodersen [138], who found that the length of the center-electrode should be $2z_0 \sim 2r_0$ in order to obtain a harmonic potential in the ordinary Paul trap design where no mirror substrates are included.

In the design of the cavity mirrors trap it is important to consider what shape of the mirrors will induce the least micromotion along the $z$-axis. Here a small argument may lead us in the right direction. Suppose we have four infinitely long electrode rods in a quadrupole configuration directed along the $z$-axis. Adding voltages to the electrodes will induce an $E$-field that is everywhere perpendicular to the $z$-axis. Now, filling space uniformly with a dielectric for $z < 0$ will not change the $E$-field in any point in space, because this $E$-field fulfills the necessary

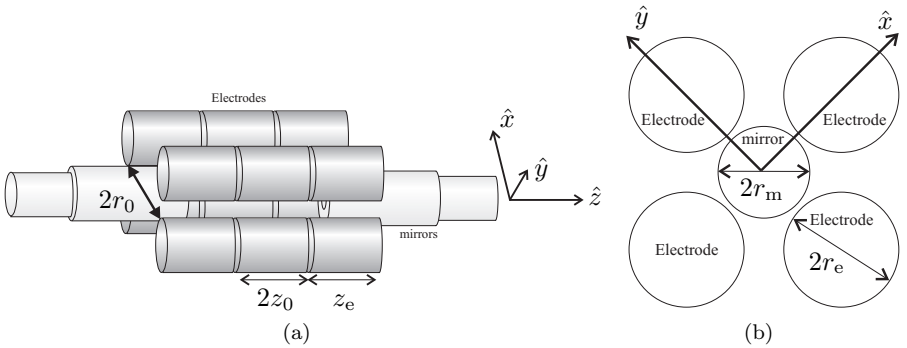


*Fig. 8.8:* (a) Sketch of linear Paul trap with integrated mirrors. (b) End-view of the trap.

boundary conditions at the dielectric vacuum interface [139]. The same line of reasoning leads to the conclusion that in the real trap setup the end of the mirror substrates should be flat and extend as far as possible to the electrodes. Numerical simulations for different mirror radiuses $r_m$ reveal that the induced axial micromotion becomes more than a factor of 100 higher when the mirror radius is scaled from $r_m = r_0$ to $r_m = \frac{1}{2}r_0$ which confirms this assertion.

| | |
|---|---|
| Mirror radius: | $r_m = 2.075$ mm |
| Electrode radius: | $r_e = 2.6$ mm |
| Electrode inscribed radius: | $r_0 = 2.35$ mm |
| Center-electrode length | $2z_0 = 5$ mm |
| End-cap electrode length | $z_{ec} = 5$ mm |
| rf-frequency: | $\Omega_{rf} = 2\pi \times 4.25$ MHz |
| Axial geometrical constant: | $\eta = 0.342$ |
| $a$-parameter($^{40}Ca^+$): | $a = -0.74 \times 10^{-3} U_{ec}$ [Volt] |
| $q$-parameter($^{40}Ca^+$): | $q = 1.23 \times 10^{-3} U_{rf}$ [Volt] |

*Tab. 8.1:* Reference table of the trap-parameters. The trap dimensions are depicted in Fig. 8.8, and the $a$ and $q$ parameters are treated in Sec. 2.1.

The dimensions of the trap and the mirror substrate are presented in Table 8.1. They have been chosen such that we can fulfill the requirement that the Coulomb crystal ion density is $n_0 = 3 \times 10^8$ cm$^{-3}$ for a reasonable amplitude of the rf-voltage. Using the parameters from Table 8.1 and Eq. (C.1) we see that to obtain this ion density for $^{40}Ca^+$ an rf-voltage of $U_{rf} \sim 220$ V is needed, which is technically feasible.

### *8.4.2 Mirror off-set*

As a prerequisite for the geometry of the ion trap and integrated bow-tie mode cavity the $^{40}Ca^+$ ion Coulomb crystal core needs to be located at the position

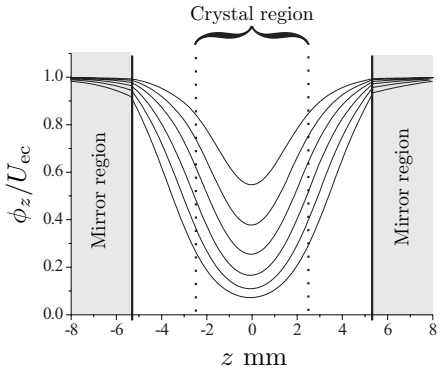


*Fig. 8.9:* Axial potentials along the center-axis when $U_{\rm rf} = 0$ and $U_{\rm ec} \neq 0$ for the center-electrode lengths [2,3,4,5,6,7] mm starting from top graph. The mirror end-faces are indicated by the full lines and the ion Coulomb crystal region is indicated by dotted lines. The electrode radius is $r_e = 2.6$ mm and the electrode inscribed radius is $r_0 = 2.35$ mm. The cylindrically shaped mirrors have radius $r_{\rm m} = 2.0$ mm and the distance between the mirrors is $l_{\rm cav} = 10$ mm (see Fig. 8.8).

with the least micromotion, which is on the Paul trap axis. This implies that in order to get overlap between the cavity mode and the ion crystal (see Fig. 8.3) a 200 $\mu$m radial displacement of the bow-tie mode cavity relative to the Paul trap axis may be needed. Unfortunately this displacement introduce unwanted micromotion along the $z$-axis.

When the mirror symmetry axis is centered on the linear Paul trap axis the geometrical symmetry makes the induced axial micromotion near the Paul trap axis so small that it is hard to quantify in the numerical simulations. If we make a small radial off-set of the mirrors this is no longer the case. We shall now investigate the consequences of axial mirror displacements from numerical simulations of the rf-potential, which is used to give an estimate of the velocity amplitude of the axial micromotion. The directions $\hat{x}$ and $\hat{y}$ used in this discussion are defined in Fig. 8.8.

In Fig. 8.10 the velocity amplitude of the axial micromotion component for a $^{40}Ca^{+}$ ion is shown as a function of the position in the $\hat{y}$-direction, when both mirrors have been displaced 200 $\mu$m in the directions $\hat{x}$ and $\frac{\hat{x}+\hat{y}}{\sqrt{2}}$. This velocity amplitude was estimated from electric field simulations in FlexPDE. From this graph we can deduce that the size of the axial micromotion is really dependent on the displacement direction. Mirror displacement along the $\hat{x}$-direction clearly introduces much bigger axial micromotion than the displacement along the $\frac{\hat{x}+\hat{y}}{\sqrt{2}}$-direction. For the 200 $\mu$m displacement in the $\hat{x}$-direction the axial micromotion velocities are $v_z \sim 30$ m/s for ions at the position $z = 2.5$ mm. Even though this has the biggest effect on the ions that are closest to the mirrors ($z \sim 2.5$ mm) the other ions are moving with comparable velocities. In terms of Doppler cooling

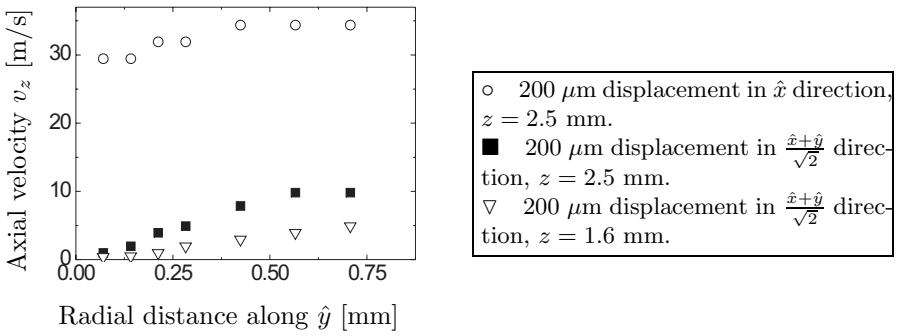


*Fig. 8.10:* Axial micromotion velocity amplitude of the ion $v_z$ as a function of the distance from the Paul trap axis along the direction $\hat{y}$ when the mirrors are translated 200 $\mu$m along the $\hat{x}$ and $\frac{\hat{x}+\hat{y}}{\sqrt{2}}$ directions. The unit vectors $\hat{x}$ and $\hat{y}$ have been defined in Fig. 8.8(b).

velocities of this magnitude are critical and should be avoided. A displacement of 200 $\mu$m in the $\frac{\hat{x}+\hat{y}}{\sqrt{2}}$-direction has, according to the simulations, less critical influence on the axial micromotion. This is especially the case for the ions at distances $r \lesssim 200$ $\mu$m from the trap axis. These ions move at axial velocities of $v_z \sim 1$ m/s, which is sufficiently low for cooling below the critical temperature for crystallization.

The smaller axial micromotion for a mirror displacement in the $\hat{x}$-direction is expected for simple symmetry reasons. Imagine that we have the mirrors centered in the linear Paul trap and only applied the quadrupole voltages at the four electrode rods. Then the electric potential is constant in the plane spanned by the $\frac{\hat{x}+\hat{y}}{\sqrt{2}}$ and the $\hat{z}$ unit vectors and located halfway between the Paul trap electrodes. Due to symmetry this is still valid if the mirrors are displaced along the $\frac{\hat{x}+\hat{y}}{\sqrt{2}}$ direction. If the electric potential is constant in this plane there is no electric field component in this plane, i.e., the micromotion associated with the oscillating electric field is zero in this plane. Therefore it is expected that $v_z = 0$ m/s in this plane as is confirmed by the simulation shown in Fig. 8.10.

## *8.5 Magnetic field*

The magnetic field in the region of the $^{40}Ca^+$ ions has a crucial influence on whether or not light storage in the $^{40}Ca^+$ ions is possible. The obvious reason for this is that we use the magnetic substates in the $^{40}Ca^+$ ions for light storage. In the present section the influence of magnetic fields present in the experiment is discussed.

Two physical properties that have direct consequences for the outcome of the experiment depend on the magnetic field.

- The first property is the *Zeeman shift* of the magnetic substates of the $3D_{3/2}$ state. Two of these magnetic substates are coupled by the 866 nm control laser and signal laser pulse in a $\Lambda$-configuration (see Fig. 8.2) under the condition of two-photon resonance. Zeeman shifts of the substates thus imply that a detuning of the control laser frequency with respect to the carrier frequency of the signal pulse is necessary, which in turn means that the control and signal pulse cannot be on resonance with the cavity simultaneously. For a Zeeman shift which is much larger than the cavity resonance width in-coupling of the control laser into the cavity mode is impossible, when the two photon resonance condition is fulfilled.

- The second property is the *Larmor precession* of the ions around the direction of the magnetic field. This will cause a fast decoherence of the stored state if the magnetic field is perpendicular to the quantization axis of the control and signal light.

These two properties make it important to minimize and control the magnetic field at the location of the $^{40}Ca^{+}$ ions.

The different sources of magnetic fields are the earth field, currents in the wires connected to the trap electrodes, and magnetic materials in the vicinity of the trapping region. The latter magnetic field source has been minimized by careful selection of non-magnetic materials for the Paul trap construction, the vacuum chamber, and the laser table. This will be described in Chap. 9.

The earth field, which is on the order of one gauss, is compensated by coils external to the vacuum chamber giving a homogeneous field at the location of the $^{40}Ca^{+}$ ions. The field in the vacuum chamber emanating from various local sources of magnetic fields was measured to have a gradient $|\nabla|B|| \lesssim 0.1$ mG/mm.

The currents in the wires connected to the trap electrode can be estimated from the capacitance of the linear Paul trap, which is on the order of $\sim$ pF. For an rf-voltage of $U_{\mathrm{rf}} \sim 200$ V this gives rise to time varying currents with an amplitude of $\sim 1$ mA. The magnitude of the $B$-field induced by these currents is $\lesssim 0.5$ mG. The magnetic field gradient from these currents is expected to be $\sim 0.1$ mG/mm.

It is therefore possible to reduce stray magnetic fields in the region of the $^{40}Ca^{+}$ ions to $\sim$ 1 mG. This corresponds to a Larmor frequency of 1 kHz that would determine the decoherence rate of the atomic dark state, which is a considerably faster decoherence than the decoherence set by the lifetime of $\sim 1$ s of the $3D_{3/2}$-state. In order to make the decoherence rate smaller a bias magnetic field directed along the propagation axis of the control laser and the signal pulse ($\hat{z}$-axis) can be added which with certainty makes the $\hat{z}$-axis the axis of Larmor precession. This bias field can be fairly large compared to the stray field in the trap, because the only requirement is that the Zeeman shift due to the bias field is not too large compared to the cavity width as mentioned in the beginning of this section. The relative Zeeman shift of the $m_j = -1/2$ and $m_j = 3/2$ substates in the $3D_{3/2}$ state is $\Delta E = 2\pi \times 2.2$ MHz/G and the cavity resonance width is $\gamma_{\mathrm{cav}} = 2\pi \times 1.7$ MHz, which means that a bias field of up to

$\sim 1$ G can be applied before the in-coupling of the control field is significantly reduced.

## 8.6 Cavity locking scheme

In order to fulfill the criteria that the trap cavity is resonant with the carrier frequency of the memory pulse the length of the trap cavity needs to be stabilized to some external reference. Certain measures have been taken at the trap table to minimize the acoustic noise at the cavity, such as having a rigid table construction with a noise-dampening honeycomb structure inside the table. Despite these precautions active cavity stabilization during the adiabatic transfer of the memory pulse seems to be necessary as the cavity length has to be well defined on the length scale determined by the ratio between the wavelength of the light ($\lambda \sim 866$ nm) and the finesse ($\mathcal{F} \sim 4200$), i.e., $\sim 0.2$ nm.

For the active stabilization we need locking laser for the cavity. The laser needs to be stable in frequency and it must not interact with the $^{40}Ca^{+}$ ions. In the following discussion the different aspects of choosing the appropriate locking laser setup is covered.

It is important that the locking laser is stable on a long term as the experiments typically take hours to complete. Ideally the cavity has to stay exactly on resonance with the 866 nm transition in $^{40}Ca^{+}$ at all times. We could consider using an absolute frequency reference for the locking laser as for instance an atomic transition. A problem arises, however, when we take into consideration that the locking laser should be tunable with respect to the atomic transition in order to set the trap cavity on resonance with the 866 nm transition in $^{40}Ca^{+}$. Tuning the locking laser with respect to the atomic transition is possible by introducing an AOM or an EOM to induce sidebands, but in order to be able to tune to all frequencies in a free spectral range of the cavity the tuning range of the AOM or the EOM system has to be a few GHz, which is not feasible.

To overcome this problem a temperature stabilized cavity with a free spectral range of $\sim 600$ MHz is used as a frequency reference instead, which gives a span of frequencies that the locking laser can be tuned to. The idea is to use the same temperature stabilized cavity for the locking laser as we use for the 866 nm memory laser. By doing so the two lasers are fixed relative to each other, which in turn implies that the trap cavity length is fixed to the 866 nm laser which needs to be on resonance with the cavity. A drawback of this scheme is the drift of the temperature stabilized cavities, which mainly cause the 866 nm laser to drift away from the atomic resonance of $^{40}Ca^{+}$. This drift has been measured to be maximally 1 MHz/h and only $\sim 5$ MHz during a whole day [45] for the temperature stabilized cavity we intend to use (see also Sec. 3.4.4). A similar setup for the locking laser is used by the ion trap group in Innsbruck [134]. In this setup an ultra-stable cavity is used as a reference [140].

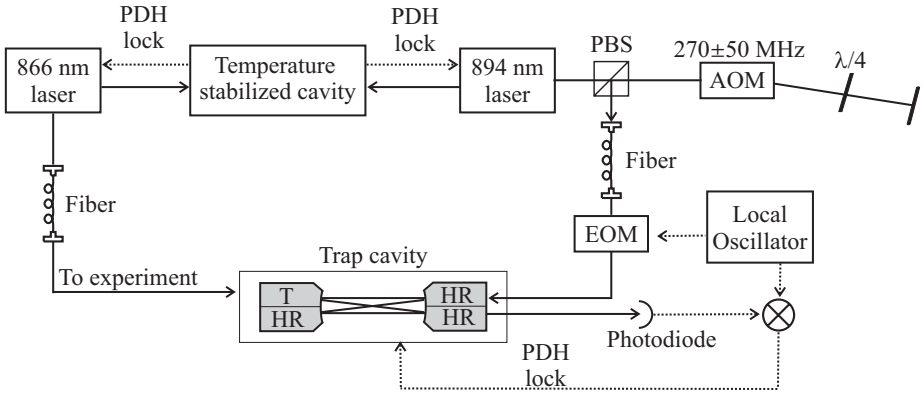


*Fig. 8.11:* The basic layout of the trap cavity locking scheme during the experiments. Solid lines are laser beam paths and dashed lines are signal paths. PDH lock: Pound-Drever-Hall lock, PBS: Polarizing Beam Splitter, T: Transmitting mirror, HR: High Reflecting mirror.

### *8.6.1 Scheme description*

A conceptual schematics of the locking scheme for the trap cavity is shown in Fig. 8.11. An 894 nm diode laser is used as the locking laser. This laser is locked to the same temperature stabilized cavity (see Sec. 3.4.4) as the 866 nm diode laser using a Pound-Drever-Hall locking scheme for both lasers. Before the 894 nm laser is sent to the trap table via an optical fiber it is frequency shifted by a double-pass acousto-optic modulator setup giving a frequency tuning range of $\pm 100$ MHz[1] for the locking laser. The 866 nm laser has likewise been made tunable with respect to the temperature stabilized cavity using an AOM. This part of the 866 nm laser setup is not included in Fig. 8.11, but is treated in Ref. [45].

The Pound-Drever-Hall scheme is used for locking the trap cavity to the 894 nm locking laser. The basics of this lock are illustrated in figure 8.11. In order to be able to obtain an error signal for the lock an EOM, which is controlled by the modulation signal from a local oscillator, is used for modulation of the locking laser beam, before it is coupled in as bow-tie mode in the trap cavity through one of the high reflecting mirrors. The cavity transmission of the laser beam is detected by a photodetector at one of the other high reflecting mirrors. The detected cavity transmission signal is then mixed with the modulation signal from the local oscillator to obtain the error signal [43, 44], which is used for the locking feedback to the cavity.

The wavelength of 894 nm has been chosen for two reasons. First of all it is far off resonant with any internal transitions in the $^{40}Ca^{+}$ ion which is a requirement for continuous cavity locking during the experiments. Second the wavelength is in the infrared where the mirror coatings have the highest

[1] The AOM is a Brimrose TEF 270 MHz ± 50 MHz.

reflectivity. This ensures a sufficiently high cavity finesse for the locking laser. The cavity mirror transmissions at $\lambda = 894$ nm have been measured and we find that the high reflective mirror transmission is $\mathcal{T} \sim 9.5 \times 10^{-4}$ and the in-coupling mirror transmission is $\mathcal{T} \sim 3.2 \times 10^{-3}$. This results in a finesse of $\mathcal{F} \sim 1000$ for the trap cavity at 894 nm which is only a factor of 4 lower than the finesse at 866 nm, so adequate cavity lock precision can be obtained using 894 nm as the locking laser wavelength.

# 9. LINEAR PAUL TRAP WITH OPTICAL RESONATOR

In the previous chapter the different aspects of the trap design were considered. In the present chapter the actual trap construction is presented together with an overview of the vacuum chamber in which the trap has been installed. The optical resonator is for this first generation quantum memory trap an asymmetric standing wave resonator consisting of a high reflecting mirror and in-coupling mirror with a transmission of $\mathcal{T} \sim 1500$ ppm. Measurements of the optical resonator finesse and losses are presented at the end of the chapter.

## *9.1 Trap and resonator construction*

The quantum memory trap setup, which can be seen in Fig. 9.1, was designed in collaboration with Henrik Bechtold (engineer at the institute). Figure 9.1(a) shows the fully assembled trap setup, which basically consists of a linear Paul trap construction mounted on an outer construction that holds the cavity mirrors.

### *9.1.1 Electrodes and mirror mounts*

The linear Paul trap electrodes are made of gold coated copper. The copper electrodes are mounted in a construction made of Macor. Connections to the electrodes are made by ∅1 mm copper wire that has been welded onto the electrodes. The whole Paul trap electrode construction can be translated and tilted with respect to the optical axis of the optical cavity. This translation and tilt are controlled by three screws that push the electrode construction down against two beryllium copper springs.

The cavity mirror mounts are made of titanium, because this metal exhibits a notably low diamagnetism and hence does not introduce magnetic fields in the trapping region. To keep the distance between the mirror mounts stable against fluctuations of the trap temperature they have been mounted on a ceramic material[1] of a special composition that has a very low thermal expansion coefficient of $\lesssim 1$ ppm/°C. In one end of the mirror mount construction the length of the optical cavity is controlled by three piezo tubes[2] glued onto the mirror mount. The idea of using three piezoes is that small misalignments of the cavity could be compensated by applying slightly different voltages to the piezoes that would tilt the mirror mount. In practice the construction turned

[1] Machinable ceramic (MC-LD) from MarkeTech International, Inc. [141]
[2] Ferroperm Piezoes (ref nr. 27202).

out to be too rigid for this tilt to have any noticeable effect on the cavity alignment, so we will probably only use one piezo in future versions of the quantum memory trap. Before the closure of the vacuum chamber the optical cavity is aligned by turning three set screws that tilts the piezo construction with respect the outer mirror mount construction. Each mirror is mounted in a ∅3.0 mm hole in the titanium and held in place by a small screw which is gently tightened against the mirror from the side. In Fig. 9.1(b) a picture is shown of the mirrors installed in the mirror mount.

### *9.1.2 Alignment of the trap*

The alignment of the linear Paul trap with respect to the optical cavity mode is very important in order to have proper overlap between the $^{40}Ca^{+}$ ions and the cavity mode (see Sec. 8.1.2). The cavity mode waist is $\sim 37$ $\mu$m, so the alignment precision should preferably be better than this.

In the setup stage of the quantum memory trap some precautions are taken to obtain this precision, but for a final adjustment a special tool has been made which consists of two thin plates with a 100 $\mu$m hole drilled in each plate. The plates are mounted on four rods such that they can be mounted in the Macor holder for the linear Paul trap. The holes define where the optical mode has to be in order to be centered on the linear Paul trap axis. The positioning of the linear Paul trap is done by sending light into the mode of the optical cavity, and then minimize the mode losses introduced by the finite size of the holes in the two plates.

### *9.1.3 Re-pump laser in-coupling*

Re-pump laser light at 866 nm is needed for laser cooling of the $^{44}Ca^{+}$ ions (see Sec. 2.2.1). For an efficient re-pumping out of the $3D_{3/2}$-state the angle between the linear Paul trap axis and the re-pump laser beam should be as small as possible. To couple sufficient re-pump laser light, which is resonant with the 866 nm transition of the $^{44}Ca^{+}$ ions, along the Paul trap axis would require that the cavity is on resonance with the light. This is not possible though, because the cavity at the same time has to be resonant with the 866 nm transition in the $^{40}Ca^{+}$ ions which is used for the $\Lambda$-transition in the quantum memory scheme (see Fig. 8.2).

Instead we have mounted two fused silica caps on the mirrors that act as reflectors for the 866 nm re-pump light for the $^{44}Ca^{+}$ ions and make a small angle between the re-pump laser beam and the Paul trap axis possible (see Fig. 9.1(d)). The fronts of the caps have a $\lambda/10$ surface quality and an infrared reflective coating. The beam path of the 866 nm re-pump laser is illustrated in Fig. 9.1(f), which shows a horizontal cross-section including the Paul trap axis of the trap construction seen from above. The angle of the 866 nm laser beam with respect to the trap axis is $\sim 11^{\circ}$ which is a sufficiently low angle to have an efficient re-pumping out of the $3D_{3/2}$ state in $^{44}Ca^{+}$. To confirm this we performed an experiment in the linear Paul trap described in Sec. 3.1 in which

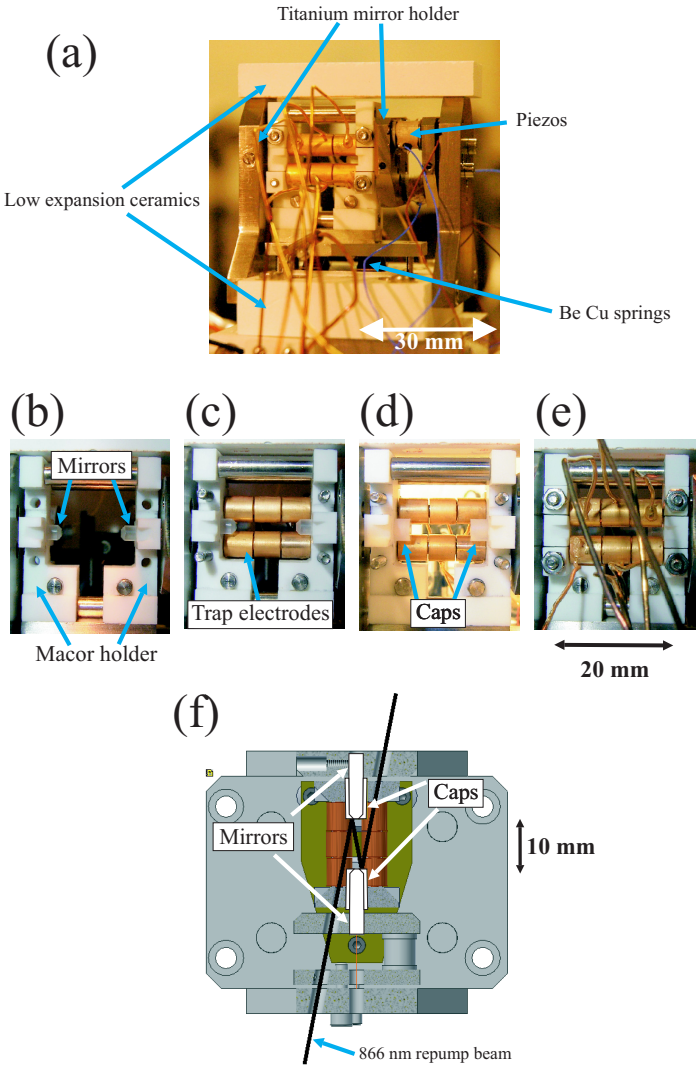


*Fig. 9.1:* Pictures of the quantum memory trap setup. (a) The full trap setup. (b) The bare mirrors. (c) The Paul trap electrodes mounted behind the mirrors. (d) Caps mounted on the mirrors. (e) All Paul trap electrodes mounted. (f) A cross section of the trap setup showing the re-pump laser beam path. The trap dimensions are listed in Table 8.1.

re-pumping of the $Ca^+$ ions was done under angle with respect to the Paul trap axis. In this experiment we saw that efficient laser cooling and crystallization of a medium sized $^{40}Ca^+$ Coulomb crystal is still possible when the re-pump angle is 45°.

Apart from acting as mirrors for the 866 nm re-pump light the caps also give rise to the substrate geometry that introduce the least axial micromotion. This subject was treated in Sec. 8.4, where it was argued that the end face of the substrate should be flat and substrate diameter as large as possible to minimize the axial micromotion induced by the presence of the mirror substrates.

## 9.2 UHV chamber

The quantum memory trap is mounted in an UHV chamber which was build as a part of the project. In this section we will describe the different parts of the vacuum chamber. An important design parameter has been to minimize magnetic fields in the trap region as discussed in Sec. 8.5. To reduce the number of magnetic field sources in the neighborhood of the trap region we have chosen non-magnetic materials as, for example, aluminum for most of the parts inside the vacuum chamber. The vacuum chamber and the laser table on which it has been installed are made in low-magnetic stainless steel. The UHV chamber geometry is similar to the UHV chamber described in Sec. 3.2, so here only a brief summary of the inside of the new UHV chamber will be presented. The UHV with a pressure of roughly $10^{-10}$ Torr is maintained by a titanium sublimation pump and an ion getter pump[3]. The pressure is monitored by an ion gauge. A photograph of the UHV chamber inside is shown in Fig. 9.2. A stainless steel plate with threaded holes, on which the various parts are mounted, has been installed in the chamber. Here the different parts in the photograph are described in detail:

- The quantum memory trap is situated in the center of the chamber. It is mounted on an aluminum base together with 20 in-line connectors mounted in 4 Macor blocks. The in-line connectors are used for connecting the trap electrode wires and the piezo wires to ∅1.0 mm copper wires that are connected to the trap feedthrough and the piezo feedthrough.

- The calcium and magnesium ovens are very similar in their construction to the ovens installed in the other vacuum chamber described in this Thesis and the reader is referred to Sec. 3.2 for a review of the basic oven construction. In the setup presented here the atoms effuse through a 4–5 mm long canal with a ∅0.4 mm diameter. Skimmers placed between the ovens and the quantum memory trap protect both the trap electrodes and the cavity mirrors from contamination. There are three vertical skimmers and two horizontal skimmers. The resulting beam size at the center of the linear Paul trap is ∼ 1.5 mm horizontally and ∼ 1.0 mm vertically. The Ca and Mg atomic beam directions make a 45° and a 57° angle with respect to

[3] Physical electronics 300 l/s Captorr ion pump.

the Paul trap axis, respectively. Isotope selective photo-ionization production of $Ca^+$ ions under a 90° angle is possible through two anti-reflection coated viewports.

- The optical access for the laser beams to the trap region parallel and perpendicular to the trap axis as well as in a 45° angle is provided through six viewports. The viewports have been anti reflection coated for the three wavelengths: 866 nm, 397 nm, and 272 nm. In Fig. 9.2(a) are also seen two mirrors denoted by M1 and M2. These mirrors have been introduced in the vacuum chamber, because the chamber geometry prohibits direct optical access through the viewports for the 866 nm re-pump laser, which needs to be send in under an 11° angle with respect to the trap axis (see Sec. 9.1). All the laser beam paths are indicated in Fig. 9.2(b). In the top flange (not shown in figure) a viewport is mounted through which the ion fluorescence from the Doppler laser cooling is imaged.

- The *oven shutter* is for blocking the atomic beams. It consists of an aluminum plate mounted on a rotary motion feedthrough, so it can be rotated in and out of the blocking position. The aluminum plate is designed such that the Ca oven and the Mg oven can be blocked individually.

- A small piece of optical fiber with a diameter of 80 $\mu$m has been mounted on a linear motion feedthrough, which is used to translate the fiber end in and out of the center of the linear Paul trap. The optical fiber can viewed by a CCD camera, when laser light is scattered from the tip of the fiber. This is used for initial alignment of cooling lasers and length scale calibration of the recorded images.

## 9.3 Cavity characterization

The cavity losses play a critical role for the fidelity of the quantum memory in ions as shown in Sec. 8.2 and therefore the cavity losses need to be measured. Here the methods used for characterization of the cavity are presented along with some data obtained for the standing wave cavity presently used in the quantum memory setup.

### 9.3.1 Theory

This section is devoted to deriving and discussing the basics of resonator theory which we use for characterization of the high finesse cavity. The discussion will be restricted to a resonator consisting of two mirrors (*Fabry-Perot resonator*), but the derivations here can easily be extended to more complex resonator setups as for instance the bow-tie cavity presented in Sec. 8.3.

In our efforts towards characterizing the cavity, the cavity finesse as well as the cavity round trip losses are important parameters. Information about these can be obtained in many ways. A simple model can be used to deduce the

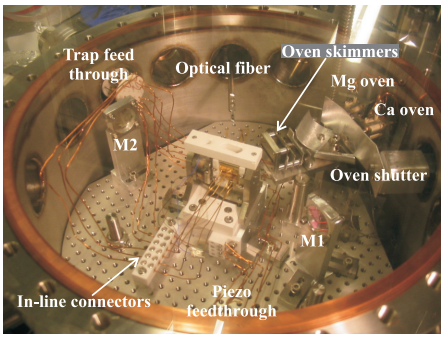


(a)

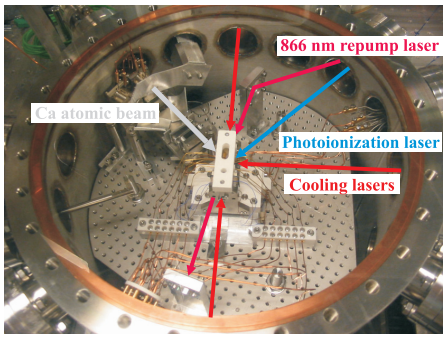


(b)

*Fig. 9.2:* Photos of the vacuum chamber for the quantum memory trap setup. (a) The different parts of the vacuum chamber. M1 and M2 denotes the two mirrors for the 866 nm re-pump beam. (b) Beam paths of the lasers and the atomic calcium beam. For a length scale note that the distance between nearest neighbor holes in the base plate of the vacuum chamber is 1 cm.

cavity finesse and the cavity round-trip losses from measurements of the cavity reflection and transmission signals when the cavity is scanned across resonance of the fundamental $\mathrm{TEM}_{00}$ mode.

In the following we will consider a Fabry-Perot cavity. Let the transmission for the in-coupling mirror be denoted by $T_1$ and the transmission of the high-reflecting mirror be denoted by $T_2$. The reflectivity of the mirrors we define as $R_i \equiv 1 - T_i$ for $i = 1, 2$. This definition of the reflectivity may at first glance appear a bit odd as there are also dissipative loss mechanisms at the surface of the mirrors that will reduce the actual mirror reflectivity. We cannot however easily measure the individual dissipative loss of each mirror, and therefore it makes more sense to treat this loss separately. Therefore we also introduce, $L$, as the fractional loss of intensity of a light field propagating one round trip in the cavity which cannot be attributed to light transmission through the mirrors. To simplify the equations below we also introduce the loss parameter $\alpha_L \equiv 1 - L$.

Considering the electric field amplitude of the intra-cavity circulating light just before the in-coupling mirror $E_{c_1}$ it is easily seen that this field relates to the in-coupling field amplitude $E_i$ as follows

$$\frac{E_{c_1}}{E_i} = \frac{\sqrt{\alpha_l(1-R_1)R_2}e^{i\delta}}{1-\sqrt{\alpha_L R_1 R_2}e^{i\delta}}, \tag{9.1}$$

where $\delta$ is the phase shift of the electric field for one cavity round trip. Similarly the electric field amplitude just before the high reflector mirror, $E_{c_2}$, is

$$\frac{E_{c_2}}{E_i} = \frac{\sqrt{\alpha_L(1-R_1)}e^{i\delta/2}}{1-\sqrt{\alpha_L R_1 R_2}e^{i\delta}}. \tag{9.2}$$

The field amplitude of the field transmitted through the high reflector, $E_t$, is related to the intra-cavity field by the relation $E_t/E_i = -\sqrt{1-R_2}E_{c_2}/E_i$ and the field amplitude reflected from the in-coupling mirror, $E_r$, is $E_r/E_i = -\sqrt{1-R_1}E_{c_1}/E_i + \sqrt{R_1}$. Now inserting the equations (9.1) and (9.2) into these expressions and taking the square modulus the reflected and the transmitted powers normalized to the incoming power become

$$\frac{P_r}{P_i} = \frac{R_1 + \alpha_L R_2 - 2\sqrt{\alpha_L R_1 R_2}\cos\delta}{1+\alpha_L R_1 R_2 - 2\sqrt{\alpha_L R_1 R_2}\cos\delta} \tag{9.3}$$

$$\frac{P_t}{P_i} = \frac{\alpha_L(1-R_1)(1-R_2)}{1+\alpha_L R_1 R_2 - 2\sqrt{\alpha_L R_1 R_2}\cos\delta}. \tag{9.4}$$

The reflected and transmitted powers have been plotted as a function of $\delta$ in Fig. 9.3(a). The FWHM width of the resonance $\delta_{\mathrm{FWHM}}$ is also indicated in the figure. From Eq. (9.4) the finesse is easily found as the ratio of the distance between two neighboring resonances ($2\pi$) and $\delta_{\mathrm{FWHM}}$, which gives

$$\mathcal{F} = \frac{2\pi}{\delta_{\mathrm{FWHM}}} = \pi\frac{(\alpha_L R_1 R_2)^{1/4}}{1-\sqrt{\alpha_L R_1 R_2}}. \tag{9.5}$$

For the case of a low loss and low transmission cavity ($T_1, T_2, L \ll 1$) Eq. (9.5) reduces to

$$\mathcal{F} \cong \frac{2\pi}{T_1+T_2+L}. \tag{9.6}$$

If we define $\rho \equiv \frac{P_r(\delta=0)}{P_r(\delta=\pi)}$, i.e., the reflected power on resonance divided by the reflected power off resonance, it is found that $\pm\rho = \frac{(R_1-x)(1+x)}{(R_1+x)(1-x)}$, where $x = \sqrt{\alpha_L R_1 R_2}$. The quantity $\rho$, which can be determined experimentally from the reflection signal, has been plotted in Fig. 9.3(b) as a function of the dissipative cavity round trip loss $L$ for a cavity with parameters similar to our cavity. It is seen that $\rho \simeq 1$ when the cavity losses are small. When the in-coupling transmission equals the sum of the dissipative losses of the cavity and the transmission of the out-coupling mirror ($T_1 = T_2 + L$) there is no reflected signal on cavity resonance ($\rho = 0$). In this situation the cavity is said to be *impedance matched.*

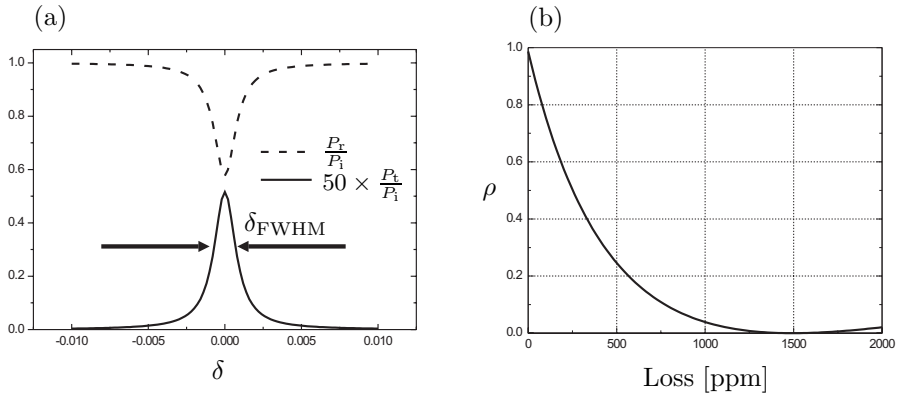


*Fig. 9.3:* (a) The transmission signal and reflected signal normalized to the incoming power for a cavity with $T_1 = 1500$ ppm, $T_2 = 5$ ppm, and $L = 200$ ppm (see Eq. (9.3)). The transmission signal is multiplied by a factor of 50 to account for the small cavity transmission signal. (b) Reflection dip, $\rho = \frac{P_r(\delta=0)}{P_r(\delta=\pi)}$, as function of the cavity round trip dissipative loss, $L$. The in-coupling transmission is $T_1 = 1500$ ppm and the high reflector transmission is $T_2 = 5$ ppm.

Using the approximation $(1 - R_1, 1 - R_2, L) \ll 1$ we arrive at a simple and highly useful expression for the cavity round-trip dissipative loss

$$L = T_1 \frac{1 \pm \sqrt{\rho}}{1 \mp \sqrt{\rho}} - T_2, \tag{9.7}$$

where the upper sign is used when the total cavity round trip loss exceeds the transmission of the in-coupling mirror ($T_2 + L > T_1$) and the lower sign is used when the total round trip loss is lower than the in-coupling transmission ($T_2 + L < T_1$).

### *9.3.2 Results and methods*

Both the cavity transmission signal and the reflected signal need to be measured to make a proper characterization of the cavity. We will now present such measurements and use them to calculate the cavity finesse and losses.

A schematic of the setup for this measurement is shown in Fig. 9.4. The 866 nm laser light is derived from a diode laser via an optical fiber and sent through a series of lenses for beam shaping such that beam is mode matched with the cavity. When appropriate mode matching and cavity alignment have been done the fundamental $\mathrm{TEM}_{00}$ mode dominates. The transmitted signal is measured simply by focussing the transmitted signal onto a detector. The reflected signal is separated from the incoming beam using a $\lambda/4$-plate and a polarization beam splitter and the light is then focused onto a detector. This configuration avoids that all the reflected light is sent directly back to the diode

laser. The diode laser is furthermore protected from cavity back reflections by two optical Faraday isolators.

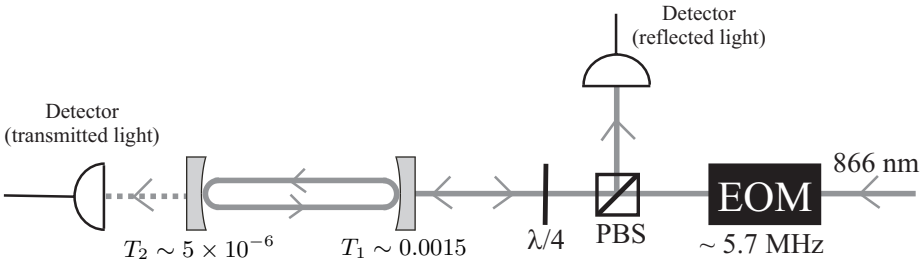


*Fig. 9.4:* Setup for cavity characterization.

The cavity length is scanned by applying a sawtooth scan voltage to the piezoes that control the cavity length. An example of such a scan signal when the cavity is scanned more than one free spectral range is shown together with the sawtooth scan signal in Fig. 9.5(a). The resonance peaks represent the increased cavity transmission for the $TEM_{00}$ cavity mode. Higher order cavity modes are also present in the scan and they are identified as small peaks with an amplitude of $\sim 0.1$ V in the scan.

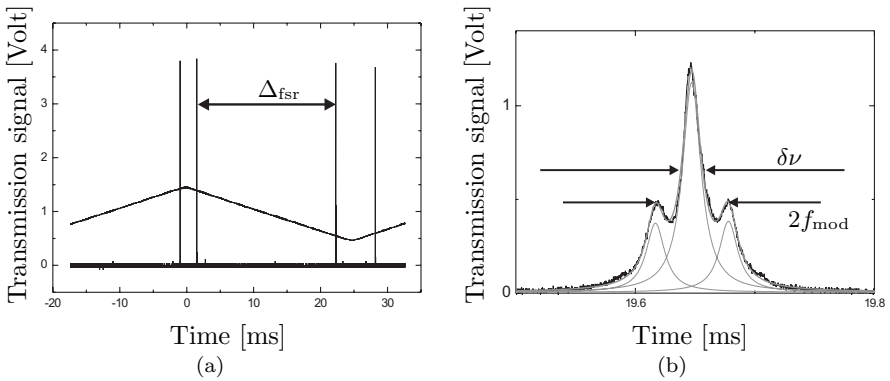


*Fig. 9.5:* (a) Transmission signal of the cavity when the cavity is scanning more than one free spectral range together with the sawtooth scan signal. (b) The transmission signal when the cavity is scanned slowly across the $TEM_{00}$-resonance of the cavity. The light sent to the cavity is modulated at frequency $f_{\mathrm{mod}} = 5.7$ MHz using an EOM.

The resonance width is established from the transmission signal of a slow scan of the cavity length across the fundamental $TEM_{00}$ cavity mode. The scan needs to be slow in order to avoid broadening effects of the resonance due to the finite rise time of the photo detector. To calibrate the measurement we introduce an electro optic modulator (EOM) in the laser beam path which produces sidebands at the modulation frequency $f_{\mathrm{mod}} \sim 5.7$ MHz. For each

resonance width measurement the modulation frequency is known to a 4-digit precision. The transmission signal of the cavity for the carrier an the first sidebands is shown in Fig. 9.5(b). A multi peak Lorentzian fit of the carrier and the two neighboring sidebands determines the peak positions and the Lorentzian width of the three peaks. The peak widths are assumed to be equal in the multi peak fit. In the example shown in Fig. 9.5(b) the resonance width is $\delta\nu \sim 3.3$ MHz. The resonance width measurements are extremely sensitive to acoustic noise in the laboratory, so in order to get good statistics the measurements are repeated several times.

A good measure for the quality of the cavity mirrors is the fidelity $\mathcal{F} \simeq 2\pi/(T_1 + T_2 + L)$ derived in Sec. 9.3.1, which only depends on the cavity mirror transmissions and the dissipative loss in the cavity. The finesse is found experimentally as the ratio between the cavity free spectral range $\Delta_{\text{fsr}}$ and the resonance width $\delta\nu$, i.e., $\mathcal{F} = \Delta_{\text{fsr}}/\delta\nu$. The free spectral range could be calculated from the length of the cavity, but it is very hard directly to measure the exact cavity length. Instead the free spectral range is measured optically by comparing the cavity free spectral range to a free spectral range of a laser stabilization cavity (see Sec. 3.4.4 for a description of the stabilization cavity). The procedure for this is as follows. A laser beam from the Ti:Sapph laser is split in two and sent both to the laser stabilization cavity and the quantum memory cavity. Then the Ti:Sapph laser frequency is manually tuned one free spectral range of the quantum memory cavity while the number of stabilization cavity free spectral ranges the laser frequency traverses is counted. The free spectral range for the stabilization cavity is 596 MHz, which also has been measured optically, but this time using the modulation frequency of a double pass acousto optic modulator as a reference. For the present cavity setup a free spectral range of $\Delta_{\text{fsr}} = (22.0 \pm 0.1) \times 596$ MHz $= 13.1 \pm 0.1$ GHz has been measured. Using this result together with measurements of the cavity resonance width we can deduce a cavity finesse of $\mathcal{F} = 4000 \pm 200$, which is consistent with the finesse of $\mathcal{F} \sim 4200$ expected from the nominal in-coupling transmission of $T \sim 1500$ ppm.

The finesse measurement reveals that the cavity dissipative losses are small compared to the transmission loss of the in-coupling mirror, but to get a quantitative measure of cavity losses a measurement of the amplitude of the resonance dip in the reflection signal is necessary. Our experience is that new mirrors which have not yet been cleaned typically have losses of a couple of 100 ppm. The mirrors are cleaned using a lens tissue and acetone or methanol. The best cleaning result is usually obtained by folding the lens tissue a few times to get some layers of tissue such that a moderate pressure of the lens tissue against the mirror surface is applied. Figure 9.6 shows the cavity reflection dip after such a cleaning. The cavity loss deduced from this measurement is $L + T_2 \sim 28$ ppm, which is the lowest loss we have obtained using the described cleaning method. The cavity losses are very sensitive to dust particles in the air which will contaminate the mirror surfaces. To protect the mirrors from dust a plexiglass house for the setup (1 m $\times$ 0.5 m $\times$ 0.5 m) has been built. The dust free environment

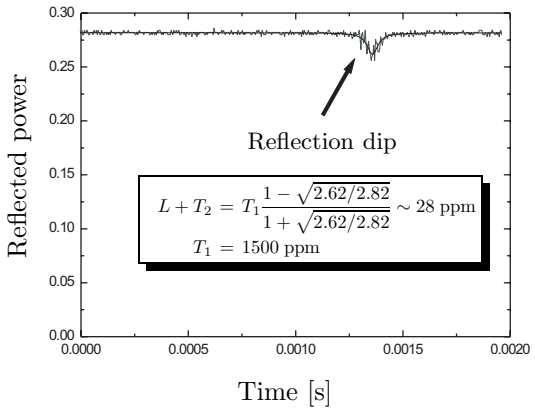


*Fig. 9.6:* Reflection signal from the cavity fitted to a Lorentzian. The total cavity round-trip loss calculated from this reflection dip is $L + T_2 \sim 28$ ppm as shown in the insert.

is obtained by blowing air[4] cleaned with a HEPA-filter into the plexiglass house at a rate of 0.5 lites per second.

[4] Using an air pump Nitto Kohki LA 28 B

# 10. SUMMARY AND OUTLOOK

The present Thesis has covered different aspects of the construction and development of an experiment on quantum memory for light in two component ion Coulomb crystals consisting of $^{40}Ca^{+}$ and $^{44}Ca^{+}$ ions. A central part of the work has been to build a linear Paul trap with an integrated optical resonator. The linear Paul trap is the first of its kind where the Paul trap axis and the optical axis of the resonator coincide, and the Paul trap construction at the same time is designed to confine large ion Coulomb crystals. The linear Paul trap is now installed in a low-magnetic UHV chamber and the first ion trapping experiments have been initialized. In the present trap setup the resonator is a standing wave resonator, but a running wave resonator setup is ultimate goal for the trap setup. We are currently working on the realization of this running wave resonator setup. Resonator round trip losses on the order of a few tens ppm have been measured in the standing wave resonator setup. If we include these cavity losses in the simulations of single photon storage in the bow-tie configuration, the predicted attainable fidelity of the light storage becomes $F \sim 0.9$.

Numerical simulations of the trapping fields have been used in the design phase of the linear Paul trap with integrated resonator to estimate the magnitude of the axial micromotion introduced by the presence of the resonator substrates. Our conclusion is that with the right choice of substrate geometry the magnitude of the axial micromotion will not be critical for the experiment. The magnetic fields in the trapping region need to be reduced to a few mG. A bias magnetic field along the trap axis, which will decrease the decoherence rate of the ions caused by Larmor precession, has furthermore to be applied.

With the aim of being able to produce the large bi-crystals consisting of two isotopes of calcium experiments on isotope-selective photo-ionization loading of calcium in a regular linear Paul trap have been carried out. The photo-ionization experiments indicated that ions of all naturally occurring isotopes can be produced from natural calcium, including the extremely rare $^{46}Ca$ isotope which has an abundance of only 0.004%. For the $^{44}Ca$ isotope, that has an abundance of 2.086%, the isotope selectivity of $\eta_{44} \sim 1100$ is sufficient for the purpose of producing the large $^{40}Ca^{+}$–$^{44}Ca^{+}$ bi-crystals needed for the quantum memory experiment. As a tool for controlling the ratio of $^{40}Ca^{+}$ and $^{44}Ca^{+}$ ions in the bi-crystal the near electron transfer between the atoms in the atomic beam and the trapped ions is utilized.

Ionization rate measurements as a function of the ionization laser detuning revealed the hitherto unknown isotope shifts of the $4s^2\ ^1S_0 \leftrightarrow 4s5p\ ^1P_1$ transition in calcium and the hyperfine splitting of $4s5p\ ^1P_1$ state of $^{43}Ca$. From these

data the field shift and specific mass shift coefficients as well as the hyperfine structure constants for $^{43}$Ca were deduced.

We have also performed experiments on collisions between trapped laser cooled calcium ions and calcium atoms in an effusive beam. These experiments offer an opportunity to study the low-energy near resonant charge transfer between ions of a low abundant isotope, as for instance $^{44}Ca^{+}$, and $^{40}$Ca atoms. A technique has been demonstrated to measure the atomic beam profile of the effusive beam by probing the charge transfer rate at different locations in the atomic beam. The atomic flux in the atomic beam was estimated from the temperature of the atomic beam and the theory of effusive beams. This has been used to calculate the near resonant charge transfer cross section, which is found to be an order of magnitude larger than the cross section predicted from an extrapolation of higher energy charge transfer data. Greater confidence in the experimental cross section result would be obtained by improving the atomic flux estimate, which for instance is found by using absorption spectroscopy on the $4s^2\ ^1S_0 \leftrightarrow 4s4p\ ^1P_1$ transition in neutral calcium.

The structural properties of single component $Ca^{+}$ ion Coulomb crystals have been studied. For large Coulomb crystals with ion numbers exceeding 10,000 transitions between fcc and bcc lattice structures are observed. According to theoretical predictions smaller spherically symmetric ion Coulomb crystals with ion numbers below 10,000 ions the ions arrange in concentric spheres of different radii throughout the crystal. Besides observing these shell structures a transition to long-range lattice structures has been observed. The different structures are co-existing for the same set of trap parameters and presumably induced by the finite temperature of the ion crystal.

For two component ion Coulomb crystal consisting of $^{40}Ca^{+}$ and $^{44}Ca^{+}$ ions we have seen the concentric shell structure of the $^{40}Ca^{+}$ crystal core predicted from previous MD simulations and observations of bi-crystals in a linear Paul trap. The shell structure of the $^{40}Ca^{+}$ core resembles the structure of an one component Coulomb crystal confined in an infinitely long cylindrically symmetric static harmonic potential. Quite surprisingly our results show that this structure is not unique, but instead a transition to a fc-orthorhombic lattice structure of the $^{40}Ca^{+}$ core exists for certain configurations of the trapping parameters and sizes of the Coulomb crystals. MD simulations of the bi-crystals which include the full time-dependent potential, indicate that the existence of the fc-orthorhombic lattice structure in the crystal core is induced by the time variation of the confining rf-potential of the linear Paul trap. We find a qualitative agreement between the experimentally observed rectangular structure of the crystal projection and the MD simulations, but quantitatively there is a small deviation of 7% which is at present not fully understood.

# BIBLIOGRAPHY


[1] N. V. Vitanov, M. Fleischhauer, B. W. Shore, and K. Bergmann. Coherent manipulation of atoms and molecules by sequential laser pulses. *Adv. At., Mol., and Opt. Phys.*, 46:55–190, 2001.

[2] H. J. Kimble. Strong interactions of single atoms and photons in cavity QED. *Phys. Scr.*, T76:127–137, 1998.

[3] S. E. Harris. Electromagnetically induced transparancy. *Phys. Today*, 50:36, July 1997.

[4] C. Liu, Z. Dutton, C. H. Behroozi, and L. V. Hau. Observation of coherent optical information storage in an atomic medium using halted light pulses. *Nature*, 409:490–493, 2001.

[5] D. F. Phillips, A. Fleischhauer, A. Mair, R. L. Walsworth, and M. D. Lukin. Storage of light in atomic vapor. *Phys. Rev. Lett.*, 86(Iss. 5):783–786, 2001.

[6] C. A. Sackett, D. Kielpinski, B. E. King, C. Langer, V. Meyer, C. J. Myatt, M. Rowe, Q. A. Turchette, W. M. Itano, D. J. Wineland, and C. Monroe. Experimental entanglement of four particles. *Nature*, 404:256–259, 2000.

[7] M. Keller, B. Lange, K. Hayasaka, W. Lange, and H. Walther. A calcium ion in a cavity as a controlled single-photon source. *New J. Phys.*, 6:95, 2004.

[8] M. Fleischhauer, S. F. Yelin, and M. D. Lukin. How to trap photons? Storing single-photon quantum states in collective atomic excitations. *Opt. Comm.*, 179:395–410, 2000.

[9] W. Paul, H. P. Reinhard, and U. von Zahn. Das electrische massenfilter als massen spektrometer und isotopentrenner. *Z. Phys.*, 152:143–182, 1958.

[10] J. D. Prestage, G. J. Dick, and L. Maleki. New ion trap for frequency standard applications. *J. Appl. Phys.*, 66:1013–1017, August 1989.

[11] E. Fisher. Die dreidimensionale stabilisierung von ladungstragern in einem vierpolfeld. *Z. Phys.*, 156:1–26, 1959.

[12] H. G. Dehmelt. Radiofrequency spectrocopy of stored ions: I storage. *Adv. At. Mol. Phys*, 3:53–72, 1967.

[13] D. A. Church. Storage-ring ion trap derived from the linear quadrupole radio-frequency mass filter. *J. Appl. Phys.*, 40:3127–3134, 1969.

[14] Pradip K. Ghosh. *Ion Traps.* Oxford University Press inc., New York, 1995.

[15] Jon Matthews and R. L. Walker. *Mathematical Methods of Physics.* Addison-Wesley, 2 edition, 1970.

[16] D. Wineland and H. Dehmelt. Proposed $10^{14}\delta\nu < \nu$ laser fluorescence spectroscopy on $Tl^+$ mono-ion oscillator III. *Bull. Am. Phys. Soc.*, 20:637, 1975.

[17] F. Diedrich, J. C. Bergquist, Wayne M. Itano, and D. J. Wineland. Laser cooling to the zero-point energy of motion. *Phys. Rev. Lett.*, 62:403–406, 1989.

[18] Peter Staanum. *Quantum optics with trapped calcium ions.* PhD thesis, University of Aarhus, february 2004.

[19] H. J. Metcalf and P. Van der Straten. *Laser Cooling and Trapping.* Springer-Verlag, New York, 1999.

[20] D. F. V. James. Quantum dynamics of cold trapped ions with application to quantum computation. *Appl. Phys. B*, B66:181–190, 1998.

[21] I. Siemers, M. Schubert, R. Blatt, W. Neuhauser, and P. E. Toshek. The "trapped state" of a trapped ion–line shifts and shape. *Europhys. Lett.*, 18(2):139–144, 1992.

[22] A.-M. Mårtensson-Pendrill, A. Ynnermann, and H. Warston. Isotope-shifts and nuclear-charge radii in singly ionized $^{40-48}Ca^+$. *Phys. Rev. A*, 45(7):4675–4681, april 1992.

[23] W. Alt, M. Block, V. Schmidt, T. Nakamura, P. Seibert, X. Chu, and G. Werth. Shifts of the $3D-4P$ transitions in different isotopes of positive calcium ions. *J. Phys. B*, 30:L677–L681, 1997.

[24] E. Wigner. On the interaction of electrons in metals. *Phys. Rev.*, 46:1002–1011, 1934.

[25] H. W. Jiang, R. L. Willett, H. L. Stormer, D. C. Tsui, L. N. Pfeiffer, and K. W. West. Quantum liquid versus electron solid around $\nu = \frac{1}{5}$ Landau-level filling. *Phys. Rev. Lett.*, 65(5):633–636, 1990.

[26] H. Thomas, G. E. Morfill, V. Demmel, J. Goree, B. Feuerbacher, and D. Möhlmann. Plasma crystal: Coulomb crystallization in a dusty plasma. *Phys. Rev. Lett.*, 73:652–655, 1994.

[27] H. M. Van Horn. Dense astrophysical plasmas. *Science*, 252:384–389, 1991.

[28] J. P. Hansen. Statistical mechanics of dense ionized matter. I. equilibrium properties of the classical one-component plasma. *Phys. Rev. A*, 8:3096–3109, 1973.

[29] E. L. Pollock and J. P. Hansen. Statistical mechanics of dense ionized matter. II. equilibrium properties and melting transition of the crystallized one-component plasma. *Phys. Rev. A*, 8:3110–3122, 1973.

[30] W. L. Slattery, G. D. Doolen, and H. E. DeWitt. Improved equation of state for the classical one-component plasma. *Phys. Rev. A*, 21:2087–2095, 1980.

[31] J. P. Schiffer. Order in very cold confined plasmas. *Hyp. Interact.*, 103:71–79, 1996.

[32] K. Mølhave and M. Drewsen. Formation of translationally cold $MgH^+/MgD^+$ molecules in an ion trap. *Phys. Rev. A*, 62:011401(R), 2000.

[33] A. Bertelsen, I. S. Vogelius, S. Jørgensen, R. Kosloff, and M. Drewsen. Photo-dissociation of cold $MgH^+$ ions: Towards rotational temperature measurements and controlled dissociation. *Eur. Phys. J. D*, 31(2):403–408, 2004.

[34] Liv Hornekær. *Single- and Multi-Species Coulomb Ion Crystals: Structures, Dynamics and Sympathetic Cooling.* PhD thesis, University of Aarhus, November 2000.

[35] P. Bowe, L. Hornekær, C. Brodersen, M. Drewsen, J. S Hangst, and J. P. Schiffer. Sympathetic crystalization of trapped ions. *Phys. Rev. Lett.*, 82:2071, 1999.

[36] N. Kjærgaard, L. Hornekær, A.M. Thommesen, Z. Videsen, and M. Drewsen. Isotope selective loading of an ion trap using resonance-enhanced two-photon ionization. *Appl. Phys. B*, 71:207–210, may 2000.

[37] J. L. Hall and S. A. Lee. Interferometric real-time display of cw dye laser wavelength with sub-doppler accuracy. *Appl. Phys. Lett.*, 29(6):367–369, 1976.

[38] Ryuzo Ohmukai, Masayoshi Watanabe, Hidetsuka Imajo, Kazuhiro Hayasaka, and Shinji Urabe. Doppler-free optogalvanic spectroscopy of $Ca^+$ and Ca. *Jpn. J. Appl. Phys.*, 33:311–314, 1994.

[39] A. M. Thommesen. Optogalvanic effects in a $\Lambda$-level system of $Ca^+$ and application in laser cooling. Master's thesis, University of Aarhus, 2000.

[40] T. W. Hänsch and B. Couillaud. Laser frequency stabilization by polarization spectroscopy of a reflecting reference cavity. *Optics Communications*, 35(Iss. 3):441–444, 1980.

[41] J. J. T. Lindballe. Eksperimenter med resonant to-foton isotopselektiv fotoionisation af calcium ved anvendelse af en frekvensfordoblet farvestoflaser. Master's thesis, University of Aarhus, 2003.

[42] L. Ricci, M. Weidemüller, T. Esslinger, A. Hemmerich, C. Zimmermann, V. Vuletic, W. König, and T. W. Hänsch. A compact grating-stabilized diode laser system for atomic physics. *Opt. Comm.*, 117:541–549, 1994.

[43] Eric D. Black. An introduction to Pound-Drever-Hall laser frequency stabilisation. *Am. J. Phys.*, 69:79–87, 2001.

[44] R. W. P. Drever, J. L. Hall, F. V. Kowalski, J. Hough, G. M. Ford, A. J. Munley, and H. Ward. Laser phase and frequency stabilization using an optical resonator. *Appl. Phys. B*, 31:97–105, 1983.

[45] Frank K. Jensen. Laser frequency stabilization for use in stirap experiments. Master's thesis, University of Aarhus, 2004.

[46] S. Gulde, D. Rotter, P. Barton, F. Schmidt-Kaler, R. Blatt, and W. Hogervorst. Simple and efficient photo-ionization loading of ions for precision ion-trapping experiments. *Appl. Phys. B*, 73:861–863, November 2001.

[47] J. E. Hansen, C. Laughlin, H. W. van der Hart, and G. Verbockhaven. Energy levels, wavefunction compositions and electric dipole transitions in neutral Ca. *J. Phys. B*, 32:2099–2137, 1999.

[48] N. Beverini, E. Maccioni, F. Sorrentino, V. Baraulia, and M. Coca. Measurement of the $4s^2\ {}^1S_0 \leftrightarrow 4s3d\ {}^1D_2$ transition probability in calcium. *J. Phys. D*, 23(2):223–228, 2003.

[49] G. Smith. Oscillator strengths for neutral calcium lines of 2.9 eV excitation. *J. Phys. B*, 21:2827–2834, 1988.

[50] J. Sugar and C. Corliss. Atomic energy levelsof the iron-period elements: Potassium through nickel. *J. Phys. Chem. Ref. Data*, 14:1–664, 1985.

[51] D. M. Lucas, A. Ramos, J. P. Home, M. J. McDonnell, S. Nakayama, J.-P. Stacey, S. C. Webster, D. N. Stacey, and A. M. Steane. Isotope-selective photoionization for calcium ion trapping. *Phys. Rev. A*, 2004.

[52] J. Mitroy. Energy levels and oscillator strengths for neutral calcium. *J. Phys. B*, 26(21):3703–3718, 1993.

[53] A. K. Pulhani, G. P. Gupta, and B. M. Suri. Isotopic selectivity calculations for multi-step photoionization of calcium atoms using narrow-band lasers. *J. Phys. B*, 35(17):3677–3688, 2002.

[54] C-J. Lorenzen, K. Niemax, and L. R. Pendril. Isotope shifts of energy levels in the naturally abundant isotopes of strontium and calcium. *Phys. Rev. A*, 28:2051–2058, 1983.

[55] N. Vaeck, M. Godefroid, and J. E. Hansen. MCHF oscillator strength and lifetime calculations in neutral calcium. *J. Phys. B*, 24(2):361–381, 1991.

[56] W. H. Smith and H. S. Liszt. Absolute oscillator strengths for some resonance multiplets of Ca I,II, Mg I,II, BI, and A1 I. *J. Opt. Soc. Amer.*, 61(7):938–941, 1971.

[57] M. S. Mathur and F. M. Kelly. Hanle effect of the $5p^1\ P_1^0$ level of calcium and its density dependence. *Can. J. Phys.*, 60:1237–1240, 1982.

[58] K. Heilig and A. Steudel. Changes in mean-quare nuclear charge radii from optical isotope shifts. *At. Data Nucl. Data Tables*, 14:613–638, 1974.

[59] E. G. Nadjakov, K. P. Marinova, and Yu. P. Gangrsky. Systematics of nuclear charge radii. *At. Data Nucl. Data Tables*, 56:133–157, 1994.

[60] H. B. G. Casimir. *On the Interaction Between Atomic Nuclei and Electrons.* Teyler's tweede Genootschap, Haarlem, 1936.

[61] C. W. P. Palmer, P. E. G. Baird, S. A. Blundell, J. R. Brandenberger, C. J. Foot, D. N. Stacey, and G. K. Woodgate. Laser spectrocopy of calcium isotopes. *J. Phys. B*, 17:2197–2211, 1984.

[62] W. Nörtershäuser, N. Trautmann, K. Wendt, and B. A. Bushaw. Isotope shifts and hyperfine structure in the $4s^2\ ^1\mathrm{S}_0$ *to* $4s4d\ ^1\mathrm{D}_2$ transitions of stable calcium isotopes and calcium-41. *Spectrochim. Acta, Part B*, 53:709–721, 1998.

[63] P. Müller, B. A. Bushaw, W. Nörtershäuser, and K. Wendt. Isotope shifts and hyperfine structure in calcium $4snp\ ^1P_1$ and $4snf\ F$ Rydberg states. *Eur. Phys. J. D*, 12:33–44, 2000.

[64] S. Maleki and A. T. Goble. Isotope-shift measurement in $Ca^+$. *Phys. Rev. A*, 45(1):524–526, 1992.

[65] F. Kurth, T. Gudjons, B. Hilbert, T. Reisinger, G. Werth, and A.-M. Mårtensson-Pendrill. Doppler free "dark resonances" for hyperfine measurements and isotopeshifts in $Ca^+$ isotopes in a Paul trap. *Z. Phys. D*, 34:227–232, 1995.

[66] I. I. Sobel'man. *Introduction to the theory of atomic spectra.* Pergamon press Ltd., 1972.

[67] G. S. Panev, A. N. Zavilopulo, J. P. Zapesochnyi, and O. B. Shpenik. *Sov. Phys. JETP*, 40(23), 1975.

[68] J. A. Rutherford, R. F. Mathis, B. R. Turner, and D. A. Wroom. Formation of calcium ions by charge transfer. *Jour. Chem. Phys.*, 57(8):3087–3090, 1972.

[69] B. Liu and R. E. Olson. Potential energies for $Ca_2^+$: cross sections for collisions of $Ca^+$ and Rydberg $Ca^{**}$ with Ca. *Phys. Rev. A*, 18(6):2498–2505, 1978.

[70] G. Gioumousis and D. P. Stevenson. Reactions of gaseous molecule ions with gaseous molecules. v. theory. *J. Chem. Phys.*, 29(2):294–299, 1958.

[71] David R. Lide, editor. *CRC Handbook of chemistry and physics*. CRC press, 72 edition, 1992.

[72] B. H. Bransden and C. J. Joachain. *Physics of atoms and molecules*. Addison Wesley Longman Limited, 1983.

[73] D. Rapp and W. E. Francis. Charge exchange between gaseous ions and atoms. *J. Chem. Phys.*, 37(11):2631–2645, 1962.

[74] Norman F. Ramsey. *Molecular Beams*. Oxford, 1956.

[75] Giacinto Scoles, editor. *Atomic and molecular beam methods*, volume 1, chapter 4. New York: Oxford University Press, 1988.

[76] F. Diedrich, E. Peik, J. M. Chen, W. Quint, and H. Walther. Observation of a phase transition of stored laser-cooled ions. *Phys. Rev. Lett.*, 59(26):2931–2935, 1987.

[77] D. J. Wineland, J. C. Bergquist, Wayne M. Itano, J. J. Bollinger, and C. H. Manney. Atomic-ion Coulomb clusters in an ion trap. *Phys. Rev. Lett.*, 59(26):2935–2938, 1987.

[78] G. Birkl, S. Kassner, and H. Walther. Multiple-shell structures of laser-cooled $^{24}Mg^+$ ions in a quadrupole storage ring. *Nature*, 357:310–313, 1992.

[79] M. Drewsen, C. Brodersen, L. Hornekær, J. S. Hangst, and J. P. Schifffer. Large ion crystals in a linear Paul trap. *Phys. Rev. Lett.*, 81:2878, 1998.

[80] M. Block, A. Drakoudis, H. Leuthner, P. Seibert, and G. Werth. Crystalline ion structures in a Paul trap. *J. Phys. B*, 33(11):L375–L382, 2000.

[81] S. L. Gilbert, J. J. Bollinger, and D. J. Wineland. Shell-structure phase of magnetically confined strongly coupled plasmas. *Phys. Rev. Lett.*, 60:2022–2025, 1988.

[82] T. B. Mitchell, J. J. Bollinger, D. H. E. Dubin, X.-P. Huang, W. M. Itano, and R. H. Baughman. Direct Observations of Structural Phase Transitions in Planar Crystallized Ion Plasmas. *Science*, 282(5392):1290–1293, 1998.

[83] J. N. Tan, J. J. Bollinger, B. Jelenkovic, and D. J. Wineland. Long-range order in laser-cooled, atomic-ion wigner crystals observed by bragg scattering. *Phys. Rev. Lett.*, 75:4198–4201, 1995.

[84] W. M. Itano, J. J. Bollinger, J. N. Tan, B. Jelenković, X.-P. Huang, and D. J. Wineland. Bragg Diffraction from Crystallized Ion Plasmas. *Science*, 279(5351):686–689, 1998.

[85] Rainer W. Hasse. A semiempirical mass formula for spherical coulomb crystals. *J. Phys. B*, 36(5):1011–1017, 2003.

[86] Hiroo Totsuji, Tokunari Kishimoto, Chieko Totsuji, and Kenji Tsuruta. Competition between two forms of ordering in finite coulomb clusters. *Physical Review Letters*, 88(12):125002, 2002.

[87] J. Farges, M. F. de Feraudy, B. Raoult, and G. Torchet. Noncrystalline structure of argon clusters. II. Multilayer icosahedral structure of $Ar_N$ clusters $50 < N < 750$. *J. Chem. Phys.*, 84(6):3491–3501, 1986.

[88] R. W. Hasse and V. V. Avilov. Structure and madelung energy of spherical Coulomb crystals. *Phys. Rev. A*, 44(7):4506–4515, 1991.

[89] F. H. Stillinger and T. A. Weber. Packing structures and transitions in liquids and solids. *Science*, 225:983–989, 1984.

[90] L. Hornekær, N. Kjærgaard, A. M. Thommesen, and M. Drewsen. Structural properties of two-component Coulomb crystals in linear Paul traps. *Phys. Rev. Lett.*, 86:1994, 2001.

[91] R. W. Hasse and J. P. Schiffer. The structure of the cylindically confined Coulomb lattice. *Ann. Phys.*, 203:419–448, 1990.

[92] Thierry Matthey. *Framework Design, Parallelization and Force Computation in Molecular Dynamics*. PhD thesis, University of Bergen, Norway, 2002.

[93] Esben S. Nielsen. Multikomponent Coulombkrystaller: Eksperimenter og simulationer. Master's thesis, University of Aarhus, 2004.

[94] David P. DiVincenzo. Quantum computation. *Science*, 270(5234):255–261, October 1995.

[95] David P. DiVincenzo. The physical implementation of quantum computation. *Preprint quant-ph/0002077 at ⟨http://xxx.lanl.gov⟩*, 2000.

[96] J. I. Cirac, P. Zoller, H. J. Kimble, and H. Mabuchi. Quantum state transfer and entanglement distribution among distant nodes in a quantum network. *Phys. Rev. Lett.*, 78:3221–3224, 1997.

[97] G. K. Brennen, C. M. Caves, P. S. Jessen, and I. H. Deutsch. Quantum logic gates in optical lattices. *Phys. Rev. Lett.*, 82:1060–1063, 1999.

[98] D. Jaksch, H.-J. Briegel ans J. I. Cirac, C. W. Gardiner, and P. Zoller. Entanglement of atoms via cold controlled collisions. *Phys. Rev. Lett.*, 82:1975–1978, 1999.

[99] D. Jaksch, J. I. Cirac, P. Zoller, S. L. Rolston, R. Côté, and M. D. Lukin. Fast quantum gates for neutral atoms. *Phys. Rev. Lett.*, 85:2208, 2000.

[100] J. I. Cirac and P. Zoller. Quantum computations with cold trapped ions. *Phys. Rev. Lett.*, 74:4091–4094, 1995.

[101] C. Monroe, D. M. Meekhof, B. E. King, W. M. Itano, and D. J. Wineland. Demonstration of a fundamental quantum logic gate. *Phys. Rev. Lett.*, 75:4714–4717, 1995.

[102] M. D. Lukin, S. F. Yelin, and M. Fleischhauer. Entanglement of atomic ensembles by trapping correlated photon states. *Phys. Rev. Lett.*, 84:4232–4235, 2000.

[103] M. Fleischhauer and C. Mewes. 'stopping' of light and quantum memories for photons. In F. De Martini and C. Monroe, editors, *Experimental Quantum Computation and Information*, volume 148, pages 511–529. International school of physics "Enrico Fermi", 2002.

[104] Rodney Loudon. *The quantum theory of light.* Claredon Press, Oxford, 1973.

[105] R. H. Dicke. Coherence in spontaneous radiation processes. *Phys. Rev.*, 93(1):99–110, January 1954.

[106] M. Gross and S. Haroche. Superradiance: an essay on the emmission of collective spontaneous emmission. *Phys. Rep.*, 92(5):301–396, 1982.

[107] E. Arimondo. Coherent population trapping in laser spectroscopy. *Prog. Opt.*, 35:257, 1996.

[108] M. Fleischhauer and M. D. Lukin. Dark-state polaritons in electromagnetically induced transparency. *Phys. Rev. Lett.*, 84:5094–5097, 2000.

[109] M. Fleischhauer and M. D. Lukin. Quantum memory for photons: Dark-state polaritons. *Phys. Rev. A*, 65(2):022314, 2002.

[110] K. Bergmann, H. Theuer, and B. W. Shore. Coherent population transfer among quantum states of atoms and molecules. *Rev. Mod. Phys.*, 70:1003–1025, 1998.

[111] M. Hennrich, T. Legero, A. Kuhn, and G. Rempe. Vacuum-stimulated Raman scattering based on adiabatic passage in a high-finesse optical cavity. *Phys. Rev. Lett.*, 85:4872–4875, 2000.

[112] L. V. Hau, S. E. Harris, Z. Dutton, and C. H. Behroozi. Light speed reduction to 17 metres per second in an ultracold atomic gas. *Nature*, 397:594–598, 1999.

[113] M. D. Lukin, M. Fleischhauer, M. O. Scully, and V. L. Velichansky. Intracavity electromagnetically induced transparency. *Opt. Lett.*, 23:295–297, 1998.

[114] D. Bouwmeester, A. Ekert, and A. Zeilinger, editors. *The Physics of Quantum Information*. Springer-Verlag, Berlin, 2000.

[115] Anthony E. Siegman. *Lasers*. University Science Books, California, 1986.

[116] A. Mair, J. Hager, D. F. Phillips, R. L. Walsworth, and M. D. Lukin. Phase coherence and control of stored photonic information. *Phys. Rev. A*, 65(Iss. 3):031802/1–4., 2002.

[117] A. Kasapi, Maneesh Jain, G. Y. Yin, and S. E. Harris. Electromagnetically induced transparency: Propagation dynamics. *Phys. Rev. Lett.*, 74:2447–2450, 1995.

[118] D. Budker, D. F. Kimball, S. M. Rochester, and V. V. Yashchuk. Nonlinear magneto-optics and reduced group velocity of light in atomic vapor with slow ground state relaxation. *Phys. Rev. Lett.*, 83:1767–1770, 1999.

[119] M. M. Kash, V. A. Sautenkov, A. S. Zibrov, L. Hollberg, G. R. Welch, M. D. Lukin, Y. Rostovtsev, E. S. Fry, and M. O. Scully. Ultraslow group velocity and enhanced nonlinear optical effects in a coherently driven hot atomic gas. *Phys. Rev. Lett.*, 82:5229–5232, 1999.

[120] G. Juzeliunas and H. J. Carmichael. Systematic formulation of slow polaritons in atomic gases. *Phys. Rev. A*, 2002.

[121] Hong Gao, Mark Rosenberry, and Herman Batelaan. Light storage with light of arbitrary polarization. *Phys. Rev. A*, 67(5):053807, 2003.

[122] A. V. Turukhin, V. S. Sudarshanam, M. S. Shahriar, J. A. Musser, B. S. Ham, and P. R. Hemmer. Observation of ultraslow and stored light pulses in a solid. *Phys. Rev. Lett.*, 88(2):023602, 2002.

[123] B. S. Ham, P. R. Hemmer, and M. S. Shahriar. Efficient electromagnetically induced transparency in a rare-earth doped crystal. *Optics Communications*, 144:227–230, 1997.

[124] M. Bajcsy, A. S. Zibrov, and M. D. Lukin. Stationary pulses of light in an atomic medium. *Nature*, 426:638–641, 2003.

[125] B. Julsgaard, A. Kozhekin, and E. S. Polzik. Experimental long-lived entanglement of two macroscopic objects. *Nature*, 413:400–403, 2001.

[126] B. Julsgaard, J. Sherson, J. I. Cirac, J. Fiurášek, and E. S. Polzik. Experimental demonstration of quantum memory for light. *Nature*, 432:482–486, 2004.

[127] A. Kuzmich and E. S. Polzik. Atomic quantum state teleportation and swapping. *Phys. Rev. Lett.*, 85:5639–5642, 2000.

[128] K. Hammerer, K. Molmer, E. S. Polzik, and J. I. Cirac. Light-matter quantum interface. *Phys. Rev. A*, 70(4):044304, 2004.

[129] D. Kruse, M. Ruder, J. Benhelm, C. von Cube, C. Zimmermann, Ph. W. Courteille, Th. Elsässer, B. Nagorny, and A. Hemmerich. Cold atoms in a high-$Q$ ring cavity. *Phys. Rev. A*, 67(5):051802, 2003.

[130] H. Kogelnik and T. Li. Laser beams and resonators. *Appl. Opt.*, 5(10):1550–1567, October 1966.

[131] Peter W. Milonni and Joseph H. Eberly. *Lasers*. John Wiley & sons, 1988.

[132] G. R. Guthohrlein, M. Keller, K. Hayasaka, W. Lange, and H. Walther. A single ion as a nanoscopic probe of an optical field. *Nature*, 414:49–51, 2001.

[133] A. B. Mundt, A. Kreuter, C. Becher, D. Leibfried, J. Eschner, F. Schmidt-Kaler, and R. Blatt. Coupling a single atomic quantum bit to a high finesse optical cavity. *Phys. Rev. Lett.*, 89(10):103001, 2002.

[134] A. B. Mundt, A. Kreuter, C. Russo, C. Becher, D. Liebfried, J. Eschner, F. Schmidt-Kaler, and R. Blatt. Coherent coupling of a single $^{40}Ca^{+}$ ion to a high-finesse optical cavity. *Appl. Phys. B*, 76:117–124, 2003.

[135] A. Kreuter, C. Becher, G. P. T. Lancaster, A. B. Mundt, C. Russo, H. Häffner, C. Roos, J. Eschner, F. Schmidt-Kaler, and R. Blatt. Spontaneous emission lifetime of a single trapped $Ca^{+}$ ion in a high finesse cavity. *Phys. Rev. Lett.*, 92(20):203002, 2004.

[136] A. von Hippel, editor. *Dielectric materials and applications*. The technology press of M. I. T. and John Wiley & Sons, 1954.

[137] D. R. Denison. Operating parameters of quadrupole in a grounded cylindrical housing. *J. Vac. Sci. and Tech.*, 8:266–269, 1971.

[138] Christian E. Brodersen. Laserinduceret krystallisering af $Mg^{+}$-ioner i en lineær Paulfælde. Master's thesis, University of Aarhus, 1997.

[139] J. David Jackson. *Classical Electrodynamics*. John Wiley & Sons, 3 edition, 1999.

[140] H. C. Nägerl, Ch. Roos, D Liebfried, H. Rohde, G. Thalhammer, J. Eschner, F. Schmidt-Kaler, and R. Blatt. Investigating a qubit candidate: Spectrocopy on the $S_{1/2}$ to $D_{5/2}$ transition of a trapped calcium ion in a linear Paul trap. *Phys. Rev. A*, 61:023405, 2000.

[141] Marketech International Inc. ⟨http://www.mkt-intl.com/⟩.

[142] P. E. Hodgson, E. Gadioli, and E. Gadioli. *Introductory Nuclear Physics*. Oxford Science Publications, 1997.

[143] A. N. Nesmeyanov. *Vapor pressure of the chemical elements*. Elsevier Publ. Comp., 1963.

# APPENDIX

# A. RELEVANT DATA ON CALCIUM

## *A.1 Natural abundance of calcium*

| Isotope | Abundance |
|---|---|
| 40 | 96.941% |
| 42 | 0.647% |
| 43 | 0.135% |
| 44 | 2.086% |
| 46 | 0.004% |
| 48 | 0.187% |

*Tab. A.1:* Natural abundance values of the calcium isotopes. Values are found in [142].

## *A.2 Clebsch-Gordan coefficients in $Ca^+$*

The Clebsch-Gordan coefficients for the $\lambda = 866$ nm $3D_{3/2} \leftrightarrow 4P_{1/2}$ transition in $Ca^+$ are shown in Fig. A.1.

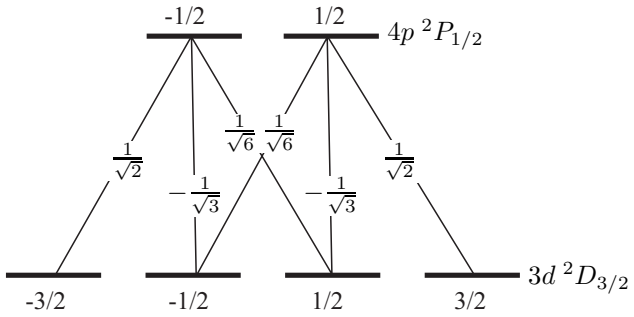


*Fig. A.1:* Clebsch-Gordan coefficients for the 866 nm $3D_{3/2} \leftrightarrow 4P_{1/2}$ transition $Ca^+$

## *A.3 Vapor pressure of calcium*

The vapor pressure of solid calcium found in Ref. [143]

$$p\,[\mathrm{mmHg}] = 10^{6.08968 - 9051.24/T - 0.00078270T + 1.03041 \log T}, \qquad \text{(A.1)}$$

where the temperature $T$ is in Kelvin.

## A.4 Root mean square nuclear radii

The root mean-square charge radii $\sqrt{\langle r^2 \rangle}$ of calcium (in fm).

| Isotope, $A$ | $\sqrt{\langle r^2 \rangle}$ [fm] | uncertainty [fm] |
|---|---|---|
| 40 | 3.4827 | 0.0017 |
| 42 | 3.5142 | 0.0017 |
| 43 | 3.5001 | 0.0017 |
| 44 | 3.5242 | 0.0017 |
| 46 | 3.5011 | 0.0017 |
| 48 | 3.4831 | 0.0017 |

*Tab. A.2:* Nuclear root mean-square charge radii of calcium. Taken from Ref. [59].

# B. STORAGE OF A SECANT PULSE

The dynamical impedance matching condition (see Eq. (7.14)) in Chap. 7 imposes a constraint on how control field $\Omega(t)$ has to be shaped for a complete transfer of an incoming one photon state to the dark state of the atom cavity system. We assume that the input photon wave packet envelope has a normalized hyperbolic secant shape, i.e.,

$$\Phi_{\rm in}(t) = \sqrt{\frac{L}{cT}}\,\mathrm{sech}\left(\frac{2t}{T}\right). \tag{B.1}$$

Inserting this into the impedance matching condition Eq. (7.14) we find the non-linear first order differential equation

$$\frac{d}{dt}\cos\theta(t) + \frac{\gamma_{\rm cav}}{2}\cos^3\theta(t) + \frac{2}{T}\tanh[2t/T]\cos\theta(t) = 0. \tag{B.2}$$

This differential equation can be solved analytically for $\cos\theta(t)$. Using the constraint that $\cos\theta(t) \to 0$ for $t \to \infty$, i.e., the dark state of the cavity-atom system ends up as a purely atomic excitation, the solution becomes

$$\cos\theta(t) = \frac{2}{\gamma_{\rm cav}T}\frac{\mathrm{sech}[2t/T]}{\sqrt{1+\tanh[2t/T]}}. \tag{B.3}$$

From this we see that the impedance matching condition can only be fulfilled provided that $\gamma_{\rm cav}T \geq 4$.

Using the definition Eq. (7.6) it is found that the Rabi frequency of the classical control field should be changed according to

$$\Omega(t) = g\sqrt{N}\frac{\mathrm{sech}[2t/T]}{\sqrt{(1+\tanh[2t/T])(\tanh[2t/T]+\gamma_{\rm cav}T/2-1)}}. \tag{B.4}$$

# C. COHERENT COUPLING STRENGTH

In this appendix the coherent coupling $g(\mathbf{r})$ between an optical cavity mode with one photon in the mode and an ion situated at $\mathbf{r}$ is derived. This is subsequently used in the calculation of the collective coupling strength $g\sqrt{N}$ of the photon field to an $^{40}Ca^{+}$ ion crystal. A two-level ion with ground state $|a\rangle$ and excited state $|b\rangle$ is exposed to an electric field $E(\mathbf{r},t) = (E_0(\mathbf{r})/2)(e^{i\omega t}+\text{c.c.})$ from the photon field mode, where $\omega$ is the photon frequency and $E_0(\mathbf{r})$ is the electric field amplitude. When the optical frequency is assumed to be resonant with the $|a\rangle \leftrightarrow |b\rangle$ transition the interaction Hamiltonian in the rotating wave approximation reads

$$H_{int} - \frac{\hbar}{2}\left(\frac{2\mathcal{D}E_0(\mathbf{r})}{\hbar}\right)[|b\rangle\langle a| + |a\rangle\langle b|], \tag{C.1}$$

where the transition dipole moment $\mathcal{D}$ is given by

$$\mathcal{D}^2 = \frac{3\pi\epsilon_0\hbar c^3 W_{\text{s}}}{\omega^3}. \tag{C.2}$$

$W_{\text{s}}$ is the transition rate of spontaneous emission and $\hbar\omega_{ab}$ is the transition frequency between the states $|a\rangle$ and $|b\rangle$. Comparing Eq. (C.1) to the interaction Hamiltonian given in Eq. (7.3)[1], we see that the one-photon coupling strength to one ion is defined by the electric field amplitude of an one-photon mode in the cavity, $E_0(\mathbf{r})$, by the relation $\hbar g(\mathbf{r}) = \frac{1}{2}\mathcal{D}E_0(\mathbf{r})$.

The electric field amplitude for each of the four arms of the running wave Gaussian bow-tie mode in the cavity we write as

$$E_0(\mathbf{r}) = \tilde{E}_0\frac{w_0}{w(z)}e^{-(x^2+y^2)/w^2(z)}, \tag{C.3}$$

where $w(z) = w_0\sqrt{1+(z\lambda/\pi w_0^2)^2}$ is the waist and $w_0$ is the minimal waist[2]. From this the mode volume function $f(\mathbf{r})$ is defined by $E_0(\mathbf{r}) = \tilde{E}_0 f(\mathbf{r})$. Now defining the coherent coupling parameter $g$ as $g(\mathbf{r}) = gf(\mathbf{r})$ it is easily shown that

$$g = \frac{\mathcal{D}}{\hbar}\sqrt{\frac{\hbar\omega}{2\epsilon_0 V}}, \tag{C.4}$$

[1] We ignore that the Hamiltonian in Eq. (7.3) includes the $a$ and $a^\dagger$ operators that describe the creation and annihilation of a cavity mode photon.

[2] For brevity the spatial displacement of the mode arms and the small angle between them is left out in this description.

where the mode volume is given by $V = \int f^2(\mathbf{r})d\mathbf{r}$ and integration is over all four mode arms of the bow-tie mode. The mode volume for the bow-tie mode is

$$V = \frac{\pi w_0^2}{2} \times 4l_{\text{cav}}, \tag{C.5}$$

where $l_{\text{cav}}$ is the cavity length. Inserting $l_{\text{cav}} = 10$ mm and $w_0 = 37$ $\mu$m we obtain a mode volume of $V \sim 0.086$ mm$^3$. The collective coupling to the $^{40}$Ca$^+$ ions in the crystal is given by the integral

$$\int g^2(\mathbf{r})n(\mathbf{r})d\mathbf{r} = g^2 \int_{^{40}\text{Ca}^+\text{crystal}} n_0 f^2(\mathbf{r})d\mathbf{r}, \tag{C.6}$$

where $n(\mathbf{r})$ is the density of the trapped $^{40}$Ca$^+$ ions and $n_0$ is the uniform density of $^{40}$Ca$^+$ in the crystal. The last integral in Eq. (C.6) is the number of $^{40}$Ca$^+$ ions that overlap with the bow-tie mode, which gives

$$N = n_0 \frac{\pi w_0^2}{2} \times l_{\text{crys}}. \tag{C.7}$$

Inserting the characteristic parameters for our experiment, namely $n_0 = 3 \times 10^8$ cm$^{-3}$, and $l_{\text{crys}} \sim 5$ mm, the number of ions contained in the cavity mode becomes $N \sim 3200$. The collective coupling Eq. (C.6) becomes

$$g^2 N = \frac{n_0 \omega \mathcal{D}^2}{8\epsilon_0 \hbar} \cdot \frac{l_{\text{crys}}}{l_{\text{cav}}}. \tag{C.8}$$

For the $3D_{3/2}(m_j = 3/2) \leftrightarrow 4D_{1/2}(m_j = 1/2)$ transition, which is coupled by the cavity field (see Fig. 8.2) the spontaneous emission rate is $W_{\text{s}} = 2\pi \times 0.84$ MHz. This is calculated from the total spontaneous emission rate of 1.69 MHz found in Fig. 2.4 and the Clebsch-Gordan coefficient for the $^2D_{3/2}(m_j = 3/2) \leftrightarrow {}^2D_{1/2}(m_j = 1/2)$ transition (see Fig. A.1) of $1/\sqrt{2}$. Inserting $W_{\text{s}} = 2\pi \times 0.84$ MHz and $\omega = 2\pi \times 3.46 \times 10^{14}$ Hz into Eq. (C.2) we find that the dipole moment of the transition $3D_{3/2}(m_j = 3/2) \leftrightarrow 4P_{1/2}(m_j = 1/2)$ in $^{40}$Ca$^+$ is $\mathcal{D} = 11 \times 10^{-30}$ m·C. We now have the relevant numbers to calculate the collective coupling strength in Eq. (C.8) and we arrive at $g\sqrt{N} \sim 2\pi \times 11.6$ MHz.

# D. CRYSTAL SIZE EXTRACTION

In order to determine the number of ions in a Coulomb crystal it is necessary to extract information about the crystal volume from the recorded images. An one component Coulomb crystal confined in the harmonic potential of our linear Paul trap has a spheroidal shape with the axis of rotational symmetry parallel to the plane in which the crystal is projected. The crystal projection correspondingly becomes an ellipse. The most obvious way to establish the volume of the spheroidally shaped crystal is to calculate it from the major and minor axis of the projected ellipse. In some applications this method will be sufficient, but it is inefficient if a large series of crystal images have to be measured and furthermore it is associated with an uncertainty from the subjective determination of the crystal boundary. Last but not least if the crystal contains more than one species the shape of each constituent is no longer spheroidal and this rudimentary method does not apply.

A more precise and faster method is to integrate the crystal volume numerically on a computer. If the boundary of the crystal is known the crystal volume $V$ can be found by assuming rotational symmetry around the $z$-axis and make the integration summation

$$V\,[\text{pixel}^3] = \sum_{i=1}^{N} \pi r_i^2 \times 1\,\text{pixel}, \tag{D.1}$$

where $r_i$ is the radial extend determined by the crystal boundary at pixel $z_i$.

The crystal boundary is found from the image of the crystal by setting an intensity threshold (see Fig. D.1). Pixels that belongs to the crystal projection are above this intensity threshold and pixels below threshold are not part of the crystal projection. We then use the image analysis program ImageJ to analyze and find the boundary of the crystal region. The crystal boundary determined this way is depicted in Fig. D.1, where it is seen that the boundary is found to be about half a shell distance outside the outer shell. At first sight this might seem to overestimate the crystal size, but is turns out that to calculate the correct ion number in the crystal half a shell distance should be added to the actual crystal boundary in the volume calculation. Despite the subjective initialization of the intensity threshold this method seems to be consistent at reproducing the crystal boundary at half a shell distance outside the crystal for different crystal images.

For medium sized crystals which are most often encountered in our experiments the uncertainty of the volume measured by the threshold method ranges

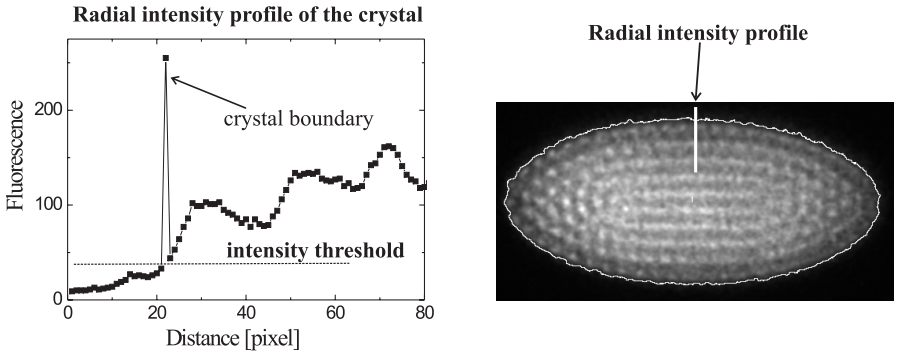


*Fig. D.1:* Techniques for determining the outer boundary of the crystal. The graph shows a radial profile plot of the crystal along the thick white line in crystal image. The pixel depth if 8 bit and the intensity peak at 22 pixels indicates the boundary found by the threshold condition. The outer boundary of the crystal (plus half a shell distance) is indicated by the white line in the crystal image.

from 2–10% depending on the crystal size. A conservative uncertainty estimate of 5% is used in this Thesis.